

# Quantum annealing and its variants: Application to quadratic unconstrained binary optimization

Vrinda Mehta

IAS Series

Band / Volume 59

ISBN 978-3-95806-755-4





Forschungszentrum Jülich GmbH  
Institute for Advanced Simulation (IAS)  
Jülich Supercomputing Centre (JSC)

# **Quantum annealing and its variants: Application to quadratic unconstrained binary optimization**

Vrinda Mehta

Schriften des Forschungszentrums Jülich  
IAS Series

Band / Volume 59

ISSN 1868-8489

ISBN 978-3-95806-755-4

Bibliografische Information der Deutschen Nationalbibliothek.  
Die Deutsche Nationalbibliothek verzeichnet diese Publikation in der  
Deutschen Nationalbibliografie; detaillierte Bibliografische Daten  
sind im Internet über <http://dnb.d-nb.de> abrufbar.

Herausgeber  
und Vertrieb:           Forschungszentrum Jülich GmbH  
                                  Zentralbibliothek, Verlag  
                                  52425 Jülich  
                                  Tel.: +49 2461 61-5368  
                                  Fax: +49 2461 61-6103  
                                  zb-publikation@fz-juelich.de  
                                  www.fz-juelich.de/zb

Umschlaggestaltung:   Grafische Medien, Forschungszentrum Jülich GmbH

Titelbild:                D-Wave Quantum Systems Inc.

Druck:                    Grafische Medien, Forschungszentrum Jülich GmbH

Copyright:              Forschungszentrum Jülich 2024

Schriften des Forschungszentrums Jülich  
IAS Series, Band / Volume 59

D 82 (Diss. RWTH Aachen University, 2023)

ISSN 1868-8489  
ISBN 978-3-95806-755-4

Vollständig frei verfügbar über das Publikationsportal des Forschungszentrums Jülich (JuSER)  
unter [www.fz-juelich.de/zb/openaccess](http://www.fz-juelich.de/zb/openaccess).



This is an Open Access publication distributed under the terms of the [Creative Commons Attribution License 4.0](https://creativecommons.org/licenses/by/4.0/),  
which permits unrestricted use, distribution, and reproduction in any medium, provided the original work is properly cited.

# Abstract

In this thesis, we study the performance of the numerical implementation of quantum annealing, as well as of physical quantum annealing systems from D-Wave Quantum Systems Inc., for solving 2-Satisfiability (2-SAT) and other quadratic unconstrained binary optimization (QUBO) problems.

For gauging the suitability of quantum annealing for solving these problems, we use three main metrics: the probability of the algorithm to solve the problem, its ability to find all the solutions to the problem if the problem has more than one solution, and the scaling of the time to solution as a function of the problem size. In doing so, we compare the performance of the numerically simulated ideal quantum annealing with its actual physical realization. We find that the ideal, standard quantum annealing algorithm can solve the sets of 2-SAT problems considered in this work, even if with a low success probability for hard problems, and can sample the degenerate ground states of the 2-SAT problems with multiple satisfying assignments in accordance with perturbation theory. However, in the long annealing time limit, the ideal standard annealing algorithm leads to a scaling of the time to solution that is worse compared to even the simple enumeration of all the possible states. On the other hand, we find noise and temperature effects to play an active role in the evolution of the state of the system on the D-Wave quantum annealers. These systems can solve a majority of the studied problems with a relatively large success probability, and the scaling of the time to solution, though still growing exponentially in the system size, is significantly improved.

Next, by means of simulations, we introduce two modifications in the standard quantum annealing algorithm, and gauge the performance of the modified algorithms. These modifications are the addition of a trigger Hamiltonian to the standard quantum annealing Hamiltonian, or a change in the initial Hamiltonian of the annealing Hamiltonian. We choose the trigger Hamiltonian to have either ferromagnetic or antiferromagnetic transverse couplings, while the additional higher-order couplings added to the typically chosen initial Hamiltonian are ferromagnetic. We find that these modifications can lead to significant improvements in the performance of the annealing algorithm, even if the scaling behavior is still exponential.



# Zusammenfassung

In dieser Arbeit untersuchen wir die Leistung der numerischen Implementierung von Quanten-Annealing sowie der physikalischen Quanten-Annealing-Systeme von D-Wave Quantum Systems Inc. zur Lösung von 2-Satisfiability (2-SAT) und anderen quadratischen uneingeschränkten binären Optimierungsproblemen (QUBO).

Um die Eignung von Quanten-Annealing für die Lösung dieser Probleme zu beurteilen, verwenden wir drei Hauptmetriken: Die Wahrscheinlichkeit, dass der Algorithmus das Problem löst, seine Fähigkeit, alle Lösungen für das Problem zu finden, falls es mehr als eine Lösung gibt, und die Skalierung der Zeit bis zur Lösung in Abhängigkeit von der Problemgröße. Dabei vergleichen wir die Leistung des numerisch simulierten idealen Quanten-Annealings mit seiner tatsächlichen physikalischen Umsetzung. Wir stellen fest, dass der ideale Standard-Quanten-Annealing-Algorithmus die in dieser Arbeit betrachteten 2-SAT-Problemsätze lösen kann, wenn auch mit einer geringen Erfolgswahrscheinlichkeit für schwierige Probleme, und dass er Stichproben über die entarteten Grundzustände der 2-SAT-Probleme mit mehreren erfüllenden Zuordnungen in Übereinstimmung mit der Störungstheorie liefern kann. Allerdings führt der ideale Standard-Annealing-Algorithmus im Grenzwert langer Zeiten zu einer schlechteren Skalierung der Zeit bis zur Lösung als selbst die einfache Aufzählung aller möglichen Zustände. Andererseits stellen wir fest, dass Rauschen und Temperatureffekte eine aktive Rolle bei der Entwicklung des Systemzustands auf den D-Wave-Quanten-Annealern spielen. Diese Systeme können einen Großteil der untersuchten Probleme mit einer relativ großen Erfolgswahrscheinlichkeit lösen, und die Skalierung der Zeit bis zur Lösung ist, wenn auch stets exponentiell wachsend in der Systemgröße deutlich verbessert.

Als Nächstes führen wir mit Hilfe von Simulationen zwei Modifikationen in den Standard-Quanten-Annealing-Algorithmus ein und messen die Leistung der modifizierten Algorithmen. Die Modifikationen sind das Hinzufügen eines Trigger-Hamiltonians zum Standard-Quanten-Annealing-Hamiltonian oder die Änderung des Anfangs-Hamiltonians im Annealing-Hamiltonian. Wir wählen den Trigger-Hamiltonian so, dass er entweder ferromagnetische oder antiferromagnetische transversale Kopplungen hat, während die zusätzlichen Kopplungen höherer Ordnung, die dem typischerweise gewählten Anfangs-Hamiltonians hinzugefügt werden, ferromagnetisch sind. Wir stellen fest, dass diese Modifikationen zu signifikanten Verbesserungen in der Leistung des Quanten-Annealing-Algorithmus führen können, auch wenn das Skalierungsverhalten immer noch exponentiell ist.



# Contents

<b>1. Introduction</b>	<b>1</b>
1.1. A general overview . . . . .	1
1.2. Gate-based quantum computing . . . . .	3
1.2.1. Single-qubit state . . . . .	3
1.2.2. Qubit as a two-level system . . . . .	4
1.2.3. Multi-qubit state . . . . .	5
1.2.4. Basic operations for gate-based quantum computing . . . . .	5
1.3. Quantum annealing . . . . .	6
1.3.1. The adiabatic theorem . . . . .	7
1.3.2. The Landau-Zener theory . . . . .	8
1.4. Problem sets . . . . .	9
1.4.1. 2-SAT problems . . . . .	10
1.4.1.1. Creation . . . . .	10
1.4.1.2. Properties . . . . .	11
1.4.1.3. Ising formulation . . . . .	12
1.4.2. 2-SAT-derived problems . . . . .	13
1.4.2.1. Random-g problems . . . . .	14
1.4.2.2. Multiple-copies problems . . . . .	14
1.4.3. Fully-connected QUBO problems . . . . .	14
1.4.3.1. Random problems . . . . .	14
1.4.3.2. Regular problems . . . . .	15
1.4.3.3. Solving the fully-connected problems . . . . .	15
1.5. Our focus . . . . .	16
<b>2. Numerical methods</b>	<b>17</b>
2.1. Essential operations . . . . .	17
2.1.1. Single-qubit operations . . . . .	17
2.1.2. Two-qubit operators . . . . .	18
2.2. Solving the TDSE . . . . .	20
2.2.1. Crank-Nicolson algorithm . . . . .	21
2.2.2. Suzuki-Trotter product formula algorithm . . . . .	22
2.3. Lanczos algorithm for solving the spectrum . . . . .	25
2.3.1. Repeated minimization in two-dimensional Krylov subspace . . . . .	25
2.3.2. Minimization in L-dimensional Krylov subspace . . . . .	26
<b>3. Assessing the performance of the D-Wave systems</b>	<b>29</b>
3.1. Solving optimization problems using D-Wave systems . . . . .	30
3.1.1. Embedding of the problem Hamiltonian . . . . .	30

3.1.2.	D-Wave controls . . . . .	31
3.2.	Results . . . . .	32
3.2.1.	Benchmarking the D-Wave systems . . . . .	32
3.2.1.1.	18-variable 2-SAT problems . . . . .	32
3.2.1.2.	Random-g problems . . . . .	33
3.2.1.3.	Multiple-copies problems . . . . .	35
3.2.1.4.	Fully-connected QUBO problems . . . . .	37
3.2.2.	Hardness of the QUBO problems . . . . .	39
3.2.2.1.	Hamming distance analysis . . . . .	39
3.2.2.2.	Scaling analysis . . . . .	40
3.3.	Summary . . . . .	41
<b>4.</b>	<b>Fair sampling</b>	<b>43</b>
4.1.	Forward annealing . . . . .	43
4.1.1.	Simulation results . . . . .	44
4.1.2.	D-Wave results . . . . .	47
4.1.3.	Perturbation theory . . . . .	48
4.2.	Reverse annealing . . . . .	50
4.2.1.	Simulation results . . . . .	50
4.2.2.	D-Wave results . . . . .	56
4.3.	Summary . . . . .	60
<b>5.</b>	<b>Adding the trigger Hamiltonian</b>	<b>63</b>
5.1.	2-SAT problems . . . . .	64
5.1.1.	Standard Hamiltonian . . . . .	64
5.1.2.	Hamiltonian with the ferromagnetic trigger Hamiltonian . . . . .	66
5.1.3.	Hamiltonian with the antiferromagnetic trigger Hamiltonian . . . . .	68
5.2.	Nonstoquastic problem Hamiltonians . . . . .	74
5.3.	Summary . . . . .	79
<b>6.</b>	<b>Scaling and distribution of quantifiers of quantum annealing</b>	<b>81</b>
6.1.	Analysis criteria . . . . .	81
6.1.1.	Minimum energy gap . . . . .	82
6.1.2.	Success probability . . . . .	82
6.1.3.	Time to solution . . . . .	84
6.2.	Numerical results . . . . .	85
6.2.1.	Minimum energy gaps . . . . .	85
6.2.2.	Success probability . . . . .	87
6.2.3.	TTS99 . . . . .	90
6.3.	D-Wave results . . . . .	91
6.3.1.	Success probability . . . . .	91
6.3.2.	TTS99 . . . . .	92
6.4.	Summary . . . . .	94

<b>7. Modifying the initial Hamiltonian</b>	<b>97</b>
7.1. Choices for the initial Hamiltonian . . . . .	97
7.2. Results . . . . .	99
7.2.1. Minimum energy gaps . . . . .	99
7.2.2. Success probability . . . . .	100
7.2.3. Scaling . . . . .	103
7.3. Summary . . . . .	104
<b>8. Summary</b>	<b>107</b>
<b>Appendices</b>	<b>113</b>
<b>A. Proof of the adiabatic theorem</b>	<b>114</b>
<b>B. Uniqueness of the ground state of the annealing Hamiltonian</b>	<b>121</b>
<b>C. Pseudo-code for the Kosaraju-Sharir’s algorithm</b>	<b>123</b>
<b>D. Discretizing a quantum Hamiltonian in continuous space</b>	<b>125</b>
<b>E. Error bounds</b>	<b>127</b>
E.1. Crank-Nicolson algorithm . . . . .	127
E.2. Suzuki-Trotter product formula algorithm . . . . .	128
E.2.1. First-order approximation . . . . .	128
E.2.2. Second-order approximation . . . . .	129
<b>F. Quantum simulation</b>	<b>131</b>
<b>G. Distributions</b>	<b>133</b>
<b>Bibliography</b>	<b>135</b>
<b>List of publications</b>	<b>147</b>
<b>Eidesstattliche Erklärung</b>	<b>149</b>
<b>Acknowledgements</b>	<b>151</b>



# 1. Introduction

A quantum computer is a computing device that can exploit certain features of quantum mechanics, like superposition and entanglement, which can help these systems solve some particularly hard tasks believed to be challenging for classical computers. The underlying idea is that making use of such properties, quantum computers can access a larger portion of the computational space, the so-called Hilbert space, in a given time, which makes them fundamentally different and more powerful than the present-day classical computers for specific applications.

In this chapter, we provide an overview of quantum computing. We discuss the major landmarks in quantum computing and the state of the art quantum computers, followed by a review of the basic concepts of the two standard models for quantum computers. In the subsequent sections, we discuss the adiabatic theorem and the Landau-Zener theory, and define the sets of problems used in this work. In the last section, we explain the motivation for this work.

## 1.1. A general overview

One of the first ideas for designing quantum computers which is believed to have led to the conception of quantum computation, was proposed by Richard Feynman [Fey82]. He suggested that classical computers might not be sufficient to reproduce the behavior of quantum systems as the computational resources required increase exponentially with the number of interacting particles in the system. Thus, it was proposed that if special computers based on the laws of quantum mechanics could be designed, they could be better equipped to simulate such systems. Around the same time, Paul Benioff came up with a quantum mechanical version of the Turing machine [Ben80]. Over the next few years, such ideas led to the development of several quantum computing algorithms which have a proven speed up over any existing classical algorithms. Some examples of such algorithms are Deutsch-Jozsa algorithm [Deu85; DJ92], Bernstein–Vazirani algorithm [BV97], Simon algorithm [Sim97], Grover’s search algorithm [Gro96; Gro97], and Shor’s prime factorization algorithm [Sho99]. Further research and development in the field led to a search for potential applications for quantum computing, and has resulted in a list which has continued to vastly expand over the years [OML19; BGM21]. These applications include finance, medicine, logistics, scheduling, machine learning, cryptography, and many more [Tra+16; WE19; VK19; Sak20; DBM21; SBS18; Mav+18; Cor+22; WKI12; AHY20; Moh+21; MHF21]. The availability of commercial quantum computers has given a further boost to research in this direction [Wal+05; PAL14; Boi+14; Røn+14; AL18b; Dev16; Mic+17; CWM21].

There are two standard approaches for building a quantum computer. The first and

more widely known model is that of the gate-based quantum computers, while the second and a relatively recent model is the adiabatic model of quantum computing. The gate-based quantum computer model is inspired from the gate-based model of a classical computer, where sets of quantum gates are used to carry out any computation [NC10]. There are several companies, e.g., Google, IBM, Rigetti, IonQ, and eleQtron, that offer gate-based quantum computers. However, the number of qubits in such devices remains limited to about a hundred qubits. The underlying issues for the practical applicability of quantum computers to real-world applications are decoherence of the qubits and gate errors. Furthermore, sparse connectivity between the qubits also adversely affects the performance of these devices. Although ion-trap quantum computers have an all to all connectivity, the major drawback of this architecture is that it is difficult to initialize the ions in their motional groundstates [NC10].

The second model for quantum computing is the adiabatic model of quantum computing. Based on the idea of this model, special purpose quantum computers, the so-called quantum annealers, have been devised for solving optimization problems which have gained popularity over the past years. Quantum annealing is the quantum-inspired version of simulated annealing [KGV83], where thermal fluctuations are replaced by quantum fluctuations, with the aim of making use of quantum tunnelling in finding the energy configuration with the minimum energy [ACd89; Fin+94; KN98]. It was initially thought of as an optimization algorithm for solving optimization problems, with the hope that it can outperform simulated annealing by facilitating the search for the state with the minimum energy even when the state of the system gets trapped in a local minimum with a high but narrow potential barrier, a case for which simulated annealing becomes ineffective. Quantum annealing was viewed as an alternative route to quantum computation for the first time with its experimental realization in disordered magnets, where it was proposed that the computational problem can be cast as a classical spin problem, and can then be solved by the combination of thermal cooling and application of a transverse field [Bro+99]. In the early 2000's, this idea was formalized more, where it was shown that although not necessarily beneficial, the adiabatic quantum evolution could be well approximated by discrete unitary gates to accommodate this idea in the gate-based paradigm of quantum computing [Far+00]. In [Far+01] it is suggested that this continuous time evolution can in fact offer an alternative model for quantum computation. Although sometimes used interchangeably, there are some differences in the notion of quantum annealing and adiabatic quantum computation. Unlike adiabatic quantum computation, quantum annealing does not impose the strict condition of the evolution being adiabatic [Dic+13; VL17]. These ideas form the basis of the present-day adiabatic quantum computing, resulting in the development of quantum annealing systems with more than 5000 qubits [MF20]. In contrast to the gate-based quantum computers, quantum annealers require much less controls on a single-qubit level, and are relatively more robust against decoherence. However, sparse connectivity between the qubits is an obstacle for the performance of these systems.

While it has not been possible to demonstrate an indisputable speed-up of quantum computers for solving any practically relevant problems so far, with emerging technological advancements in their realization, it has become possible to implement more kinds of, as

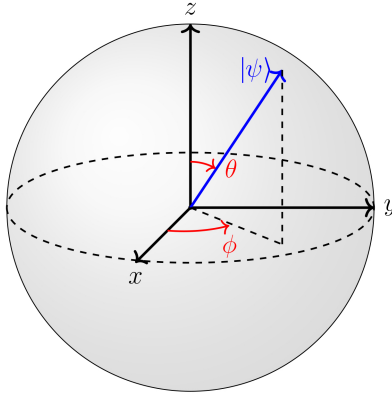


Figure 1.1.: Bloch sphere representation of quantum state  $|\psi\rangle$ .

well as larger problems on these quantum computers. Using quantum annealing, it has been possible to solve many industry-based optimization problems [Nev+09; Cla+19; Fel+19; Mul+19; Ino+21; Yar+22].

## 1.2. Gate-based quantum computing

In this section, we discuss the essential concepts and notations related to gate-based quantum computing [NC10]. We start by describing the fundamental unit of quantum computing, the qubit, and then proceed to discuss a physical representation for it. Next, we define the notations for a system consisting of multiple qubits, and lastly, we introduce the basic gate operations for a quantum computer.

### 1.2.1. Single-qubit state

For classical (digital) computers, a bit is the smallest unit of data that a computer can process and store, which is a binary variable that can assume values 0 or 1. Any computation on the digital computer then progresses by performing operations that transform the string of bits  $\{0, 1\}^n$  to another bit string  $\{0, 1\}^m$ . Similarly, the basic unit of processing for a quantum computer are quantum bits, or qubits. However, unlike the classical bits, a qubit can exist in a superposition state of  $|0\rangle$  and  $|1\rangle$ , i.e., the state of a qubit can be expressed as

$$|\psi\rangle = a_0 |0\rangle + a_1 |1\rangle, \quad (1.1)$$

where  $a_0$  and  $a_1$  are complex numbers, such that  $|a_0|^2 + |a_1|^2 = 1$ , and  $|0\rangle$  and  $|1\rangle$  are the basis vectors constituting the computational basis. However, a measurement of the state of the qubit does not yield the complex coefficients  $a_0$  and  $a_1$  directly, but results in one of the states  $|0\rangle$  or  $|1\rangle$ . According to the quantum theory, the probability of obtaining these states are  $|a_0|^2$  and  $|a_1|^2$ , respectively.

In the polar representation, the complex coefficients  $a_0$  and  $a_1$ , given in Eq. (1.1), can be written as  $a_0 = r_0 e^{i\phi_0}$  and  $a_1 = r_1 e^{i\phi_1}$ , and thus, the general state for a single-qubit

$$|\psi\rangle = r_0 e^{i\phi_0} |0\rangle + r_1 e^{i\phi_1} |1\rangle, \quad (1.2)$$

is determined by the two amplitudes  $r_0$  and  $r_1$ , and the two phases  $\phi_0$  and  $\phi_1$ . According to the quantum theory, multiplying a state  $|\psi\rangle$  by a global phase

$$e^{-i\phi_0} |\psi\rangle = r_0 |0\rangle + r_1 e^{i(\phi_1 - \phi_0)} |1\rangle, \quad (1.3)$$

does not lead to any observable changes in the state  $|\psi\rangle$ . Furthermore, since  $|a_0|^2 + |a_1|^2 = 1$ , we obtain  $|r_0|^2 + |r_1|^2 = 1$ , and without loss of generality, we can assume  $r_0 = \cos \theta/2$  and  $r_1 = \sin \theta/2$  for  $\theta \in [0, \pi]$ . Setting  $\phi = \phi_1 - \phi_0$ , a general state of a single-qubit can be expressed as

$$|\psi\rangle = \cos \frac{\theta}{2} |0\rangle + e^{i\phi} \sin \frac{\theta}{2} |1\rangle, \quad (1.4)$$

where  $\phi \in [0, 2\pi]$ . Using this representation, with two independent variables,  $\theta$  and  $\phi$  the state of a qubit can be represented on a sphere, known as the Bloch sphere, which is shown in Fig. 1.1.

## 1.2.2. Qubit as a two-level system

Like the intrinsic spin of an electron, a qubit is also a two-level system. Thus, a natural physical representation for a qubit can be a spin-1/2 particle. In this notation, the convention is to represent the state  $|0\rangle$  as  $|\uparrow\rangle$  (with spin value  $\hbar/2$ ) and the state  $|1\rangle$  as  $|\downarrow\rangle$  (with a spin value  $-\hbar/2$ ). Thus, another valid representation for a qubit is the state

$$|\psi\rangle = a_0 |\uparrow\rangle + a_1 |\downarrow\rangle. \quad (1.5)$$

The spin operator  $\mathbf{S} = 1/2 \boldsymbol{\sigma}$  acts on the Hilbert space spanned by the basis vectors  $|\uparrow\rangle$  and  $|\downarrow\rangle$ , where we have set  $\hbar = 1$ ,  $\boldsymbol{\sigma} = (\sigma^x, \sigma^y, \sigma^z)$ , and

$$\sigma^x = \begin{pmatrix} 0 & 1 \\ 1 & 0 \end{pmatrix}, \sigma^y = \begin{pmatrix} 0 & -i \\ i & 0 \end{pmatrix}, \sigma^z = \begin{pmatrix} 1 & 0 \\ 0 & -1 \end{pmatrix}, \quad (1.6)$$

are the Pauli-matrices.

The expectation value of the Pauli-matrices, which represents the measurement outcome of a physical observable, i.e., a Hermitian operator, is given as  $\langle \psi | \sigma^\alpha | \psi \rangle$ , for  $\alpha = x, y, z$ . Thus for the state given by Eq. (1.5), we have

$$\langle \sigma^x \rangle = a_0 a_1^* + a_0^* a_1 \quad \langle \sigma^y \rangle = a_0 a_1^* - a_0^* a_1, \quad \langle \sigma^z \rangle = a_0 a_0^* - a_1 a_1^*, \quad (1.7)$$

where  $a_0^* (a_1^*)$  is the complex conjugate of  $a_0 (a_1)$ .

In a similar manner, there can be other valid representations for a qubit as long as it is possible to sufficiently isolate the two unique states of a physical system. Furthermore, from a practical point of view, it should be possible to control the transitions from one of these two states to the other. One example of such a qubit are the superconducting

qubits which are designed using circuit elements like capacitors and inductors. However, the energy difference between the successive energy levels of a system consisting of only linear elements is constant, making it impossible to single out two energy levels. To overcome this problem, a Josephson junction is added to the circuit, which introduces anharmonicity in the Hamiltonian, thus giving a way to approximate the system as a two-level system. Other possible types of qubits include trapped ion, quantum dots, and topological qubits.

### 1.2.3. Multi-qubit state

So far we have focused on the state involving only one qubit. However, from a practical point of view, such a system is not very useful for real-world applications. We therefore consider a system of  $N$  qubits. The quantum state of such a system is defined by the linear superposition of the product states of the  $N$  single-qubit states (constituting the so-called computational basis), and is given by

$$|\psi\rangle = a_0 |00\dots 00\rangle + a_1 |00\dots 01\rangle + \dots + a_{2^{N-2}} |11\dots 10\rangle + a_{2^{N-1}} |11\dots 11\rangle, \quad (1.8)$$

where coefficients  $a_0, \dots, a_{2^{N-1}}$  are complex numbers which are renormalized such that  $\sum_{i=0}^{2^N-1} |a_i|^2 = 1$  so that  $\langle\psi|\psi\rangle = 1$ . Expressing the basis vectors in decimal representation instead of binary, the state of the system can be equivalently written as

$$|\psi\rangle = a_0 |0\rangle + a_1 |1\rangle + \dots + a_{2^{N-2}} |2^N - 2\rangle + a_{2^{N-1}} |2^N - 1\rangle. \quad (1.9)$$

### 1.2.4. Basic operations for gate-based quantum computing

After having introduced the state representing the system consisting of multiple qubits, we now focus on some of the basic gates that are commonly used in quantum computing. The most fundamental single-qubit gates are the bit-flip  $X$  gate, bit- and phase-flip  $Y$  gate, and the phase-flip  $Z$  gate. In matrix representation, they are equivalent to the Pauli-matrices  $\sigma^x$ ,  $\sigma^y$ ,  $\sigma^z$ , respectively, given by Eq. (1.6). Their action on the qubit state  $|\psi\rangle$  given by Eq. (1.1) is thus

$$\begin{aligned} X|\psi\rangle &= a_0 X|0\rangle + a_1 X|1\rangle = a_0 |1\rangle + a_1 |0\rangle, \\ Y|\psi\rangle &= a_0 Y|0\rangle + a_1 Y|1\rangle = ia_0 |1\rangle - ia_1 |0\rangle, \\ Z|\psi\rangle &= a_0 Z|0\rangle + a_1 Z|1\rangle = a_0 |0\rangle - a_1 |1\rangle. \end{aligned} \quad (1.10)$$

It can be readily verified that the  $X$ ,  $Y$ , and  $Z$  gates are unitary, i.e., they conserve the norm of the qubit state upon which they act. The effective action of any single-qubit unitary quantum operation is to cause a rotation of the qubit state. The rotational operator  $R^{\mathbf{v}}(\theta)$  causing the rotation of a state around a unit vector  $\mathbf{v}$  by an angle  $\theta$  is of the form

$$R^{\mathbf{v}}(\theta) = e^{-i\theta\mathbf{v}\cdot\boldsymbol{\sigma}/2} = \mathbb{I} \cos \frac{\theta}{2} - i\mathbf{v}\cdot\boldsymbol{\sigma} \sin \frac{\theta}{2}, \quad (1.11)$$

where  $\boldsymbol{\sigma} = (\sigma^x, \sigma^y, \sigma^z)$  is given by the Pauli matrices of Eq. (1.6). Particularly important rotation operators are the rotation gates  $R^x(\theta)$ ,  $R^y(\theta)$ , and  $R^z(\theta)$  around the  $x$ -,  $y$ -,

and  $z$ -axes, respectively given by

$$\begin{aligned} R^x(\theta) &= \begin{pmatrix} \cos \frac{\theta}{2} & -i \sin \frac{\theta}{2} \\ -i \sin \frac{\theta}{2} & \cos \frac{\theta}{2} \end{pmatrix}, \\ R^y(\theta) &= \begin{pmatrix} \cos \frac{\theta}{2} & -\sin \frac{\theta}{2} \\ \sin \frac{\theta}{2} & \cos \frac{\theta}{2} \end{pmatrix}, \\ R^z(\theta) &= \begin{pmatrix} e^{-i\theta/2} & 0 \\ 0 & e^{i\theta/2} \end{pmatrix}. \end{aligned} \tag{1.12}$$

Any unitary single-qubit operation can be constructed using a combination of rotation gates with different angles and axes of rotation, together with a global phase shift on the qubit [NC10].

In addition, commonly introduced single-qubit discrete gates in quantum computing literature are the Hadamard gate

$$H = \frac{1}{\sqrt{2}} \begin{pmatrix} 1 & 1 \\ 1 & -1 \end{pmatrix}, \tag{1.13}$$

the phase gate

$$S = \begin{pmatrix} 1 & 0 \\ 0 & i \end{pmatrix}, \tag{1.14}$$

and the  $\pi/8$  gate

$$T = \begin{pmatrix} 1 & 0 \\ 0 & \exp(i\pi/4) \end{pmatrix}. \tag{1.15}$$

Another important discrete gate for quantum computation is the 2-qubit Controlled-NOT or CNOT gate. This gate has two inputs, the control qubit and the target qubit, and only in the case that the control qubit is in state  $|1\rangle$ , the target qubit is flipped. In the matrix notation, this gate is defined as

$$CNOT = \begin{pmatrix} 1 & 0 & 0 & 0 \\ 0 & 1 & 0 & 0 \\ 0 & 0 & 0 & 1 \\ 0 & 0 & 1 & 0 \end{pmatrix}. \tag{1.16}$$

Together with the Hadamard gate and the  $\pi/8$  gate, the CNOT gate forms a set of discrete universal gates for quantum computation [NC10].

### 1.3. Quantum annealing

We now shift our focus to quantum annealing. The basic idea of quantum annealing is quite distinct from that of gate-based quantum computing. It is commonly used to solve optimization problems for which an optimization problem is mapped to the Ising Hamiltonian

$$H_P = - \sum_{i=1}^N h_i^z \sigma_i^z - \sum_{\langle i,j \rangle} J_{i,j}^z \sigma_i^z \sigma_j^z, \tag{1.17}$$

where  $h_i^z$  is the applied field acting along the  $z$ -direction,  $J_{i,j}^z$  is the coupling between the  $i^{\text{th}}$  and  $j^{\text{th}}$  spins, and  $\langle i, j \rangle$  denotes the set of coupled spins.

The quantum annealing algorithm consists of starting in the ground state of an easy to prepare initial Hamiltonian,  $H_I$ , from where the system is slowly swept towards the final Hamiltonian,  $H_P$ , encoding the optimization problem that needs to be solved, by means of an annealing parameter  $s$ , defined as  $s = t/T_A$ , where  $T_A$  is the annealing time. The instantaneous annealing Hamiltonian is typically of the form

$$H(s) = A(s)H_I + B(s)H_P, \quad (1.18)$$

where functions  $A(s)$  and  $B(s)$  control the annealing schedule, and are chosen such that  $A(0)/B(0) \gg 1$  and  $A(1)/B(1) \ll 1$ . For a major part of the simulations in this work, we have chosen a linear scheme for annealing, i.e.,

$$H(s) = (1-s)H_I + sH_P. \quad (1.19)$$

The transverse-field Hamiltonian, with the uniform superposition state as its ground state, is one of the simplest choices for the initial Hamiltonian. In symbols

$$H_I = - \sum_{i=1}^N h_i^x \sigma_i^x, \quad (1.20)$$

where  $h_i^x$  is the magnetic field along the  $x$ -direction and typically, we have  $h_i^x = 1$  for all  $i$ . With these choices, the resulting Hamiltonian, referred to as the standard quantum annealing Hamiltonian in this thesis, Eq. (1.18) is stoquastic, i.e., all its off-diagonal elements are real and non-positive in the computational basis. This construction of Hamiltonian is believed to be less powerful than the universal model for quantum computation. On the other hand, with a non-stoquastic Hamiltonian the adiabatic model for quantum computation has been shown to be polynomially equivalent to the conventional gate-based model of quantum computing, and therefore, universal [Aha+07; BL08; Miz19].

Initializing the system in the ground state of the initial Hamiltonian and choosing the annealing time to be sufficiently long, we can find the solution to the optimization problem by solving the time-dependent Schrödinger equation (TDSE)

$$i \frac{\partial}{\partial t} |\psi(t)\rangle = H(t) |\psi(t)\rangle. \quad (1.21)$$

This is guaranteed by the adiabatic theorem, which will be discussed next. The numerical techniques to solve the TDSE are discussed in chapter 2.

### 1.3.1. The adiabatic theorem

The adiabatic theorem states that if the sweep from the initial Hamiltonian to the final Hamiltonian is done slowly enough, the state of the system stays in the same eigenstate of the instantaneous Hamiltonian as the eigenstate from which the algorithm starts [BF28; Kat50]. This implies that if the annealing time is sufficiently long, and one starts in the ground state of the initial Hamiltonian, the adiabatic theorem ensures that one obtains

the ground state of the problem Hamiltonian, which is the state encoding the solution to the given optimization problem. Mathematically, this requires [Ami09],

$$T_A \gg \max_{0 \leq s \leq 1} \frac{\| \langle 1(s) | \frac{dH}{ds} | 0(s) \rangle \|}{\Delta(s)^2}, \quad (1.22)$$

where  $T_A$  is the annealing time,  $|0(s)\rangle$  and  $|1(s)\rangle$  are the ground state and the first excited state of the instantaneous Hamiltonian, respectively, and  $\Delta(s)$  represents the energy gap between the two. For understanding the proof for the adiabatic theorem for a system with a non-degenerate ground state, see Appendix A. The validity of the adiabatic theorem, and hence that of the quantum annealing algorithm depends on the existence of an energy gap between the ground state and the first excited state of the annealing Hamiltonian, i.e., on the condition that there is no crossing between these energy levels. This is shown to be the case in Appendix B.

### 1.3.2. The Landau-Zener theory

The Landau-Zener model, describing a spin-1/2 particle, also deals with systems evolving under a time-dependent Hamiltonian [Lan32; Zen32; De +97]. In this section, we review the Landau-Zener theory.

For a two-level system, under the action of a slowly reversing magnetic field (from  $-H_0$  to  $H_0$  in time  $T$ ) and a constant transverse-field, the time-dependent Hamiltonian is given as

$$H_{LZ}(t) = -\Gamma\sigma^x - ct\sigma^z, \quad (1.23)$$

where  $\Gamma$  sets the level-splitting between the two energy levels,  $c = 2H_0/T$  controls the speed of the sweep of the magnetic field, such that  $H(t) = ct$ , and  $t$  ranges from  $-T/2$  to  $T/2$ . For such a set-up, we can use the Landau-Zener formula to obtain an estimate for the probability of the state of the system to stay in the ground state, if initialized in the ground state. The probability for the system to change its state of magnetization from  $|\downarrow\rangle$  at large negative times to  $|\uparrow\rangle$  at large positive times is given as [Lan32; Zen32]

$$p_0 = 1 - p_1 = 1 - e^{-\pi\Gamma^2/hc}, \quad (1.24)$$

where  $p_1 = \exp(-\pi\Gamma^2/hc)$  is the probability of the system going through a non-adiabatic transition and retaining  $|\downarrow\rangle$  as the state of the system. For slow sweep of the magnetic field, i.e., a small value of  $c$ , we obtain  $p_0 \approx 1$ .

Figure 1.2(a) shows the energy spectrum and the energy expectation values of a spin-1/2 particle under an external magnetic field with  $H_0 = 100$  for different times  $T$ , while Fig. 1.2(b) shows the response of the magnetization of the system to the reversing magnetic field for  $T = 500$ , i.e.,  $c = 0.4$ . It can be seen that the step in the magnetization corresponds to the position of the anticrossing in the energy spectrum.

The main quantity of interest, here and for the majority of this work, is the success probability. In the case of simulations, it is calculated by determining the overlap of the numerically obtained state by implementing the time evolution according to the TDSE, with the known ground state of the problem.

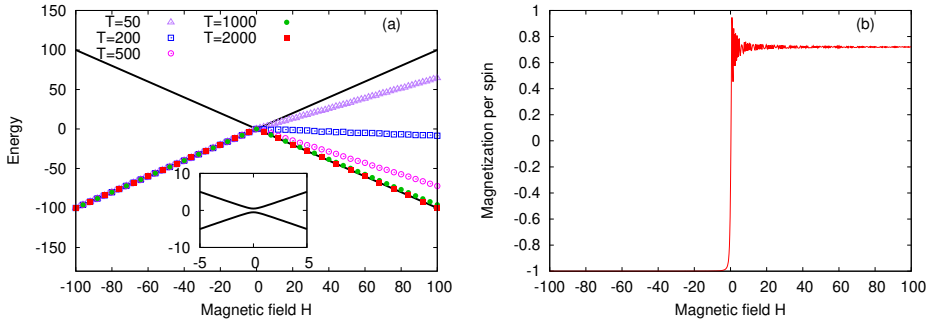


Figure 1.2.: (a) Energy spectrum and energy expectation values corresponding to different times for a 2-level system under a slowly reversing magnetic field with  $\Gamma = 0.5$  and  $H_0 = 100$ . The inset shows the point of anticrossing. (b) The magnetization of the spin-1/2 particle with  $T = 500$ .

The plot for the success probability obtained for the given system, with different sweep times is shown in Fig. 1.3. Fitting function of type  $1 - \exp(aT)$  yields  $a = -0.004$ . Comparing with Eq. (1.24), one obtains  $a = -\pi\Gamma^2/c = -0.004$ , which is the same as the fitting exponential obtained in Fig. 1.3.

Both the quantum annealing Hamiltonian, and the Landau-Zener Hamiltonian are time-dependent Hamiltonians that consist of non-commuting operators  $\sigma^x$  and  $\sigma^z$  terms. However, the forms of the Hamiltonians are different. Moreover, in quantum annealing, one usually deals with more complex systems than a 2-level system. However, the Landau-Zener formula can still be used to obtain an estimate for the success probability in the long annealing-time limit, where the evolution of the state of the system is almost adiabatic, i.e., the evolution is adiabatic except in the vicinity of the anticrossing and the system can be effectively approximated by a 2-level system in the vicinity of the anticrossing.

## 1.4. Problem sets

In this section, we discuss the sets of problems that will be considered in this work for assessing the performance of quantum annealing. We focus also on the method for creating these problems, some of their statistical properties, and their mapping to a form suitable for quantum annealing for solving them.

Combinatorial optimization is a class of problems where the task is to find an optimal assignment to the set of variables constituting the problem such that the corresponding cost function is minimized for this assignment. For real-world combinatorial optimization problems, the number of possible solutions increases exponentially with the size of the problem. This makes these problems, in general, difficult to solve. As mentioned previously, it is believed that quantum annealing, equipped with features like quantum tunneling, can be more suitable for solving such problems compared to the classical algorithms like simulated annealing.

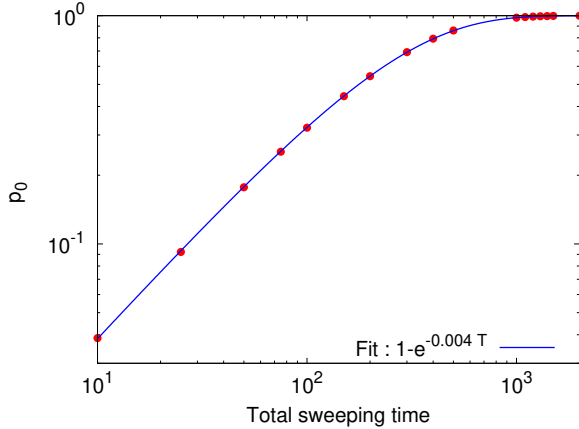


Figure 1.3.: Success probability  $p_0$  for different time of sweeps with  $H_0 = 100$  and  $\Gamma = 0.5$ .

For most parts of this thesis, we use sets of hard (to be qualified later) 2-satisfiability (2-SAT) problems for benchmarking different variants of the quantum annealing algorithm as well as D-Wave quantum annealers. Furthermore, we also use some sets of problems derived from the 2-SAT problems and other randomly generated problems for benchmarking purposes.

### 1.4.1. 2-SAT problems

We start with the definition of the SAT problems. A  $K$ -SAT problem is described by a Boolean function  $F$  of  $N$  binary variables, consisting of a conjunction of  $M$  clauses, each of which is a disjunction of  $K$  literals [JS94], i.e.,

$$F = (L_{1,1} \vee L_{1,2}) \wedge (L_{2,1} \vee L_{2,2}) \wedge \dots \wedge (L_{M,1} \vee L_{M,2}), \quad (1.25)$$

for  $K = 2$ , where literal  $L_{\alpha,j}$  can be a binary variable  $x_i$  or its negation  $\bar{x}_i$  for  $i = 1, 2, \dots, N$ ,  $\alpha = 1, 2, \dots, M$ , and  $j = 1, 2$ . The SAT problem is considered satisfiable if there exists an assignment for the binary variables that makes the Boolean function true.

The sets of 2-SAT problems used in this work, range from  $6 \leq N \leq 20$ , with  $M = N + 1$ , as the satisfiability threshold (the number of clauses  $M$  for a given  $N$  at which the SAT problems change from satisfiable to unsatisfiable in the mean) for a random 2-SAT problem lies around  $M \approx N$  [Neu14b].

#### 1.4.1.1. Creation

In this work, we use two ensembles of sets of hard 2-SAT problems. The first is an already existing set of problems with  $6 \leq N \leq 18$ , where the sets with  $N < 10$  consist of 100 problems each, while the sets with  $N \geq 10$  contain 1000 problems [Neu14a]. These sets of problems were created by Markov chain Monte-Carlo partitioning the realization

space of random K-SAT problems with respect to the degeneracy of the ground state [Neu14a]. From the set of generated problems, those with a ground state degeneracy of one were stored, so that the resulting set of problems is particularly hard to be solved using simulated annealing. The brute-force search method used for determining the degeneracy of the ground state of these problems, scales as  $\mathcal{O}(2^N)$ , which limits the size of the problems that could be created in this way.

In the present section, we discuss another method for creating the second set of 2-SAT problems, with which we generate problem sets with ground state degeneracy of one, two and four. Using this method, we create problem sets consisting of 100 problems each, with the number of variables ranging from  $6 \leq N \leq 20$ . The clauses of these problems are made keeping in mind the following constraints.

- The two literals involved in each clause cannot correspond to the same variable.
- No clause can be repeated.
- All the variables are utilized at least in one of the clauses.

From the resulting sets of problems, we need to identify the unsatisfiable problem instances. This is done by making use of the implication graph of the 2-SAT problems. Using Kosaraju-Sharir's algorithm [Sha81] we then identify the strongly connected components in the implication graph, which are the sets of vertices reachable from one another. If we find a variable and its negation to belong to the same strongly connected component, the 2-SAT problem does not have any satisfying assignments. Such problems are discarded from the problem sets. The pseudo-code for the implementation of the Kosaraju-Sharir's algorithm for identifying the strongly connected components is given in Appendix C.

Using brute-force search, we find all the satisfying assignments for the remaining problems and select the ones with 1, 2, and 4 satisfying assignments.

For creating these problems, we made use of the workstations equipped with Intel Core i7-8700 and 32 GB memory for the smaller problems ( $6 \leq N \leq 13$ ), while for the larger problems we used the supercomputer JUWELS of the Jülich Supercomputing Centre at Forschungszentrum Jülich [Jül19].

### 1.4.1.2. Properties

We now discuss a few analytical properties of the new sets of 2-SAT problems obtained. Using combinatorics, we find the average number of satisfying assignments  $\mu$  to be

$$\langle \mu \rangle = \left(1 - \frac{1}{2K}\right)^M 2^N, \quad (1.26)$$

where  $N$  is the number of variables involved in the problem,  $M$  is the number of clauses, and  $K = 2$  for 2-SAT problems [EGS11]. It should be noted however, that this formula holds when no constraints are placed on the way the clauses are created. In Fig. 1.4 we compare the average ground state degeneracy of the obtained sets of 2-SAT problems with this theoretical expectation as a function of  $N$  with  $M = N + 1$ . Although in good

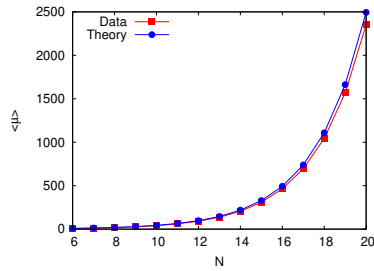


Figure 1.4.: Average degeneracy of the ground state of the problem Hamiltonian for  $M = N + 1$  and  $6 \leq N \leq 20$ .

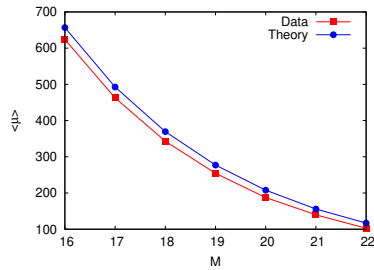


Figure 1.5.: Average degeneracy of the ground state of the problem Hamiltonian for  $N = 16$  and  $16 \leq M \leq 22$ .

agreement, the slight deviations of the average number of satisfying assignments obtained from the created sets of problems from the theoretically predicted values can be explained on the basis of the constraints imposed while generating the problems.

Next, keeping  $N$  fixed at 16, we can plot the average number of satisfying assignments of the 2-SAT problems as a function of the number of clauses  $M = N + a$ , with  $0 \leq a \leq 6$ . The resulting plot is shown in Fig. 1.5, where the deviations between the theoretical formula and the experimentally obtained values become apparent.

Furthermore, we analyze the scaling of the degeneracy of the first excited state of the sets of problems with 1, 2, and 4 satisfying assignments as a function of the number of variables in the problem. The results are shown in Fig. 1.6. We note that for all the three problem sets, the average degeneracy of the first excited state grows exponentially as a function of  $N$ , with an exponent of 0.311. This suggests roughly a doubling of the degeneracy of the first excited states with the addition of every two spins. This makes the problems at hand difficult to be solved using simulated annealing.

### 1.4.1.3. Ising formulation

In order for quantum annealing to solve them, the 2-SAT problems need to be mapped to a form that is suitable for the annealing algorithm. This is generally chosen to be the Ising model, and the mapping can be achieved using

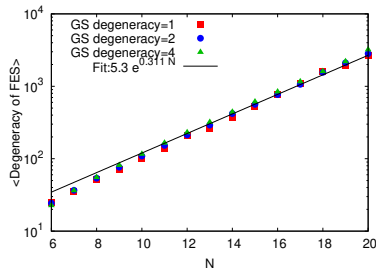


Figure 1.6.: Average degeneracy of the first excited state (FES) of the problem Hamiltonians with ground state (GS) degeneracy of 1, 2, and 4 for  $6 \leq N \leq 20$ .

$$H_{2SAT} = \sum_{\alpha=1}^M h_{2SAT}(\epsilon_{\alpha,1}x_{i[\alpha,1]}, \epsilon_{\alpha,2}x_{i[\alpha,2]}), \quad (1.27)$$

where  $i[\alpha, j]$  represents the variable  $i$  involved as the  $j$ th term in the  $\alpha$ th clause of the cost function,  $\epsilon = 1$  (-1) if the variable used is  $x_i$  ( $\bar{x}_i$ ). This mapping transforms each clause to a Hamiltonian function  $h_{2SAT}$  [Neu14a; Neu14b]. The resulting problems have a ground state degeneracy of one, two, or four and a highly degenerated first excited state. The Hamiltonians obtained from mapping 2-SAT problems to the Ising model consist of up to 2-local coupling terms, i.e., connectivity between the variables is sparse. This sparse connectivity of these problems make them easy to be embedded in real devices implementing quantum annealing.

An alternative representation for an optimization problem in order to be solved using quantum annealing is as a quadratic unconstrained binary optimization (QUBO) problem. A QUBO problem consists of a cost function  $C(x_1, x_2, \dots, x_N)$  defined over binary variables  $x_i = 0, 1$ ,

$$C(x_1, x_2, \dots, x_N) = \sum_{i \leq j} Q_{i,j} x_i x_j, \quad (1.28)$$

where  $Q$  is the QUBO matrix. The task at hand is to find an assignment to the variables  $x_i$  that minimizes the cost function  $C(x_1, x_2, \dots, x_N)$ .

There is an equivalence between the Ising and QUBO representation of a problem, both defined over binary variables. Using  $x_i = 1 - \sigma_i^z/2$ , we can map an Ising problem to a QUBO problem and vice-versa.

### 1.4.2. 2-SAT-derived problems

Using the sets of 2-SAT problems, it is possible to create new sets of problems that can exploit different properties of a real quantum annealer, and can therefore, as a collection, serve as useful benchmarks for quantum annealing. In this section, we discuss two problem classes derived from the 2-SAT problems with the ground state degeneracy of one.

### 1.4.2.1. Random-g problems

As discussed previously, employing quantum annealing for solving the 2-SAT problems requires them to be mapped to the Ising model, but this mapping is not uniquely defined. According to Eq. (1.27), each clause of the 2-SAT problems is mapped to a Hamiltonian term, which then contributes uniformly to the problem Hamiltonian with a weight equal to 1. We derive a new set of problems by randomly choosing different weights  $g_\alpha \in (0.5, 1.5]$  for each clause of the 2-SAT problems, such that

$$H_{2SAT} = \sum_{\alpha=1}^M g_\alpha h_{2SAT}(\epsilon_{\alpha,1} s_{i[\alpha,1]}, \epsilon_{\alpha,2} s_{i[\alpha,2]}), \quad (1.29)$$

in the hope that doing so can alter the difficulty of a given problem. For example, increasing the contribution of a clause that is difficult to be satisfied could make a SAT problem easier to be solved using quantum annealing (by altering the minimum energy gap), without changing its ground state. Using an appropriate optimization ansatz, it could then be possible to obtain values of  $g_\alpha$  that can make the problem easier to be solved using quantum annealing.

### 1.4.2.2. Multiple-copies problems

In our discussion, so far, the size of the considered problems has been limited to less than 20 variables. In the present section, we discuss a way of using the 2-SAT problems to create problems with a much larger number of variables. We combine multiple-copies of 12- and 18-variable 2-SAT problems in a chain-like manner to obtain the so-called multiple-copies problem. Different copies of the problems can additionally be connected to other copies through a ferromagnetic or an anti-ferromagnetic bond between the neighbouring copies. Furthermore, we explore two choices for the connecting variable between the copies: one of the least-connected or the most-connected variables from the graph, and connect it to the same variable of the neighboring copy. Since the ground state of the original 2-SAT problems is known, the solution to the multiple-copies problems is a simple concatenation of the solution to the original 2-SAT problem for the unconnected copies of the problem, copies connected through a ferromagnetic bond or an antiferromagnetic bond as long as the bond strength in the latter case is less than a certain threshold.

### 1.4.3. Fully-connected QUBO problems

All types of problems that have been considered so far have a sparse connectivity. Now, we shift our focus to the creation of problems with an all-to-all connectivity between the variables and problem sizes varying up to 200 variables. In this work, we consider two classes of fully-connected QUBO problems, namely the random problems and the regular problems [Meh+22b].

#### 1.4.3.1. Random problems

These problem instances are constructed by randomly choosing  $h$  and  $J$  values in the range  $[-1, 1]$ . The problem instances generated in this way are unrelated to one another.

Computing the ground state of these problems, or equivalently, the spin-glass problems, has been shown to be NP-hard [Bar82].

### 1.4.3.2. Regular problems

For these problems we construct the first problem instance by choosing couplings between qubits  $i$  and  $j$  such that  $J_{i,j} = (i + j)/(N - 1) - 1$  for  $i, j = 1, \dots, N$ . We find that the ground state of a Hamiltonian described in such a way is given by  $(x_1 = 1, \dots, x_k = 1, x_{k+1} = 0, \dots, x_N = 0)$ , where  $k$  is the integer that minimizes

$$f(k) = \sum_{1 \leq i \leq j \leq k} Q_{i,j} = \frac{k(N - k)(N - 2k + 2)}{N - 1}. \quad (1.30)$$

For a given  $N$ , more problem instances are then created by randomly reshuffling the indices  $i$  and  $j$ , which preserves the ground state energy and the ground state of the problem (apart from a simple reshuffling). Problem instances created in this way have the same problem graph except for the relabelling of the indices, and should be treated as the same problem by the D-Wave annealers.

An alternate way of creating more problems using the first regular problem for a given  $N$  is by using the spin-reversal transformation, where a spin  $i$  is randomly reversed, and  $h_i$  and  $J_{i,j}$  replaced by  $-h_i$  and  $-J_{i,j}$  so that the ground state energy of the QUBO problem remains unchanged.

### 1.4.3.3. Solving the fully-connected problems

In order to assess the performance of quantum annealing for solving the sets of fully-connected problems, we first need to determine the ground state of the problems. For the small QUBO problems ( $N \leq 58$ ), this is done by the means of a program called QUBO23 that enumerates all the  $2^N$  possible assignments of the binary variables  $x_1, \dots, x_N$ , and returns the assignments that have the lowest, the second lowest, and the largest costs. Although the ground states obtained from QUBO23 are the true ground states of the problems, the number of arithmetic operations required to enumerate all the possible states is proportional to  $N2^N$ , which makes this approach infeasible for larger problems.

For determining the ground states of problems up to  $N \leq 200$  we use two heuristic methods, namely qbsolv which is a heuristic solver offered by D-Wave, and the D-Wave Advantage 4.1 Hybrid solver. These solvers require much less time for finding the solution to the QUBO problem, however the ground state obtained from them cannot be proven to be the true ground state. The solution obtained for the smaller QUBO problems using QUBO23 is found to agree with that obtained from qbsolv and the D-Wave Hybrid solver. Furthermore, for the larger problems, where QUBO23 can no longer be employed, the ground states obtained with the two heuristic solvers match with one another for all the problem instances of the two classes up to  $N \leq 200$ .

## 1.5. Our focus

In this thesis, we study the performance of quantum annealing for solving optimization problems. As we have seen from the previous sections, quantum annealing is based on the principle of an adiabatic evolution starting from a certain initial state, which is chosen to be the ground state of the initial Hamiltonian, to the ground state of the final Hamiltonian, which encodes the optimization problem to be solved. According to the adiabatic theorem (Eq. (1.22)), the minimum energy gap between the ground state and the first excited state of the instantaneous Hamiltonian is a crucial quantity for the performance of quantum annealing. The smaller this gap, the longer will be the annealing time required to ascertain an adiabatic evolution of the state of the system. However, many of the hard optimization problems that are of practical interest, have minimum energy gaps that close exponentially as the number of variables in the problem increase, which poses a challenge to the performance of quantum annealing for solving such problems.

In this work, we assess the performance of the quantum annealing algorithm for mainly solving 2-satisfiability problems. We numerically introduce some modifications to the standard quantum annealing algorithm, and study their effects on the performance of quantum annealing for solving the given problems. Furthermore, we benchmark the D-Wave quantum annealers using various problems. Lastly, where applicable, we compare the performance of the ideal quantum annealing algorithm implemented numerically, with that of the D-Wave annealers.

This thesis has been organized as follows. We start by a brief revision of the numerical ingredients required for performing the simulations in Chapter 2. In Chapter 3 we benchmark two D-Wave systems for solving 2-SAT and other sets of problems derived from them and in Chapter 4 we discuss the performance of ideal quantum annealing and actual quantum annealers in terms of a relevant measure of performance, appropriate for the case of problems with more than one possible solution, namely the sampling probability of all the solutions. In the same chapter, we also discuss the reverse annealing protocol available in the D-Wave systems, and compare its performance with the simulations. We then introduce an additional Hamiltonian term, namely the trigger Hamiltonian, to the standard quantum annealing Hamiltonian, the results for which are presented in Chapter 5. We study the effects of adding two kinds of trigger Hamiltonians - the ferromagnetic and the antiferromagnetic trigger Hamiltonians, and compare their performance with the standard quantum annealing Hamiltonian for solving 2-SAT problems. Chapter 6 captures the effects of introducing the two kinds of trigger Hamiltonians on the distributions and scaling performance of various quantifiers of quantum annealing. In Chapter 7 we study the effects of modifying the initial Hamiltonian in the standard quantum annealing algorithm for solving the 2-SAT problems. Lastly, in Chapter 8 we present a summary and conclusion of this work.

## 2. Numerical methods

In this chapter, we provide the numerical ingredients that are essential for simulating quantum systems on a digital computer, simulations which form the basis for the work presented in this thesis. We start by discussing some general aspects for simulating such systems, and then move on to the methods for implementing the evolution of a quantum system, as well as for computing the energy spectrum of model Hamiltonians. We review the Crank-Nicolson algorithm and the Suzuki-Trotter product formula algorithm for solving the time-dependent Schrödinger equation (Eq. (1.21)), and the Lanczos algorithm for computing the energy spectrum of the Hamiltonian.

### 2.1. Essential operations

This section comprises some of the broad details that are commonly required for the implementation of any quantum algorithm. We start with the discussion of some essential operations that form the core of such simulations.

Any quantum mechanical operator acting on a state vector representing  $N$  qubits (Eq. (1.8)) can be expressed as a linear combination of products of the Pauli-matrices and the identity matrix which form the basis for a  $2^N \times 2^N$  operator. Thus, we can restrict ourselves to determine the action of  $\sigma_j^\alpha$ , where  $\alpha = x, y, z$ , acting on the  $j$ th qubit of the state vector Eq. (1.8). For example, the action of the operator  $\sigma_2^y$  on the  $N$ -qubit state vector is given as

$$\begin{aligned} \sigma_2^y |\psi\rangle &= a_0 \sigma_2^y |00\dots 00\rangle + a_1 \sigma_2^y |00\dots 01\rangle + \dots + a_{2^{N-2}} \sigma_2^y |11\dots 10\rangle + a_{2^{N-1}} \sigma_2^y |11\dots 11\rangle \\ &= ia_0 |00\dots 10\rangle + ia_1 |00\dots 11\rangle + \dots - ia_{2^{N-2}} |11\dots 00\rangle - ia_{2^{N-1}} |11\dots 01\rangle, \end{aligned} \quad (2.1)$$

where we have made use of the state representation given by Eq. (1.8) for the ease of understanding. It should also be noted that following the convention in computer science, in this notation the first qubit corresponds to the least significant bit of the integer index that runs from zero to  $2^N - 1$ . Even though the operator  $\sigma_j^\alpha$  only acts on the  $j$ th qubit, all the  $2^N$  coefficients need to be updated as a consequence.

#### 2.1.1. Single-qubit operations

We will now discuss how the amplitudes of the state vector are updated under the action of a single-qubit operator  $\sigma_j^\alpha$  where  $\alpha = x, y, z$ . For this purpose, we write the  $N$ -qubit state vector as

$$|\psi\rangle = a(00\dots 00) |00\dots 00\rangle + a(00\dots 01) |00\dots 01\rangle + a(11\dots 10) |11\dots 10\rangle + a(11\dots 11) |11\dots 11\rangle, \quad (2.2)$$

where the coefficients  $a_i$  from Eq. (1.8) are expressed in terms of the binary representation of the corresponding index  $i$ . In addition, we define

$$\begin{aligned} |\psi'\rangle &= \sigma_j^\alpha |\psi\rangle \\ &= a'(00\dots00)|00\dots00\rangle + a'(00\dots01)|00\dots01\rangle + a'(11\dots10)|11\dots10\rangle + a'(11\dots11)|11\dots11\rangle. \end{aligned} \quad (2.3)$$

As  $\sigma_j^z$  is a diagonal matrix in the computational basis, i.e., the computational basis is spanned by the eigenvectors of  $\sigma^z$ , the action of  $\sigma_j^z$  is to simply invert the sign of the coefficients for which  $j$ th bit is 1, i.e.,

$$\begin{aligned} a'(*\dots*0*\dots*) &= a(*\dots*0*\dots*) \\ a'(*\dots*1*\dots*) &= -a(*\dots*1*\dots*), \end{aligned} \quad (2.4)$$

where the asterisk signifies that the bits at the corresponding places remain unchanged. Focusing next on the operator  $\sigma_j^x$ , we recall that this operator swaps bit 0 to 1, and vice-versa, and hence

$$\begin{aligned} a'(*\dots*0*\dots*) &= a(*\dots*1*\dots*) \\ a'(*\dots*1*\dots*) &= a(*\dots*0*\dots*). \end{aligned} \quad (2.5)$$

This implies that under the action of  $\sigma_j^x$ , the coefficients corresponding to bits 0 and 1 at position  $j$  get interchanged. Lastly, the effect of applying  $\sigma_j^y$  on the state vector combines the effects of applying  $\sigma_j^x$  followed by  $\sigma_j^z$  on the state vector, apart from a global phase of  $e^{-i\pi/2}$ , i.e., it swaps bit 0 to 1, and vice-versa, and reverses the sign of the coefficient if the bit at the  $j$ th position is 1. Thus, we obtain

$$\begin{aligned} a'(*\dots*0*\dots*) &= -ia(*\dots*1*\dots*) \\ a'(*\dots*1*\dots*) &= ia(*\dots*0*\dots*). \end{aligned} \quad (2.6)$$

Following this approach all the single-qubit operations can be performed in place, i.e., without using another multi-qubit state vector of length  $2^N$ . With the three operators discussed above, it is possible to construct the simulations for any quantum algorithm requiring to compute the product  $H|\psi\rangle$  without having to store the corresponding Hamiltonian matrices whose size grows exponentially as  $2^{2N}$  with the number of qubits.

### 2.1.2. Two-qubit operators

Next, we focus on the two-qubit operators. Although the two-qubit spin operators  $\sigma_j^\alpha \sigma_k^\alpha$  can be written as product of the two single-qubit spin operators, this approach is not very efficient when one needs to compute the two-qubit operators for many pairs of  $j$  and  $k$ . In this case, one would either have to compute  $\sigma_k^\alpha |\psi\rangle$  many times, or would have to use extra memory in order to store  $\sigma_k^\alpha |\psi\rangle$ . Therefore, we briefly discuss the numerical implementation of the two-qubit spin operators. As before, denoting  $|\psi\rangle'' = \sigma_j^\alpha \sigma_k^\alpha |\psi\rangle$ , for  $\alpha = z$  only the sign of the coefficients with different bits at positions  $j$  and  $k$  are inverted,

and thus we obtain

$$\begin{aligned}
 a''(*\dots * 0 * \dots * 0 * \dots) &= a(*\dots * 0 * \dots * 0 * \dots) \\
 a''(*\dots * 0 * \dots * 1 * \dots) &= -a(*\dots * 0 * \dots * 1 * \dots) \\
 a''(*\dots * 1 * \dots * 0 * \dots) &= -a(*\dots * 1 * \dots * 0 * \dots) \\
 a''(*\dots * 1 * \dots * 1 * \dots) &= a(*\dots * 1 * \dots * 1 * \dots).
 \end{aligned} \tag{2.7}$$

When  $\alpha = x$ , the coefficients with complementary values of the bits at positions  $j$  and  $k$  get interchanged, i.e.,

$$\begin{aligned}
 a''(*\dots * 0 * \dots * 0 * \dots) &= a(*\dots * 1 * \dots * 1 * \dots) \\
 a''(*\dots * 0 * \dots * 1 * \dots) &= a(*\dots * 1 * \dots * 0 * \dots) \\
 a''(*\dots * 1 * \dots * 0 * \dots) &= a(*\dots * 0 * \dots * 1 * \dots) \\
 a''(*\dots * 1 * \dots * 1 * \dots) &= a(*\dots * 0 * \dots * 0 * \dots).
 \end{aligned} \tag{2.8}$$

As before, the  $\alpha = y$  two-qubit operator combines the phase flip and the bit flip operations, so that we have

$$\begin{aligned}
 a''(*\dots * 0 * \dots * 0 * \dots) &= -a(*\dots * 1 * \dots * 1 * \dots) \\
 a''(*\dots * 0 * \dots * 1 * \dots) &= a(*\dots * 1 * \dots * 0 * \dots) \\
 a''(*\dots * 1 * \dots * 0 * \dots) &= a(*\dots * 0 * \dots * 1 * \dots) \\
 a''(*\dots * 1 * \dots * 1 * \dots) &= -a(*\dots * 0 * \dots * 0 * \dots).
 \end{aligned} \tag{2.9}$$

An alternative approach for implementing the two-qubit spin operators for  $\alpha = x, y$  is by making use of the rotation operators  $R_j^\alpha(\theta)$  which transform  $\sigma_j^z$  to  $\sigma_j^\alpha$ , so that we can write

$$\sigma_j^\alpha \sigma_k^\alpha |\psi\rangle = R_j^\alpha(\theta) R_k^\alpha(\theta) \sigma_j^z \sigma_k^z (R_j^\alpha(\theta))^\dagger (R_k^\alpha(\theta))^\dagger |\psi\rangle. \tag{2.10}$$

It is straightforward to simulate the action of the two-qubit operator  $\sigma_j^z \sigma_k^z$  on the wavefunction as the update rules for the amplitudes of the new state do not depend on the amplitudes corresponding to the other basis vectors. We note that  $\sigma_j^x = (R_j^y(\pi/2))^\dagger \sigma_j^z R_j^y(\pi/2)$  and  $\sigma_j^y = R_j^x(\pi/2) \sigma_j^z (R_j^x(\pi/2))^\dagger$ , where the rotation matrices are obtained using Eq. (1.12) and read

$$R^x(\pi/2) = e^{i\pi\sigma^x/2} = \frac{1}{\sqrt{2}} \begin{pmatrix} 1 & i \\ i & 1 \end{pmatrix}, \quad R^y(\pi/2) = e^{i\pi\sigma^y/2} = \frac{1}{\sqrt{2}} \begin{pmatrix} 1 & 1 \\ -1 & 1 \end{pmatrix}. \tag{2.11}$$

The inverse rotations  $(R_j^x(\pi/2))^\dagger$  and  $(R_j^y(\pi/2))^\dagger$  are then obtained by determining  $R_j^x(-\pi/2)$  and  $R_j^y(-\pi/2)$ , respectively.

The update rules for computing the action of the rotation operators  $R_j^x(\pi/2)$  and  $R_j^y(\pi/2)$  can be obtained using the matrix representations of these operators given by Eq. (2.11). For example, for state  $|\psi\rangle' = (R_j^y(\pi/2))^\dagger |\psi\rangle$ , we have

$$\begin{aligned}
 a'(*\dots * 0 * \dots) &= \frac{1}{\sqrt{2}} [a(*\dots * 0 * \dots) - a(*\dots * 1 * \dots)] \\
 a'(*\dots * 1 * \dots) &= \frac{1}{\sqrt{2}} [a(*\dots * 0 * \dots) + a(*\dots * 1 * \dots)].
 \end{aligned} \tag{2.12}$$

## 2.2. Solving the TDSE

All the operators that have been discussed so far share the property of being unitary, and therefore, they conserve the norm of the state vector. Since any nonsingular matrix can be written as the matrix exponential of a Hermitian matrix, and unitary matrices are nonsingular, any unitary matrix  $U$  can be expressed as  $U = e^{-itH}$ , where  $H$  is a Hermitian matrix. The change in the state of a system as a consequence of the application of this unitary operator physically corresponds to the time evolution of a quantum system under a given Hamiltonian  $H$ . The time-dependent Schrödinger equation (TDSE) describes this time evolution as

$$i \frac{\partial}{\partial t} |\psi(t)\rangle = H(t) |\psi(t)\rangle, \quad (2.13)$$

where we have set  $\hbar = 1$ , and use dimensionless quantities in our simulations.

The formal solution of the TDSE is given by

$$|\psi(t+t')\rangle = U(t+t', t) |\psi(t)\rangle = \exp_+ \left( -i \int_t^{t+t'} H(u) du \right) |\psi(t)\rangle, \quad (2.14)$$

where  $t'$  denotes some interval of time, and the unitary time-ordered matrix exponential  $U = \exp_+ \left( -i \int_t^{t+t'} H(u) du \right)$  is defined as

$$\begin{aligned} \exp_+ \left( -i \int_t^{t+t'} H(u) du \right) &= 1 + (-i) \int_t^{t+t'} du_1 H(u_1) + (-i)^2 \int_t^{t+t'} du_1 \int_t^{u_1} du_2 H(u_1) H(u_2) \\ &\quad + (-i)^3 \int_t^{t+t'} du_1 \int_t^{u_1} du_2 \int_t^{u_2} du_3 H(u_1) H(u_2) H(u_3) + \dots \end{aligned} \quad (2.15)$$

Since truncating series Eq. (2.15) at some point would lead to a non-unitary approximation of the time evolution operator  $U(t+t', t)$ , Eq. (2.15) is not useful for its numerical implementation. Instead, approximating the time-dependent Hamiltonian as being piecewise constant, we divide the time interval  $t'$  in  $m$  steps  $\tau_j$ , such that  $\sum_{j=1}^m \tau_j = t'$ , and the Hamiltonian relatively stays constant over the interval  $[t_j, t_{j+1})$  where  $t_j = t + \sum_{k=1}^j \tau_k$ . Thus,

$$U(t+t', t) = U(t_m, t_{m-1}) U(t_{m-1}, t_{m-2}) \dots U(t_1, t_0), \quad (2.16)$$

and we proceed by approximating each  $U(t_j, t_{j-1})$  as

$$U(t_j, t_{j-1}) \approx e^{-i\tau_j H(t_{j-1} + \tau_j/2)}. \quad (2.17)$$

One needs to compute the matrix exponentials given by Eq. (2.17) for solving the TDSE. In case of time-independent Hamiltonians, we can write  $U(\tau) = \exp(-i\tau H)$ , where we have assumed  $\tau_j = \tau$  for all  $j$  in order to simplify the notation. The most straightforward algorithm to solve the TDSE is the full diagonalization method, where the Hamiltonian matrix  $H$  is created at every step of discretized time. We then need to determine the

unitary matrix  $V$  consisting of the eigenvectors of  $H$  and matrix  $\lambda$  consisting of the real-valued eigenvalues. Since matrix  $H$  becomes a diagonal matrix when expressed in its eigenbasis, i.e.,  $V^\dagger H V = \lambda$ ,  $U(\tau) = e^{-i\tau H} = V e^{-i\tau \lambda} V^\dagger$ , the time evolution operator can be computed by a simple matrix multiplication. However, for a  $D \times D$  matrix, the memory and the CPU time of the standard diagonalization algorithms scale as  $D^2$  and  $D^3$ , respectively [Wil65; GV96; Par98]. Since the size of the Hamiltonian matrix grows as  $2^N \times 2^N$  with the number of spins  $N$ , the method becomes infeasible already for a rather small number of spins due to the limited computational resources.

There are several algorithms that have been devised to alleviate this problem, for example, the Crank-Nicolson algorithm, Chebyshev polynomial algorithm [TK84; DD03; Wei+06], Lanczos iterative algorithm [Pav+11; SRS20], and Suzuki-Trotter product formula algorithm [De 87]. In the following sections we discuss some of these algorithms for constructing approximations to the exponential in Eq. (2.17).

At this point, we would like to mention that in this work, we restrict ourselves to quantum systems that have discrete Hamiltonians that can be expressed in terms of the Pauli operators. For a discussion of quantum Hamiltonians in real space, see appendix D.

### 2.2.1. Crank-Nicolson algorithm

The Crank-Nicolson method was devised for numerically solving heat equations [CN47], but can also be employed for solving similar partial differential equations. In this section we review the basics of the algorithm, and determine the bound on the error resulting from approximating the time evolution operator.

We start from Eq. (2.14) and split the time step  $\tau$  over which the wavefunction is allowed to evolve in half, so that

$$|\psi(t + \tau)\rangle = U(t + \tau, t + \tau/2)U(t + \tau/2, t)|\psi(t)\rangle. \quad (2.18)$$

Multiplying both sides by  $U^{-1}(t + \tau, t + \tau/2)$ , we obtain

$$U^{-1}(t + \tau, t + \tau/2)|\psi(t + \tau)\rangle = U(t + \tau/2, t)|\psi(t)\rangle, \quad (2.19)$$

and since the time evolution operator is unitary,

$$U^\dagger(t + \tau, t + \tau/2)|\psi(t + \tau)\rangle = U(t + \tau/2, t)|\psi(t)\rangle, \quad (2.20)$$

where the formal definition of the time evolution operator is given by Eq. (2.15). Restricting up to first-order accurate terms in  $\tau$  gives

$$\left(1 + i \int_{t+\tau/2}^{t+\tau} du_1 H(u_1)\right)|\psi(t + \tau)\rangle = \left(1 - i \int_t^{t+\tau/2} du_1 H(u_1)\right)|\psi(t)\rangle + \mathcal{O}(\tau^2). \quad (2.21)$$

Specializing to the case of time-independent Hamiltonians, and only keeping terms up to first order in  $\tau$ , Eq. (2.20) becomes

$$\left(1 + iH\tau/2\right)|\psi(t + \tau)\rangle = \left(1 - iH\tau/2\right)|\psi(t)\rangle + \mathcal{O}(\tau^2). \quad (2.22)$$

Thus,

$$\begin{aligned} |\psi(t + \tau)\rangle &\approx (1 + iH\tau/2)^{-1}(1 - iH\tau/2)|\psi(t)\rangle \\ &\equiv U_{CN}(\tau)|\psi(t)\rangle. \end{aligned} \quad (2.23)$$

Since  $H$  is Hermitian,

$$U_{CN}^\dagger(\tau) = (1 + iH\tau/2)(1 - iH\tau/2)^{-1}, \quad (2.24)$$

and thus

$$U_{CN}^\dagger(\tau)U_{CN}(\tau) = U_{CN}(\tau)U_{CN}^\dagger(\tau) = \mathbb{I}, \quad (2.25)$$

i.e., this approximation to the time evolution operator is unitary, implying that this method is unconditionally stable.

Applying this method  $m$  times yields an approximation to the wavefunction evolving for  $t' = m\tau$  time. The error accumulated in  $m$  applications of the method is of the order  $\mathcal{O}(\tau^{-2})$ , as shown in Appendix E.

The Crank-Nicolson method is an implicit method because it requires the calculation of the inverse of the matrix  $(1 + iH\tau/2)$ . Except for matrices with a very special structure (e.g., tridiagonal see Appendix D), this feature renders this method inefficient (in general the number of arithmetic operations scales as  $2^{6N}$ ).

## 2.2.2. Suzuki-Trotter product formula algorithm

The Suzuki-Trotter product formula algorithm is one of the most efficient and commonly used algorithms for solving the TDSE [Tro59; Suz76; SMK77; Suz85; DD83; De 87; Suz91]. Generally, the Hamiltonian matrix is a sparse matrix, and can be decomposed as

$$H = \sum_{k=1}^K H_k, \quad (2.26)$$

where  $H_k$  only consists of the local (i.e., one- and two-qubit) terms. Using the Trotter formula, the evolution operator can be written as [Tro59; Suz76]

$$U(t + t', t) = e^{-it'H} = e^{-it'(H_1 + H_2 + \dots + H_K)} = \lim_{m \rightarrow \infty} \left( \prod_{k=1}^K e^{-it'H_k/m} \right)^m. \quad (2.27)$$

As before, we define  $U(\tau) = \exp(-i\tau H_k)$ , where  $\tau = t'/m$ , such that by applying  $U(\tau)$   $m$  times one obtains  $U(t)$ .

The first-order approximation to  $U(\tau)$  can be constructed as [Suz76; Suz85; Suz91]

$$\tilde{U}_1(\tau) = e^{-i\tau H_1} \dots e^{-i\tau H_K}. \quad (2.28)$$

The accumulated error from the implementation of the first-order approximation shows a linear dependence on the time step  $\tau$  (see Appendix E for the derivation).

This error bound can be made tighter ( $\mathcal{O}(\tau^{-2})$ ), if we adopt instead the second order approximant  $\tilde{U}_2(\tau)$  for the time evolution operator  $U(\tau)$ . There are many choices for

defining  $\tilde{U}_2(\tau)$ , but here we choose the symmetrized product formula algorithm [DD83] defined as

$$\tilde{U}_2(\tau) = \tilde{U}_1^\dagger(-\tau/2)\tilde{U}_1(\tau/2) = e^{-i\tau H_K/2} \dots e^{-i\tau H_1/2} e^{i\tau H_1/2} \dots e^{-i\tau H_K/2}. \quad (2.29)$$

The derivation for the bound on the error involved in implementing the second order approximant is given in Appendix E.

### Practical implementation

Moving next to a practical point of view, the decomposition of the Hamiltonian matrix is chosen in such a way that the  $K$  resulting matrices are diagonal or block-diagonal so that it is possible to evaluate  $e^{-i\tau H_k} |\psi\rangle$  without constructing the full matrix and performing only  $l$ -components updates, for a small integer  $l$ . Then, in the case of the  $D \times D$  diagonal matrices  $H_k$ , the matrix exponentiation is straightforward, since

$$e^{-i\tau H_k} = \exp\left(-i\tau \begin{pmatrix} \lambda_k^{(0)} & & \\ & \ddots & \\ & & \lambda_k^{(D-1)} \end{pmatrix}\right) = \begin{pmatrix} e^{-i\tau \lambda_k^{(0)}} & & \\ & \ddots & \\ & & e^{-i\tau \lambda_k^{(D-1)}} \end{pmatrix}, \quad (2.30)$$

where  $\lambda_k^j$  with  $j = 0, \dots, D-1$  are the  $D$  eigenvalues of the diagonal matrix  $H_k$ . Thus, for computing  $e^{-i\tau H_k} |\psi\rangle$  we simply need to multiply each coefficient  $a_j$  of the state vector  $|\psi\rangle$  given by Eq. (1.8) with  $e^{-i\tau \lambda_k^{(j)}}$ . For this choice to be efficient, the matrices have to be chosen with care so that they are straightforward to diagonalize, or otherwise they can lead to a tremendous increase in the computational resources.

For a block-diagonal matrix  $H_k$  with  $L$  blocks  $H_{k'}^{(l)}$ , on the other hand, we get

$$e^{-i\tau H_k} = \exp\left(-i\tau \begin{pmatrix} H_{k'}^{(0)} & & \\ & \ddots & \\ & & H_{k'}^{(L-1)} \end{pmatrix}\right) = \begin{pmatrix} e^{-i\tau H_{k'}^{(0)}} & & \\ & \ddots & \\ & & e^{-i\tau H_{k'}^{(L-1)}} \end{pmatrix}. \quad (2.31)$$

Generally, the block-diagonal matrices  $H_k$  are chosen so that they have  $4 \times 4$  or  $2 \times 2$  blocks  $H_{k'}^{(l)}$ . The latter can be expressed in the standard basis for the vector space of  $2 \times 2$  matrices, that is the Pauli-matrices, i.e.,

$$H_{k'}^{(l)} = v_x \sigma^x + v_y \sigma^y + v_z \sigma^z. \quad (2.32)$$

Using the Euler formula, we can therefore write

$$e^{-i\tau H_{k'}^{(l)}} = e^{-i\tau \mathbf{v} \cdot \boldsymbol{\sigma}} = \mathbb{I} \cos(\tau v) - i \frac{\mathbf{v} \cdot \boldsymbol{\sigma}}{v} \sin(\tau v), \quad (2.33)$$

where  $\mathbf{v} = (v_x, v_y, v_z)^T$ ,  $\boldsymbol{\sigma} = (\sigma^x, \sigma^y, \sigma^z)^T$ , and  $v = \sqrt{v_x^2 + v_y^2 + v_z^2}$ . The update rules for the involved coefficients  $a_j$  and  $a_k$  of the state vector given by Eq. (1.8) then obtained using Eq. (2.33) read

$$\begin{aligned} a'_j &= \left( \cos(\tau v) - i \sin(\tau v) \frac{v_z}{v} \right) a_j - i \sin(\tau v) \frac{v_x - i v_y}{v} a_k \\ a'_k &= -i \sin(\tau v) \frac{v_x + i v_y}{v} a_j + \left( \cos(\tau v) + i \sin(\tau v) \frac{v_z}{v} \right) a_k. \end{aligned} \quad (2.34)$$

Since the computational basis is the eigenbasis for  $\sigma^z$  operator, its contributions can instead be included in the diagonal matrix, and use of Eq. (2.30) can be made to solve for the matrix exponential. In this case,  $v_z = 0$ , and Eq. (2.34) becomes

$$\begin{aligned} a'_j &= \cos(\tau v) a_j - i \sin(\tau v) \frac{v_x - i v_y}{v} a_k \\ a'_k &= -i \sin(\tau v) \frac{v_x + i v_y}{v} a_j + \cos(\tau v) a_k. \end{aligned} \quad (2.35)$$

We employ the second-order product formula algorithm for implementing the dynamics of the system under the quantum annealing Hamiltonian. In our work, we decompose the general time-dependent Hamiltonian

$$\begin{aligned} H(t) &= A(t) \sum_{i=1}^N h_i^x \sigma_i^x + B(t) \sum_{1=i < j = N} J_{i,j}^x \sigma_i^x \sigma_j^x + C(t) \sum_{i=1}^N h_i^y \sigma_i^y + D(t) \sum_{1=i < j = N} J_{i,j}^y \sigma_i^y \sigma_j^y \\ &\quad + E(t) \sum_{i=1}^N h_i^z \sigma_i^z + F(t) \sum_{1=i < j = N} J_{i,j}^z \sigma_i^z \sigma_j^z, \end{aligned} \quad (2.36)$$

as

$$H(t) = H_{single} + H_{xx} + H_{yy} + H_{zz}, \quad (2.37)$$

where  $H_{single}$  consists of only the single spin terms, i.e.,

$$H_{single} = A(t) \sum_{i=1}^N h_i^x \sigma_i^x + C(t) \sum_{i=1}^N h_i^y \sigma_i^y + E(t) \sum_{i=1}^N h_i^z \sigma_i^z, \quad (2.38)$$

while  $H_{xx}$ ,  $H_{yy}$  and  $H_{zz}$  consist of  $x$ - $x$ ,  $y$ - $y$  and  $z$ - $z$  interaction terms, respectively. We use Eq. (2.34) for solving the matrix exponential  $e^{-i\tau H_{single}}$ . For computing the contribution of  $H_{zz}$  in the time evolution of the state, we employ Eq. (2.30), which reduces to a simple multiplication of the coefficients  $a_j$  of the state vector given by Eq. (1.8) by  $e^{-i\tau \lambda_z^{(j)}}$ , where  $\lambda_z^{(j)}$  are the eigenvalues of  $H_{zz}$ . For evaluating the exponentials  $e^{-i\tau H_{xx}}$  and  $e^{-i\tau H_{yy}}$ , we first make use of the rotation matrices to transform the wavevector to the eigenbasis of  $H_{xx}$  and  $H_{yy}$ , respectively. This can be achieved by using the products of rotation matrices,  $R^y = \prod_{j=1}^N R_j^y(\pi/2)$  and  $(R^x)^\dagger = \prod_{j=1}^N (R_j^x(\pi/2))^\dagger$ , where matrices  $R_j^x(\pi/2)$  and  $R_j^y(\pi/2)$  are given by Eq. (2.11). In this new basis, the action of the exponentials  $e^{-i\tau H_{xx}}$  and  $e^{-i\tau H_{yy}}$  is straightforward to calculate, as was the case for computing the contribution for the  $H_{zz}$  term. Using the inverse matrix rotations,  $(R^y)^\dagger = \prod_{j=1}^N (R_j^y(\pi/2))^\dagger$  and  $R^x = \prod_{j=1}^N R_j^x(\pi/2)$  the resulting vector can be transformed back to the computational basis. Thus, to summarize, we have

$$\begin{aligned} e^{-itH^{xx}} &= (R^y)^\dagger \exp\left(it \sum_{i,j=1}^N J_{i,j}^x \sigma_i^x \sigma_j^x\right) R^y, \\ e^{-itH^{yy}} &= R^x \exp\left(it \sum_{i,j=1}^N J_{i,j}^y \sigma_i^y \sigma_j^y\right) (R^x)^\dagger. \end{aligned} \quad (2.39)$$

On a separate note, the Suzuki-Trotter product formula algorithm can also be used to perform quantum simulations on quantum computers, which can naturally allow for more efficient realizations of such system. A more detailed discussion of the same is given in Appendix F.

## 2.3. Lanczos algorithm for solving the spectrum

The Lanczos algorithm is an iterative method for finding approximations to the  $K$  ( $\leq D$ ) lowest or highest eigenvalues and eigenvectors of a  $D \times D$  Hermitian matrix [Wil65; GV96; CW02; Pav+11]. The usefulness of this method depends on the number of required eigenvalues and eigenvectors  $K$ , which should satisfy  $K \ll D = 2^N$  for this method to compete with exact diagonalization.

### 2.3.1. Repeated minimization in two-dimensional Krylov subspace

Consider a Hamiltonian  $H$  corresponding to a quantum system whose ground state we wish to calculate. We start by creating an orthonormal basis spanned by two vectors  $|v_0\rangle$  and  $|v_1\rangle$ , using an initial vector  $|\psi\rangle$ , as follows. The first vector is created by normalizing the initial wavevector, i.e.,

$$|v_0\rangle = \frac{|\psi\rangle}{\sqrt{\langle\psi|\psi\rangle}}, \quad (2.40)$$

and the second by applying the Hamiltonian on  $|v_0\rangle$  and orthogonalizing,

$$|\tilde{v}_1\rangle = H|v_0\rangle - \langle v_0|H|v_0\rangle|v_0\rangle. \quad (2.41)$$

Defining  $b_n = \sqrt{\langle\tilde{v}_n|\tilde{v}_n\rangle}$ , and  $a_n = \langle v_n|H|v_n\rangle$ , the normalized second basis vector becomes

$$|v_1\rangle = \frac{|\tilde{v}_1\rangle}{b_1}, \quad (2.42)$$

and hence

$$H|v_0\rangle = b_1|v_1\rangle + a_0|v_0\rangle, \quad (2.43)$$

and

$$b_1 = \langle v_1|H|v_0\rangle = \langle v_0|H|v_1\rangle, \quad (2.44)$$

where the last relation is motivated by the fact that  $b_n$  are real numbers.

Now, using this orthonormal basis, we can write any normalized wavefunction as

$$|v\rangle = \cos\theta|v_0\rangle + \sin\theta|v_1\rangle, \quad (2.45)$$

the energy expectation value of which is then given by

$$\langle v|H|v\rangle = a_0 \cos^2(\theta) + 2b_1 \cos(\theta) \sin(\theta) + a_1 \sin^2(\theta). \quad (2.46)$$

To find the wavefunction with the smallest energy in this subspace, given by the initial vector  $|\psi\rangle$ , Eq. (2.46) is differentiated with respect to  $\theta$  and set to zero, and we thus obtain,

$$-b_1 \tan^2\theta + (a_1 - a_0) \tan\theta + b_1 = 0. \quad (2.47)$$

Solving Eq. (2.47), we obtain the minimum energy wavefunction  $|\psi^{(2)}\rangle$  in the space spanned by vectors  $|v_0\rangle$  and  $H|v_0\rangle$ , where

$$|\psi^{(2)}\rangle = \cos\theta_{min}|v_0\rangle + \sin\theta_{min}|v_1\rangle. \quad (2.48)$$

This is equivalent to diagonalizing the matrix  $H'$  in the subspace spanned by vectors  $|\psi\rangle$  and  $H|\psi\rangle$ , which is given as

$$H' = \begin{pmatrix} a_0 & b_1 \\ b_1 & a_1 \end{pmatrix}. \quad (2.49)$$

Starting the next iteration from  $|\psi^{(2)}\rangle$ , we can again find the wavefunction corresponding to the minimum energy in the subspace spanned by  $|\psi^{(2)}\rangle$  and  $H|\psi^{(2)}\rangle$ . Repeating this procedure  $L$  times, starting from the vector  $|v_0\rangle$ , we can find the wavefunction that lies in the  $L+1$ -order Krylov subspace  $\mathcal{K}^{L+1}(H, |v_0\rangle) = \text{span}(|v_0\rangle, H|v_0\rangle, H^2|v_0\rangle, \dots, H^L|v_0\rangle)$ , and successively converges towards the ground state of the given Hamiltonian [Hou13].

### 2.3.2. Minimization in L-dimensional Krylov subspace

Instead of repeatedly minimizing the wavevector in two-dimensional subspace  $L$  times, we can define a vector in the Krylov subspace  $\mathcal{K}^{L+1}(H, |v_0\rangle)$  and find a wavefunction that minimizes the energy directly over this subspace, since more degrees of freedom will lead to a faster convergence.

For constructing the orthonormal basis with the vectors from the Krylov space, we start again by normalizing the initial vector  $|\psi\rangle$  as in Eq. (2.40), and orthogonalizing the second vector obtained by applying the Hamiltonian on the first as in Eq. (2.41). The subsequent vectors are created using  $H|v_n\rangle$  and orthogonalizing to all the previous vectors, i.e.,

$$b_2 |v_2\rangle = |\tilde{v}_2\rangle = H|v_1\rangle - a_1 |v_1\rangle - b_1 |v_0\rangle, \quad (2.50)$$

where  $a_n = \langle v_n | H | v_n \rangle$  and  $b_n = \langle \tilde{v}_n | \tilde{v}_n \rangle$ . Similarly,

$$b_3 |v_3\rangle = |\tilde{v}_3\rangle = H|v_2\rangle - a_2 |v_2\rangle - b_2 |v_1\rangle - \langle v_0 | H | v_2 \rangle |v_0\rangle. \quad (2.51)$$

However, from Eq. (2.43), we obtain  $\langle v_2 | H | v_0 \rangle = 0$  as  $\langle v_2 | v_1 \rangle = \langle v_2 | v_0 \rangle = 0$  by construction, and thus

$$b_3 |v_3\rangle = H|v_2\rangle - a_2 |v_2\rangle - b_2 |v_1\rangle. \quad (2.52)$$

Similarly, for the following basis vectors the contributions from the vectors other than the previous two vanish, and we obtain

$$b_{n+1} |v_{n+1}\rangle = H|v_n\rangle - a_n |v_n\rangle - b_n |v_{n-1}\rangle. \quad (2.53)$$

In the Krylov subspace, the Hamiltonian matrix reads

$$H' = \begin{pmatrix} a_0 & b_1 & 0 & 0 & & 0 & 0 \\ b_1 & a_1 & b_2 & 0 & \dots & 0 & 0 \\ 0 & b_2 & a_2 & b_3 & & 0 & 0 \\ 0 & 0 & b_3 & a_3 & & 0 & 0 \\ & \vdots & & & \ddots & & \\ 0 & 0 & 0 & 0 & & a_{L-1} & b_L \\ 0 & 0 & 0 & 0 & & b_L & a_L \end{pmatrix}. \quad (2.54)$$

Diagonalizing this tridiagonal matrix yields a good approximation to the lowest  $K$  eigenvalues of the Hamiltonian matrix, where  $K < L \ll 2^N$ .

### Practical implementation

In the numerical implementation of the algorithm, a limited numerical precision makes the Lanczos vector  $|v_n\rangle$  to have a finite overlap with the previous vectors  $|v_m\rangle$  where  $m \leq n-2$ . This loss of orthogonality of the Lanczos vectors presents itself as multiple copies of the eigenvectors, which are unrelated to actual degeneracies of these eigenvectors for the given Hamiltonian. To overcome this, we explicitly orthogonalize each Lanczos vector to all the previously obtained Lanczos vectors, to account for limited numerical precision. In order to do this, all the Lanczos vectors need to be stored.

Although the Hamiltonian matrix is generally sparse, and thus the product  $H|v_n\rangle$  can be calculated efficiently, the storage of such a large matrix can be entirely avoided by decomposing the Hamiltonian  $H$  such that the action of the components of this decomposed Hamiltonian on the vector  $|v_n\rangle$  can be easily calculated. In this work, we use the Lanczos algorithm to determine the energy spectrum of the Hamiltonian, which is an essential tool for analyzing the mechanisms involved during the evolution of the system. Furthermore, as seen from the adiabatic equation Eq. (1.22), the minimum energy gap between the ground state and the first excited state of the annealing Hamiltonian is crucial for the performance of quantum annealing.

For implementing the Lanczos algorithm, we decompose the Hamiltonian as  $H = H'_x + H'_y + H'_z$ , where  $H'_\alpha = \sum_{i=1}^N h_i^\alpha \sigma_i^\alpha + \sum_{i<j=1}^N J_{i,j}^\alpha \sigma_i^\alpha \sigma_j^\alpha$ , for  $\alpha = x, y, z$ . The action of  $H'_z$  on a Lanczos vector  $|v_n\rangle = \sum_{i=0}^{2^N-1} a_i |i\rangle$  is straightforward to compute, since  $|i\rangle$  forms the computational basis, which is also the eigenbasis of  $\sigma_i^z$ . For calculating  $H'_x|v_n\rangle$  and  $H'_y|v_n\rangle$  we again make use of the rotation matrices, as discussed above, by writing  $\sigma_i^x = (R_i^y(\pi/2))^\dagger \sigma_i^z R_i^y(\pi/2)$  and  $\sigma_i^y = R_i^x(\pi/2) \sigma_i^z (R_i^x(\pi/2))^\dagger$ . This approach is also adopted for calculating the Hamiltonian matrix and state vector products for computing the energy expectation value for the instantaneous state  $|\psi\rangle$  which is given as  $\langle\psi|H|\psi\rangle$ . Combined with the spectrum of the Hamiltonian, the energy expectation values can help to visualize the evolution of the state of the system under a time-dependent Hamiltonian.



### 3. Assessing the performance of the D-Wave systems

To date, the largest available commercial analog quantum computers are the quantum annealers offered by D-Wave Quantum Systems Inc., with their latest system providing access to more than 5000 qubits [MF20]. The hardware of a quantum processing unit (QPU) consists of an array of tunable coupled rf-superconducting quantum-interference device (rf-SQUID) qubits [Har+10]. Each qubit and the coupler of the D-Wave QPU can be controlled by the means of separate digital-to-analog-converters (DACs) [Joh+10; Bun+14a]. However, despite many improvements in the design and connectivity of the D-Wave quantum annealers over the years, these annealers are far from being ideal systems. The two main sources of imperfection in these systems are temperature and noise effects. While the former bolsters non-adiabatic evolution of the state of the system, the latter can result in an infidelity in the problem representation. In other words, instead of solving the specified Ising-type problem Hamiltonian with given problem parameters  $h$  and  $J$  according to Eq. (1.17), the QPU solves a slightly different problem, namely

$$H'_P = - \sum_{i=1}^N (h_i^z + \delta h_i^z) \sigma_i^z - \sum_{\langle i,j \rangle} (J_{i,j}^z + \delta J_{i,j}^z) \sigma_i^z \sigma_j^z, \quad (3.1)$$

where  $\delta h_i^z$  and  $\delta J_{i,j}^z$  are the respective errors in the parameters  $h_i^z$  and  $J_{i,j}^z$ . If qubit  $i$  is connected to qubit  $j$ , which is further connected to qubit  $k$ , as per the graph of the problem Hamiltonian, then the values of  $\delta h_i^z$  and  $\delta J_{i,j}^z$  depend on fields  $h_i^z$ ,  $h_j^z$ , and  $h_k^z$  and couplings  $J_{i,j}^z$  and  $J_{j,k}^z$ . Such factors can vastly affect the performance of the D-Wave systems for solving optimization problems [Ami15; Wil+20].

In 2020, the company inaugurated its new generation of quantum annealers, namely D-Wave Advantage (DWAAdv). The new system consists of more than 5000 qubits, and offers a new qubit topology, the Pegasus topology with a 15-way qubit connectivity. Compared to its predecessor, the Chimera topology on DW\_2000Q\_6 (DW2000Q), each qubit is connected to nine additional qubits in the Pegasus topology.

In this chapter, we study the performance of the DW2000Q and DWAAdv systems for solving various optimization problems. We start by describing how the D-Wave systems are employed to solve the chosen sets of problems. Subsequently, we discuss the results obtained from the two systems. In addition, we also compare the performances of the two systems for certain optimization problems.

## 3.1. Solving optimization problems using D-Wave systems

In this section, we first discuss how the optimization problems that need to be solved using the D-Wave quantum annealers are mapped on to the system. Next, we review some of the features and controls offered by the D-Wave systems that can vastly affect the performance of these systems for solving these problems.

In order to solve an optimization problem using the D-Wave systems, it needs to be specified through the linear and quadratic coefficients of a binary quadratic model (BQM) [D-W]. For the D-Wave QPU, the two processable types of BQMs are the Ising problem (Eq. (1.17)) and QUBO problem (Eq. (1.28)). A QUBO problem submitted to the D-Wave annealer is internally converted to an Ising problem such that  $h_i \in [-4, 4]$  and  $J_{i,j} \in [-1, 1]$  upon rescaling by a constant factor if the mapped values lie outside this range, with the help of the `auto_scaling` feature available in the system.

### 3.1.1. Embedding of the problem Hamiltonian

Solving an Ising problem using a D-Wave annealer requires the graph corresponding to the problem Hamiltonian to be mapped on to the working graph of the annealer. However, it is often the case that the problem graph is not a subgraph of the qubit topology of the device, and hence cannot be directly embedded on to the device. In order to solve such a problem, two or more physical qubits need to be grouped together using a ferromagnetic bond with a relatively large  $J_{i,j}$  coupling between them to avoid breaking of the thus formed logical qubits. The strength of this bond can be controlled using the chain strength parameter. It should however be noted that for large values of chain strength, the  $h_i$  and  $J_{i,j}$  values defining the problem are rescaled by a constant so that all values lie within the allowed range for the QPU. Any problem submitted to the D-Wave systems is heuristically mapped to the QPU topology by the D-Wave sampler, in a process known as minor-embedding.

It can nevertheless happen that the chain of physical qubits representing a logical qubit breaks during the annealing process such that in the end, not all the physical qubits corresponding to a logical qubit are in the same state. This is an undesirable effect. The final state of the logical qubit is determined by majority voting in such a case. It is rather straightforward to see that with a higher connectivity of the qubits, more problems can be directly embedded, i.e., without having to group the physical qubits. Figure 3.1 shows the Chimera and Pegasus qubit topologies available on DW2000Q and DWAdv systems, respectively. Not only does the DWAdv system contain approximately 3000 more qubits, each qubit in the Pegasus topology is connected to 15 other qubits, in contrast to a connectivity of 6 in the Chimera topology [Bun+14b; MF20]. Since the Pegasus topology is an extension of the Chimera topology, the latter can be natively embedded in the Pegasus topology. It is therefore interesting to see how the differences in these qubit topologies affect the performance of the two systems.

Although D-Wave's Ocean software offers tools to automatically generate an embedding for a given problem onto the qubit topology of the system, it need not yield the best

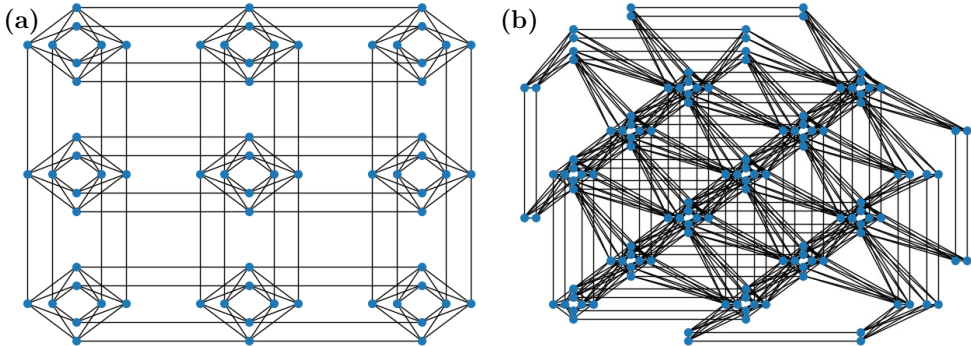


Figure 3.1.: Schematic of qubit topology (a) Chimera on DW2000Q system, and (b) Pegasus on DWAdv.

possible embedding in terms of the number of physical qubits used. However, optionally using the embedding feature available on these systems, it is possible to specify a chosen embedding for the problem, which can have a vast effect on the solution quality.

### 3.1.2. D-Wave controls

The D-Wave system software offers many parameters to control how the problem is run on the system and their choice can have a great impact on its performance. In this section, we discuss some of these features relevant to this work.

- **Annealing time:** It sets the duration for which the anneal is performed. The annealing time for the D-Wave systems is in the range of microseconds.
- **Number of reads:** This parameter sets the number of output samples required from the D-Wave system. Since the maximum duration for which a problem is allowed to run on the D-Wave quantum annealer is fixed, the maximum number of reads allowed also depends on the chosen annealing time.
- **Chain strength:** As described previously, the chain strength parameter controls the strength of the ferromagnetic coupling between the physical qubits comprising a logical qubit. This parameter also has a significant impact on the quality of the solution obtained from the D-Wave systems, and in order to obtain good results for a given problem, the optimal value of this parameter needs to be determined.
- **Annealing schedule:** This feature defines the time-dependent functions  $A(s)$  and  $B(s)$  that control the annealing scheme (see Eq. (1.18)). In the present work, we employ the default annealing scheme offered by the system.
- **Reverse annealing:** The standard quantum annealing schedule makes the system start in the ground state of the initial Hamiltonian by enforcing  $A(0) \ll B(0)$ .

However, with the help of the reverse annealing feature, it is possible to start the annealing algorithm at  $s = 1$  in a chosen classical state, anneal back to some reversal distance  $s_r$ , and then to resume the standard forward annealing from that point with or without the inclusion of a wait time at  $s_r$ .

## 3.2. Results

In section 1.4.2, we defined the sets of problems derived from the 2-SAT problems with unique satisfying assignments, as well as two classes of fully-connected problems that are suitable for benchmarking the D-Wave quantum annealers. We now proceed to discuss the results obtained for solving these problems using the D-Wave systems. Using the beta version of the Advantage topology, DWAdv\_beta, we benchmark the D-Wave systems using 2-SAT problems, the set of problems derived from them, as well as problems from two classes of fully-connected QUBO problems. The latter consist of random and regular class problems. Moreover, using these problem classes, we gauge the hardness of the fully-connected problems by studying the scaling behavior of their success probability using a newer generation of the Advantage systems, DWAdv5.1. More specifically, we study the correlation of this scaling behavior with the hardness estimates obtained using the Hamming distance distribution of the low-lying excited states with respect to the ground state, using the smaller problems from the sets. These scaling results are also compared to the corresponding values obtained for a set of newly constructed 2-SAT problems with up to 20 variables.

In this chapter, we use the success probability, defined as the ratio of the samples corresponding to the ground state energy to the total number of samples, as the performance metric.

### 3.2.1. Benchmarking the D-Wave systems

In this section, we assess the efficiency of the D-Wave systems for solving the set of 18-variable 2-SAT problems, the random-g problems, the multiple-copies problems, as well as instances of fully-connected random and regular problems. The goal here is to study different aspects of these systems using various kinds of problems.

#### 3.2.1.1. 18-variable 2-SAT problems

We start the assessment of the performance of the D-Wave annealers for solving the set of 18-variable 2-SAT problems consisting of 1000 problems. Using these problems, we wish to benchmark the two D-Wave systems, namely, the DW2000Q and the DWAdv, and compare their performance with each other. We choose the annealing time to be  $20 \mu s$ . In Fig. 3.2(a), we show a scatter plot of the success probabilities  $p_{DWAdv}$  obtained using DWAdv against the success probabilities  $p_{DW2000Q}$  obtained with DW2000Q. We observe that DWAdv performs better than DW2000Q for solving a majority of the problems, especially for the problems that have small success probabilities on the DW2000Q. On the other hand, the performance of the two systems is comparable when solving problems with

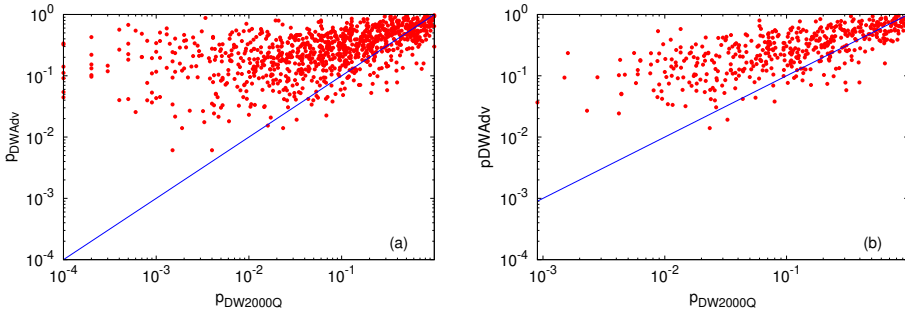


Figure 3.2.: Success probability obtained with DWAdv against the one obtained with DW2000Q for (a) all the problems in the set of 18-variable 2-SAT problems (1000 problems), and for (b) problems with a direct mapping on DW2000Q (476 problems).

relatively large success probabilities, concentrated in the upper right corner of Fig. 3.2(a). To delve deeper into this aspect, we compare how the problems are embedded on the two systems. While only 476 of the 1000 problems belonging to the set could find a direct mapping on the working graph of the DW2000Q system, 923 problems could be directly embedded on the DWAdv system. This can be attributed to a higher connectivity of the qubits in DWAdv. The effect of the embedding of the problem on the success probability can be more clearly seen from Fig. 3.2(b), which shows a scatter plot of the resulting success probabilities from the two systems for the problems having a direct embedding on DW2000Q. Although the success probability from DWAdv is still larger for a majority of the problems, it is not by as large an extent as in Fig. 3.2(a). This means that the largest improvement in the success probability on the DWAdv is obtained for the problems which could not find a direct embedding on DW2000Q. It can thus be concluded, that the higher connectivity of the qubits on DWAdv is advantageous for its performance, especially for the cases where the problem graphs could not be directly embedded on DW2000Q. This is an expected result since the chain of physical qubits representing a logical qubit is susceptible to breaking, thereby worsening the solution quality. Furthermore, for the problems with a direct embedding on both the D-Wave systems, we find DW2000Q to be performing slightly better for the problems with a relatively large success probability (points located on the upper right corner of Fig. 3.2(b)).

### 3.2.1.2. Random-g problems

Next, we move on to the results of the random-g problems. We choose two instances of 18-variable 2-SAT problems, such that for the standard choice of  $g_\alpha = 1$ , one of them has a large minimum energy gap between the ground state and the first excited state (found using Lanczos algorithm), while the other has a small gap. We refer to the former as the "first case" and to latter as the "second case". For both the problems, we create 100 new instances of 2-SAT problems, by randomly choosing the weights  $g_\alpha$  with which every

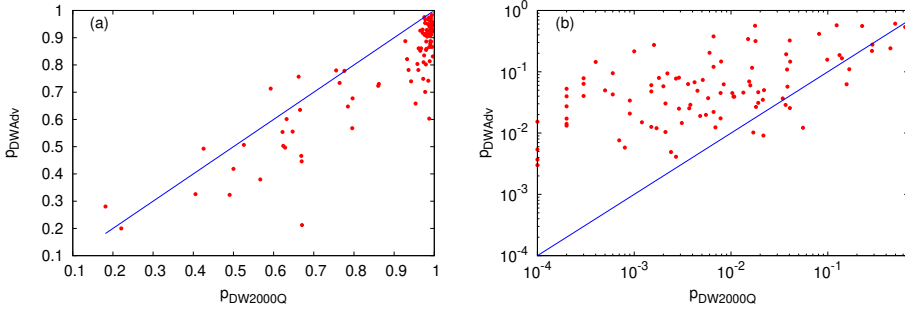


Figure 3.3.: Success probability obtained with DWAdv against the one obtained with DW2000Q for 100 random- $g$  problems created from an 18-variable 2-SAT problems with a minimum energy gap between the ground state and the first excited state (a) that is large (first case) and (b) that is small (second case).

clause constituting the 2-SAT problems contributes to the problem Hamiltonian, where  $g_\alpha \in [0.5, 1.5]$ . Employing both D-Wave systems for solving the two sets of random- $g$  problems allows for a comparison between their performances for hard and easy optimization problems. We choose the default annealing time of 20  $\mu$ s.

Firstly, we note from Fig. 3.3, that despite of randomly choosing the weights for each clause, a majority of the problem instances created have a similar hardness as the original problem with uniform  $g_\alpha = 1$ . We observe from Fig. 3.3(a) that for the first case, DW2000Q performs better for a majority of the instances compared to DWAdv, although the success probability for all these problem instances is larger than 0.1 on both the systems. We also find that all the problem instances corresponding to this case could be directly embedded in both DW2000Q and DWAdv. One of the possible reasons behind a decreased success probability on DWAdv could be an increase in the noise due to the presence of more number of unused couplers on DWAdv. On the other hand, for the second case shown in Fig. 3.3(b), the success probability is less than 0.1 for a majority of the instances on both the systems. In this case, DWAdv is found to be performing much better for a majority of the instances. We note that none of the instances of the second case could find a direct mapping on DW2000Q. Thus, the higher connectivity of qubits in DWAdv, and a small success probability of these problems on DW2000Q due to their inability to be directly embedded on the system result in a large enhancement in the success probability using DWAdv.

From the results of this section, we see that if there is a possibility to select the values of  $g$  using some variational ansatz so that the minimum energy gap between the ground state and the first excited state of the annealing Hamiltonian, or equivalently the success probability is maximized, this could vastly improve the performance of quantum annealing for solving these problems.

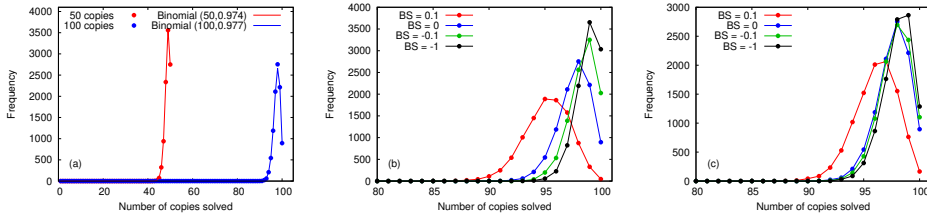


Figure 3.4.: Frequency distribution of the number of copies solved using DWAdv for the 12-variable multiple-copy problem and  $T_A = 20 \mu s$ , with (a) no connectivity between the neighboring copies, (b) neighboring copies connected through the least-connected variable, and (c) neighboring copies connected through the most-connected variable. Binomial( $N, p$ ) is the binomial distribution function used for fitting in (a), and  $BS$  in (b) and (c) represents different bond strengths between the connecting variables of neighboring copies.

### 3.2.1.3. Multiple-copies problems

Now, we focus on the second set of problems derived from the 2-SAT problems, i.e., the multiple-copies problems, in an attempt to benchmark the ability of DWAdv for solving problems with a large number of variables. In this section, we show the results for two instances of multiple-copies problem, the first comprising 50 and 100 copies of a 12-variable 2-SAT problem (comprising 600 and 1200 variables, respectively) with a relatively large minimum energy gap, and the second comprising 50 copies of an 18-variable 2-SAT problem (comprising 900 variables) with a relatively small minimum energy gap. The different copies of the problem can then be chosen to remain unconnected, or connected through a variable using parameter  $BS$  which characterizes the strength of this bond. We set the annealing time to  $20 \mu s$ , and the number of samples to 10000.

Since for the original 12-variable problem considered here, the minimum energy gap is large compared to that of the 18-variable problem, this problem is relatively easy to solve using quantum annealing. As shown in Fig. 3.4(a), for this case, it is possible to solve all of the 50 and 100 copies of the problem submitted to the D-Wave system. As the different copies of the problems are independent of one another, the frequency distribution of the number of simultaneous solutions obtained should ideally follow the binomial distribution  $\text{Binomial}(N, p, k) = {}^N C_k p^k (1-p)^{N-k}$ , where  $N$  is the number of copies,  ${}^N C_k = N!/(k!(N-k)!)$ ,  $p$  is the average success probability calculated as the ratio of the number of copies that could be solved to the total number of copies submitted, and  $k = 0, 1, \dots, N$ . The agreement between the results obtained from the DWAdv system and Binomial( $N, p$ ) shows that the qubits encoding the different copies can indeed work independently.

Next, Figs. 3.4(b) and (c) show the results for the frequency distribution of the number of copies solved for different values of bond strengths ( $BS$ ) with the least-connected variable and the most-connected variable as the connecting variable, respectively. In both these cases we consider 100 copies of the problem. For legibility, results corresponding to some values of the bond strengths have been omitted. For this case, we observe similar

trends in both figures. Adding a ferromagnetic bond between the copies of the problem increases the probability of all the 100 copies of the problems being solved simultaneously. We also observe that upon increasing the strength of the ferromagnetic bond till  $BS = -1$ , the peak of the corresponding curve becomes larger and shifts rightwards, i.e., the probability of a larger number of copies being solved increases with increasing the ferromagnetic bond strength. On increasing the bond strength further (not shown here), the curve shifts leftwards. One of the possible reasons for this observation could be the restriction on the allowed range for  $h$  and  $J$  values on the device, in accordance with which the problem parameters have to be rescaled when the bond strength decreases beyond -1.

On the other hand, adding an antiferromagnetic bond between the copies results in a decrease in the probability of solving a larger number of copies of the problem, and this probability decreases with increasing the strength of the bond. To provide an estimate, in the case where the bond between the multiple-copies is added through the least-connected variable, the curve corresponding to the antiferromagnetic bond with strength  $BS = 0.9$  peaks around 50.

In contrast to the 12-variable problem, the success probability for the original 18-variable problem is small. We embed 10, 20, 30, 40, and 50 unconnected copies of the problem on the system, and in no case it can solve all the copies simultaneously, as can be seen in Fig. 3.5(a). This is also found to be the case when adding ferromagnetic or anti-ferromagnetic bonds between the different copies of the problems. In contrast, the D-Wave Hybrid solver can find the ground state of the multi-copy problem, i.e., simultaneously solve all the copies of the problem. Additionally, with DWAdv it is possible to solve

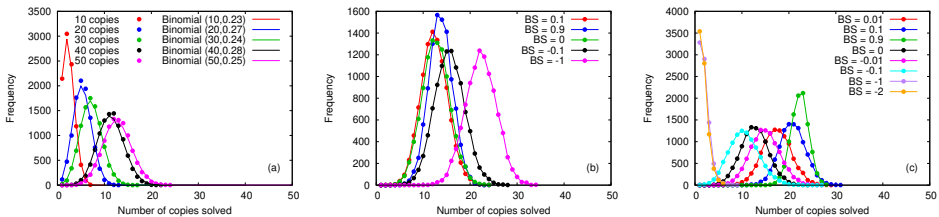


Figure 3.5.: Frequency distribution of the number of copies solved using DWAdv for the 18-variable multiple-copy problem and  $T_A = 20 \mu s$ , with (a) no connectivity between the neighboring copies, (b) neighboring copies connected through the last variable, and (c) neighboring copies connected through the most-connected variable (c).  $Binomial(N, p)$  is the binomial distribution function used for fitting in (a), and  $BS$  in (b) and (c) represents different bond strengths between the connecting variables of neighboring copies.

a larger number of copies simultaneously for certain values of bond strengths and the choice of the connecting variable. As for the 12-variable problems, upon choosing the least-connected variable from the problem graph as the connecting variable between the neighbouring copies, as shown in Fig. 3.5(b), the largest number of simultaneously solved copies of the problem increases with increasing strength of the ferromagnetic bond till  $BS = -1$ . However, the addition of an antiferromagnetic bond causes the curves to shift

leftwards.

On the other hand, we observe a more systematic rightward shift in the peaks for the number of simultaneously solved copies of the problem with the increasing strength of the anti-ferromagnetic couplings through the most-connected variable in the problem graph shown in Fig. 3.5(c). In this case, other than for  $BS = -0.01$ , a ferromagnetic bond leads to a decrease in the probability of simultaneously solving a large number of the copies. One of the possible reasons for this observation could be that for an antiferromagnetic bond, when the system fails to yield the ground state for one copy of the problem, it does not enforce other copies to remain unsolved, unlike a ferromagnetic bond. This makes these problems more difficult to be solved using a ferromagnetic bond, which enforces that either the system finds the ground state for all the copies simultaneously or for none of them. Since the original problem in this case is difficult to solve (has a smaller gap compared to most of the other problems in the set), in this case an antiferromagnetic bond is more beneficial for the success probability.

### 3.2.1.4. Fully-connected QUBO problems

We now move to the set of fully-connected problems, which we use to benchmark the performance of DWAdv for solving problems with large connectivity. Using two problem instances each for 50-variable random class problems, and 80- and 100-variable regular class problems, we study the effects of choosing different values for parameters like the annealing time and the chain strength on the success probability. For each problem instance, we run 10 trials for solving the fully-connected problem using the DWAdv system, for annealing times 20, 100, and 1000  $\mu s$  with the value of the chain strength varying from 1 to 10. The regular problem instances used to this end are created using the reshuffling of the indices (see section 1.4.2 for details on the construction of the problems).

At this point, it should be noted that the problem set with  $N = 50$  differs from the other two problem sets with  $N = 80$  and  $N = 100$ , and belong to a harder class of random problems. We discuss this in more detail in the next section. However, the effects of varying the annealing controls are noted to be similar for both these classes. Another point worth mentioning is that since the graph of different instances of the regular problems are essentially the same for a fixed  $N$ , they effectively correspond to just different embeddings of the problem.

Figure 3.6 shows the success rate of the fully-connected problems as a function of the chain strength for annealing times  $T_A = 20, 100, 1000 \mu s$ , averaged over ten runs on the system. As a first observation, we note a large variance in the values of the success rate, which is a consequence of the differences in the automatically generated embeddings of the problems by the D-Wave system during the different runs of the problem, as well as the noise and temperature effects present in the system. We find that as expected, the maximum success rate corresponds to the longest annealing time, however it is also observed that the value of the chain strength plays a decisive role in determining the performance. It can also be noted, that for a fixed annealing time, the maximum success rate for the problems corresponds to a larger value of chain strength as the size of the problem increases from  $N = 80$  to  $N = 100$ . One of the reasons for this observation could be the increasing need of longer chains of physical qubits in the system for embedding larger

### 3. Assessing the performance of the D-Wave systems

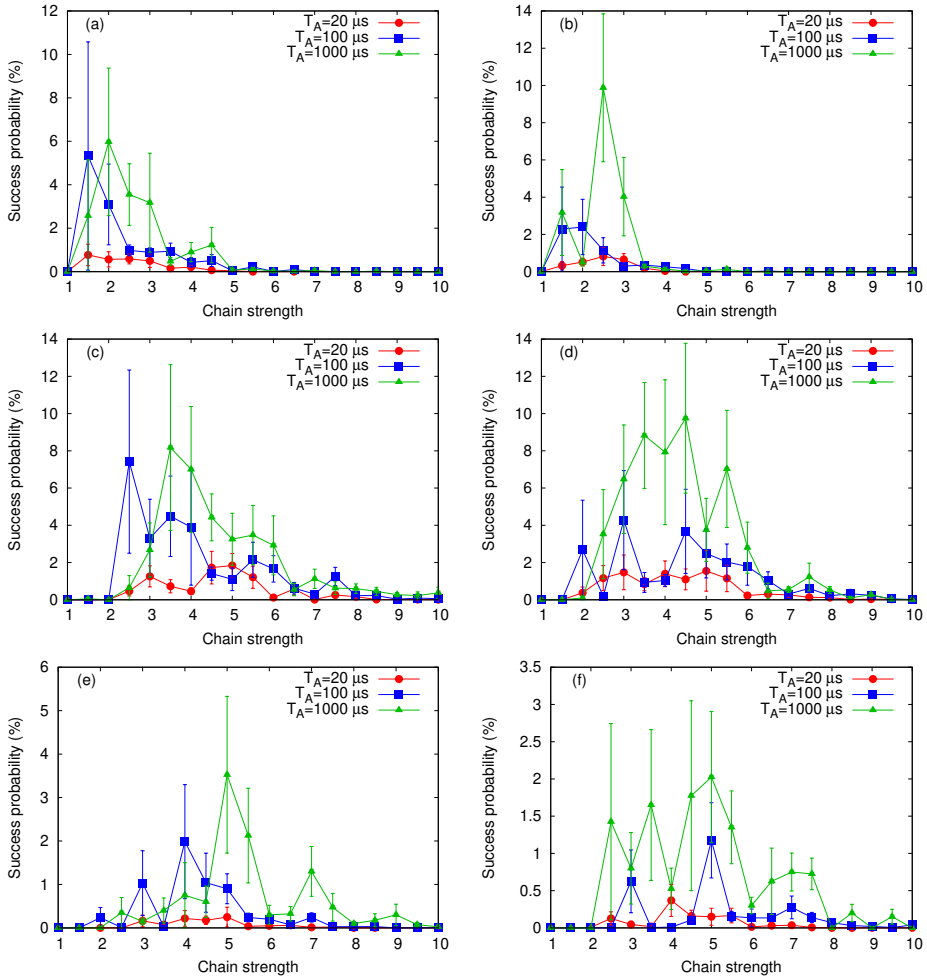


Figure 3.6.: Average success probability as a function of the chain strength for two instances of the fully-connected ((a), (b)) 50-variable random problem, ((c), (d)) 80-variable regular problem, and ((e), (f)) 100-variable regular problem averaged over 10 runs for annealing times 20, 100, and 1000  $\mu\text{s}$ .

problems and to avoid breaking of the chain during the annealing process larger values of chain strengths are required. Thus, the success probabilities can differ significantly when choosing different values of the annealing parameters.

### 3.2.2. Hardness of the QUBO problems

In this section, we examine the hardness of three classes of QUBO problems, namely, the 2-SAT problems, the fully-connected random problems, and the fully-connected regular problems, from the perspective of solving these problems by the D-Wave quantum annealer DWAdv. Specifically, we correlate the scaling performance of the D-Wave systems for solving the three classes of problems with the Hamming distance distributions of the low-lying excited states of representative 20-variable problems with respect to the ground state for the three classes [Meh+22b]. The regular problems used for this purpose are constructed using the spin-reversal transformation (see section 1.4.2).

#### 3.2.2.1. Hamming distance analysis

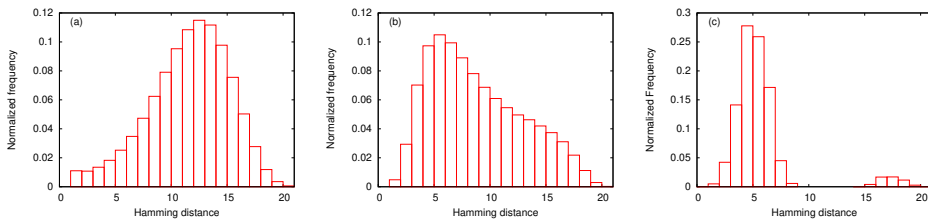


Figure 3.7.: Hamming distances of the low lying excited states from the ground state averaged over 100 instances of 20-variable (a) 2-SAT problems and (b) fully-connected random problems, and (c) a 20-variable fully-connected regular problem.

Figure 3.7(a) shows the normalized Hamming distance distribution of the degenerate first excited states, averaged over 100, 20-variable 2-SAT problems. All these states are four units of energy away from the ground state. The average Hamming distance of the first excited states of these problems is 11.07 with a standard deviation of 3.60, while the distribution peaks at a Hamming distance of 12.00. This implies, that using, say, simulated annealing, if one obtains one of these first excited states, one would need to do about 11 exact spin-flips, on average, to obtain the ground state. This suggests that such problems are hard to be solved using simulated annealing, which has shown to be the case in [Neu14a; Neu14b]. However, this hardness of the 2-SAT problem is related to its QUBO formulation. When represented in the implicative normal form, there exist classical algorithms by which the 2-SAT problems can be solved in polynomial time utilizing some special features of these problems. On the other hand, algorithms like simulated annealing and quantum annealing do not exploit such features for solving the 2-SAT problems.

The normalized Hamming distance distribution of the lowest 4000 excited states, averaged over 100 instances of 20-variable random problems, shown in Fig. 3.7(b), is very

different compared to that for the 2-SAT problems. These energy levels can be up to seventeen units of energy higher than the ground state. In this case, the average Hamming distance between the lowest excited energy states is 8.33, the standard deviation is 4.16, and the peak of the distribution lies at a Hamming distance of 5.00. This suggests that these problems should be relatively easy to solve using simulated annealing.

For the regular problems, all the problem instances corresponding to a given  $N$  have the same problem graph, and hence it suffices to look at the Hamming distance distribution of the lowest 4000 energy levels for one  $N = 20$  problem instance. This is shown in Fig. 3.7(c). In this case the energy of these levels can be up to twenty-four units of energy higher than the ground state. The distribution in this case is quite distinct compared to the previous two distributions, and the peak in this case lies at a Hamming distance of 4.00. We can therefore expect that out of the three classes of problems considered here, the regular problems are the easiest to solve using simulated annealing.

### 3.2.2.2. Scaling analysis

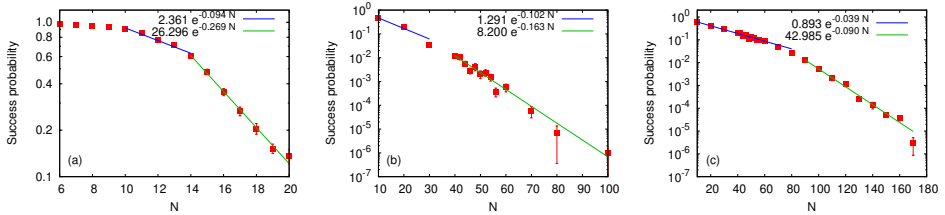


Figure 3.8.: Scaling of mean success probability as a function of problem size for (a) 2-SAT problems, (b) fully-connected random problems, and (c) fully-connected regular problems.

Next, we turn to the performance of the D-Wave Advantage\_system5.1 quantum annealer for solving these problems. For the 10 problem instances corresponding to each  $N$  for the random and regular problems, we run 10 annealing trials using the default annealing time  $T_A = 20 \mu\text{s}$ , and let the D-Wave’s ocean software automatically select the embedding and the chain strength values. In Fig. 3.8, we show the scaling of the average success probability of all the three classes of problems as a function of the problem size. As the first observation, we note that the average success probability decreases monotonically with an increase in the number of variables, for all the three classes. Since the size of the 2-SAT problems is limited to 20 variables during the creation of these problems, this is also the maximum size of the 2-SAT problems solved using DWAdv. On the other hand, random and regular problem classes consist of problems with up to 200 variables. For problems of the random class, the D-Wave annealer can find the solution for problem sizes up to  $N = 100$  only (Fig. 3.8(b)). It should be noted that none of the 90-variable random problems could be solved in even 20 trials of annealing performed in this case, and only in one trial did we find the solution to one of the 100-variable problem instances. In the case of the regular problems however, it is possible to go up to problems with  $N = 170$

before the problems become unsolvable by DWAdv. We may expect that choosing longer annealing times should lead to an increase in the success probability of these problems, hence making the larger problems solvable. Furthermore, as the size of the problems increases, embedding the QUBO problems onto the qubit topology of the D-Wave system becomes successively difficult. For example, for the 170-variable regular problems, 3964 physical qubits are required, and the software needs to make many attempts before it finally finds an embedding of the problem on to the QPU.

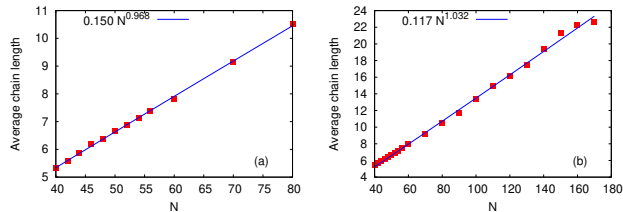


Figure 3.9.: Scaling of the chain length as a function of  $N$  for (a) random problems and (b) regular problems.

Focusing now on the scaling aspect, we note the average success probability to be exponentially decreasing as the problem size increases for all the three classes of problems. As even a simple brute-force search for the ground state scales with an exponent of 0.693 with  $N$ , i.e., exponentially as a linear power of  $N$ , we use exponential functions of the form  $a \exp(-bN)$  to fit to the average success probability. We then use the exponent thus obtained for large  $N$  as a measure of the hardness of the problem class. We find the scaling exponents to be the smallest for the regular problems and largest for the 2-SAT problems, which correlates well with the results from the Hamming distance analysis for the three problem classes. Furthermore, in all the three cases, we see a crossover in the scaling of the success probability as  $N$  increases. However, this crossover in the scaling is not observed for the average chain length scaling shown in Fig. 3.9, which continues to grow linearly as the size of the problem increases. Therefore, we regard the scaling for the larger  $N$  to lie closer to the true asymptotic scaling behavior of the success probability.

### 3.3. Summary

In this chapter, we employed the D-Wave systems DW2000Q and DWAdv for solving different optimization problems, made a comparison between the performances of these systems, and compared the hardness of three classes of QUBO problems using DWAdv with each other as well as their numerical estimates, i.e., the Hamming distance analysis for small problem instances from these classes.

We found that there were significant differences in the performances of the two D-Wave systems. It was observed that for the problems that had small success probabilities on DW2000Q, the DWAdv system performed better than the DW2000Q system for a majority of the problems, while for the easier problems the performances of the two systems were

comparable. Some of the reasons behind such observations are an increased connectivity of the qubits in the Pegasus topology on the DWAdv system, which results in shorter chains of physical qubits representing a logical qubit of the problem. Conducting a more detailed study to understand the other reasons for such observations can be one of the future tasks.

Next, using the multiple-copies of the 2-SAT problems that effectively consist of up to 1200 variables, we found that the frequency distribution of the number of simultaneously obtained copies of the problem follows the binomial distribution. This implies that the different parts of the DWAdv system embedding different copies of the problem are able to work independently of each other if the different copies of the problem are not connected. For the multiple-copies problem made up from the 12-variable 2-SAT problems it was possible to obtain the ground state of the problem, even when the different copies were unconnected. On the other hand, for the multiple-copies problem comprising of the hard 18-variable 2-SAT instance, the quantum annealer could not find the solution to the combined problem, irrespective of whether or not different copies are connected. However, for certain values of bonds between the different copies, the number of copies that could be simultaneously solved could increase.

Our results also indicated that the probability of finding the solution to a given problem depends strongly on the values of the parameters like the annealing time and relative chain strength. At this point, it is worth mentioning that despite of the annealing times being sufficiently long, the evolution of the state of the system is not guaranteed to be adiabatic, as will be discussed in detail in chapter 6.

Lastly, using two classes of fully-connected QUBO problems and a set of 2-SAT problems, the scaling complexity of these problems obtained using the D-Wave annealer was found to be well correlated with the estimates of their hardness from the Hamming distance distribution of the low-lying excited states with respect to the ground state of the smaller problem instances of these classes.

## 4. Fair sampling

In the previous chapter, we studied the performance of the D-Wave systems for solving 2-SAT problems, and other problems derived from them. We also utilized these systems to solve fully-connected QUBO problems, with the focus on the success probability as a measure of the effectiveness of the approach for solving these problems. Another important aspect, relevant in case of problems with more than one possible solution, is that of sampling of all the solutions of a given optimization problem. More specifically, the focus here is to assess the ability of quantum annealing to yield all the degenerate ground states of the problem Hamiltonian in a fair manner, i.e., with comparable sampling probabilities.

In this chapter, we explore this aspect of quantum annealing, using both simulations and the D-Wave quantum annealers. Furthermore, we make use of the reverse annealing feature available in the D-Wave systems to gauge its efficacy in fairly sampling all the solutions of the given problems. The main idea of the reverse annealing protocol is to start in one of the low-lying eigenstates of the classical Hamiltonian at  $s = 1$ , and anneal backwards till a point  $s_r$ , referred to as the reversal distance, by increasing the strength of the transverse field. After an optional waiting time  $T_W$  at  $s_r$ , the system is again swept towards  $s = 1$ , in the hope of finding a state with lower energy than the state in which the protocol started, or to sample more number of ground states if starting from one of the ground states [PVA11; Cha17; Kim+18; OA18; VK19; Mar+19; ONL18; Yam+19]. In order to compare the performance of a real quantum annealer with an ideal implementation of the reverse annealing algorithm, we also perform the simulations of the same. For this analysis, we use the new set of 2-SAT problems with four satisfying assignments (see section 1.4.1.1).

In the following sections, we discuss the sampling results using the standard forward quantum annealing as well as reverse annealing. Using the sets of 2-SAT problems with ground state degeneracy of four, we use both simulations and the D-Wave quantum annealers to study the fairness of quantum annealing in sampling all the ground states. We first discuss the results obtained using the standard forward quantum annealing protocol and then move to discussing the scope of reverse annealing in fairly sampling the ground states.

### 4.1. Forward annealing

The standard quantum annealing protocol, as also implemented by a D-Wave quantum annealer, starts from the uniform superposition state which slowly tends towards a classical state while, ideally, staying in the ground state of the instantaneous Hamiltonian at all times. This process is implemented by choosing a scheme with a decreasing (increasing)  $A(s)$  ( $B(s)$ ) in the Hamiltonian Eq. (1.18). In this section, we study the efficiency of the

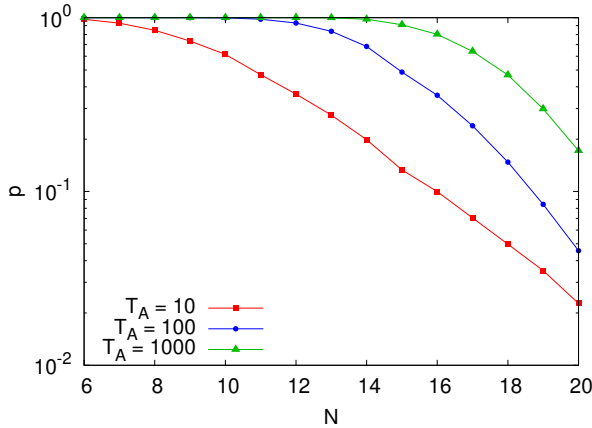


Figure 4.1.: Average total success probability of the 2-SAT problem sets with ground state degeneracy of four and  $6 \leq N \leq 20$  obtained from the numerical simulation for  $T_A = 10, 100, 1000$ .

standard quantum annealing Hamiltonian in fairly sampling the degenerate ground states of the problem Hamiltonian using simulations and the D-Wave’s Advantage\_system5.1 (DWAdv).

#### 4.1.1. Simulation results

We start by focusing on the numerically obtained results. We use annealing times  $T_A = 10, 100$ , and  $1000$  for finding the probability of obtaining the four degenerate ground states of the problem Hamiltonian for problem sets with  $6 \leq N \leq 20$ , where each set contains 100 different problems.

As the first observation, we note from Fig. 4.1 that shows the average success probability of the 100 problems of each set as a function of the problem size for a given annealing time that the average total success probability, which is the average of the sum of the sampling probabilities of the four degenerate ground states of the problem Hamiltonian, decreases as the size of the problem increases. This can be explained as follows. In Section 6.2.1, we will see that the minimum energy gap between the ground state and the first excited state of the annealing Hamiltonian corresponding to the 2-SAT problems with a unique satisfying assignment closes exponentially with increasing size of the problems. We expect that the minimum energy gaps in the case of problem Hamiltonians with degenerate ground states also shows a similar scaling behavior. The Landau-Zener theorem then suggests that the success probability should also decrease with an increasing size of the system, if the annealing time is kept fixed. Furthermore, while the average total success probability decreases rapidly for  $T_A = 10$  as the size of the problems increases, for the given sets of problems, the average success probability corresponding to  $T_A = 1000$  stays reasonably large even for the problem set with  $N = 20$ .

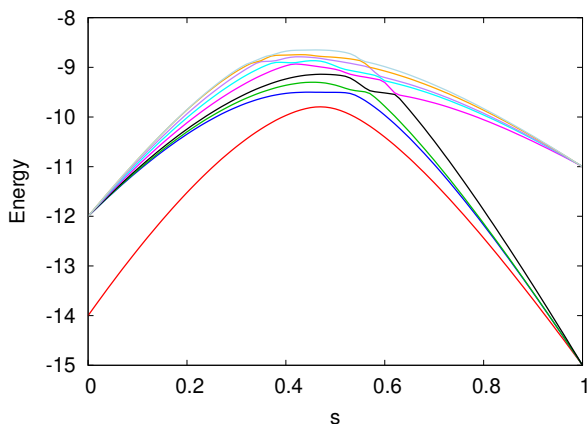


Figure 4.2.: Energy spectrum of a 14-variable problem Hamiltonian labelled as problem "230" with four degenerate ground states.

For a vast majority of the cases where the chosen annealing time is sufficient for even an almost-adiabatic evolution of the state of the system (which mostly holds for  $T_A = 100$  and  $1000$ ), we find that the sampling probabilities of the four ground states are approximately equal, i.e., the sampling is fair. An example of such a 14-variable problem is given in Tab. 4.1 labelled as problem "1". While this observation also holds for the annealing time  $T_A = 10$  for the smaller sets of the problems studied, as the size of the problems increases the total success probability of the problems belonging to these sets decreases. From what will become more apparent in Chapter 5, the annealing time  $T_A = 10$  is not long enough to ensure an adiabatic evolution of the state of the system. Furthermore, in Fig. 4.2, we show the energy spectrum of a 14-variable problem belonging to this set. As also observed for many other problems from the set of problems being studied (data not shown), we see in Fig. 4.2 that the anticrossings between one energy level and the next are aligned in an increasing order of the annealing parameter  $s$ , in a cascade like manner. These two factors combined can lead to a large deviation of the state of the system from the instantaneous ground state, resulting in a small success probability for a majority of the problems for  $T_A = 10$ . However, it can happen that owing to certain non-adiabatic mechanisms the total success probability of finding the ground state of the problem Hamiltonian is large despite of the small annealing time chosen (see Section 5.1.3), but the sampling probability of the four degenerate ground states might remain unequal.

For a few other cases, however, even with the long annealing times  $T_A = 100$  and  $1000$  where the evolution of the state of the system remains almost adiabatic, we observe unequal sampling probabilities of the four ground states. An example of such a 14-variable problem is the problem labelled as problem "3" given in Tab. 4.1. For an annealing time  $T_A = 1000$ , the sampling probabilities of the four ground states of this 2-SAT problem are obtained to be 0.139, 0.361, 0.361, and 0.139.

In a yet more extreme case of unfair sampling we observe a few problems for which

Table 4.1.: Three instances of 2-SAT problems: Problem "1" with almost fair sampling, Problem "3" with unequal sampling probabilities of the four ground states, and Problem "230" with zero sampling probability of one of the ground states. Each row of the table represents a clause of the corresponding 2-SAT problem consisting of two literals, where each literal can be a binary variable  $x_i$  or its negation  $\overline{x}_i$ .

Problem:"1"		Problem:"3"		Problem:"230"	
$\overline{x}_{13}$	$x_{14}$	$\overline{x}_8$	$x_{10}$	$\overline{x}_{10}$	$\overline{x}_{13}$
$\overline{x}_{11}$	$x_{13}$	$\overline{x}_7$	$x_{14}$	$\overline{x}_8$	$x_{13}$
$\overline{x}_{10}$	$x_{12}$	$\overline{x}_6$	$\overline{x}_{11}$	$\overline{x}_7$	$\overline{x}_{14}$
$\overline{x}_6$	$\overline{x}_8$	$\overline{x}_4$	$x_{11}$	$\overline{x}_6$	$\overline{x}_{14}$
$\overline{x}_6$	$x_{11}$	$\overline{x}_3$	$\overline{x}_5$	$\overline{x}_5$	$\overline{x}_{12}$
$\overline{x}_4$	$\overline{x}_6$	$\overline{x}_2$	$x_{14}$	$\overline{x}_4$	$\overline{x}_8$
$\overline{x}_4$	$x_{10}$	$\overline{x}_1$	$\overline{x}_{11}$	$\overline{x}_2$	$x_9$
$\overline{x}_2$	$x_{14}$	$\overline{x}_1$	$x_4$	$\overline{x}_2$	$x_{12}$
$\overline{x}_1$	$x_5$	$x_2$	$\overline{x}_{12}$	$\overline{x}_1$	$\overline{x}_{11}$
$x_1$	$x_9$	$x_3$	$x_6$	$x_1$	$\overline{x}_3$
$x_3$	$\overline{x}_5$	$x_4$	$\overline{x}_{14}$	$x_2$	$x_8$
$x_4$	$\overline{x}_{14}$	$x_6$	$\overline{x}_{11}$	$x_3$	$\overline{x}_{12}$
$x_4$	$\overline{x}_9$	$x_7$	$\overline{x}_{10}$	$x_4$	$\overline{x}_9$
$x_6$	$\overline{x}_{10}$	$x_8$	$\overline{x}_{13}$	$x_6$	$x_{11}$
$x_7$	$x_{13}$	$x_8$	$\overline{x}_9$	$x_{12}$	$\overline{x}_{13}$

Table 4.2.: Sampling probabilities of the degenerate ground states  $|\psi_0^i\rangle$ ,  $i = 1, 2, 3, 4$ , of the problem "230", corresponding to different annealing times  $T_A$ , for the standard quantum annealing Hamiltonian.

State	$T_A = 10$	$T_A = 100$	$T_A = 1000$
$ \psi_0^1\rangle$	0.1233	0.4427	0.4986
$ \psi_0^2\rangle$	0.0742	0.2605	0.2507
$ \psi_0^3\rangle$	0.0648	0.0131	$9.56 \times 10^{-10}$
$ \psi_0^4\rangle$	0.0589	0.2214	0.2506
Total	0.3212	0.9377	0.9909

even with a long annealing time like  $T_A = 1000$ , the sampling probability of one of the four ground states is totally suppressed. One such problem instance has been given in Tab. 4.1 labelled as problem "230". In this case we find the sampling probabilities of the degenerate ground states to be 0.499, 0.251,  $9.56 \times 10^{-10}$ , and 0.251 for  $T_A = 1000$ . The energy spectrum for problem "230" is shown in Fig. 4.2. The sampling probabilities of the four ground states for other annealing times are shown in Tab. 4.2.

### 4.1.2. D-Wave results

Next, we inspect the performance of DWAdv for fairly sampling the ground states of the degenerate problem Hamiltonians. We choose an annealing time of  $4 \mu s$ , and as for the simulations, find the sampling probabilities of all the ground states of the degenerate problem sets at hand. In Fig. 4.3, we show the average total success probability of the problem sets corresponding to  $10 \leq N \leq 20$  for the chosen annealing time. It is evident from the figure that the average success probability is comparable to the simulation results with annealing time  $T_A = 1000$ , despite of choosing a much longer annealing time on DWAdv ( $T_A = 1000$  in simulations is approximately equivalent to 50 ns in the D-Wave energy scale). This is indicative of the presence of noise and temperature effects in the D-Wave system.

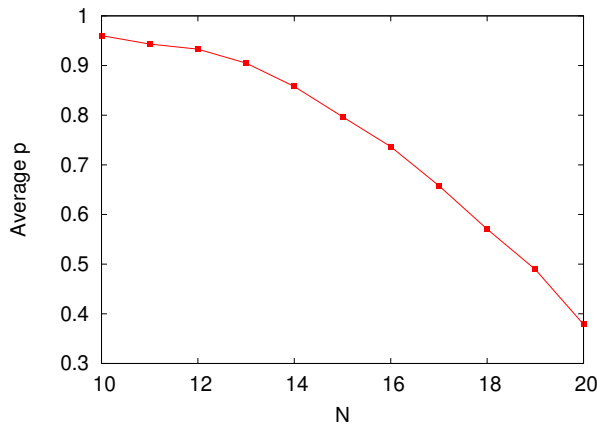


Figure 4.3.: Average total success probability of the 2-SAT problem sets with ground state degeneracy of four with  $10 \leq N \leq 20$  obtained from DWAdv for  $T_A = 4 \mu s$ .

In this case we find a more fair sampling of the four ground states compared to the numerical results, even for cases like problem "3" and "230" for which the simulation with  $T_A = 1000$  resulted in unequal sampling probabilities of the ground states. For the 14-variable problem "230", which had close to zero sampling probability of the third ground state in case of simulation with  $T_A = 1000$ , DWAdv results in sampling probabilities of 0.2470, 0.3124, 0.1552, and 0.2765, respectively. It should also be noted that the annealing time  $T_A = 4 \mu s$  is much longer compared to the simulation time  $T_A = 1000$ .

### 4.1.3. Perturbation theory

The observations noted from the simulation results regarding the sampling probabilities, at least in the long annealing time limit, can be understood using perturbation theory. More specifically, for sufficiently long annealing times, the sampling behavior of the ideal quantum annealing algorithm can be explained on the basis of the instantaneous ground state of the Hamiltonian in the vicinity of  $s = 1$ , which can be approximated using perturbation theory. In this section, we consider three examples of 14-variable 2-SAT problems with four satisfying assignments, which have been given in Tab. 4.1 and have different sampling probabilities, and use perturbation theory to understand the sampling results [MNK09; Kön+19].

In the limit  $s \approx 1$ , the instantaneous Hamiltonian can be approximated as the problem Hamiltonian  $H_P$  with a small perturbation  $V$  (the initial Hamiltonian) added to it. When the annealing time is sufficiently long for the state of the system to follow the ground state of the instantaneous Hamiltonian, the ground state of this perturbed Hamiltonian around  $s \approx 1$  can be used to obtain an estimate for the sampling probabilities of the ground states of the problem Hamiltonian. However, since the degenerate subspace of such Hamiltonians is essentially equivalent to the identity operator in any energy basis (after factoring out the common energy eigenvalue), the choice for the basis vectors for the degenerate subspace of the Hamiltonian becomes arbitrary. Employing perturbation theory for obtaining an estimate for the ground state of such Hamiltonians around  $s = 1$  requires choosing a basis suitable for obtaining the first- and second-order corrections in energy and the wavevector. To keep the degenerate perturbation theory going, this basis should be the basis that diagonalizes the initial Hamiltonian in the degenerate subspace. As the perturbation matrix we have  $V_{i,j} = \langle \psi_0^i | H_I | \psi_0^j \rangle$ , where  $H_I$  is the initial Hamiltonian and  $|\psi_0^i\rangle$  for  $i = 1, 2, 3, 4$  are the four degenerate ground states of the problem Hamiltonian in the computational basis. If the lowest energy eigenvalue of the perturbation matrix  $V$  is non-degenerate, the addition of the perturbation lifts the degeneracy in the ground energy of the problem Hamiltonian. This can be shown to be the case using Appendix B. The sampling probabilities of the four ground states of the problem Hamiltonian are then given by  $|a_i|^2$ , where  $|\nu_1\rangle = \sum_{i=1}^4 a_i |\psi_0^i\rangle$  is the eigenvector of the perturbation matrix with the smallest eigenvalue and the index  $i$  corresponds to the different ground states of the problem Hamiltonian.

We start with problem labelled as problem "1", observed to have an almost fair sampling of the four ground states, i.e., the ground states sampling probabilities are obtained to be 0.250, 0.249, 0.251, and 0.250 from the numerical simulations for  $T_A = 1000$ . The four ground states for problem "1" are  $|\psi_0^1\rangle = |10101010000000\rangle$ ,  $|\psi_0^2\rangle = |10101011000000\rangle$ ,  $|\psi_0^3\rangle = |10101010000100\rangle$ , and  $|\psi_0^4\rangle = |10101011000100\rangle$ . The first-order perturbation matrix for this problem is thus given as

$$V = \begin{pmatrix} 0 & -1 & -1 & 0 \\ -1 & 0 & 0 & -1 \\ -1 & 0 & 0 & -1 \\ 0 & -1 & -1 & 0 \end{pmatrix}. \quad (4.1)$$

The ground state of this perturbation matrix is  $|\nu_1\rangle = (0.5, 0.5, 0.5, 0.5)$ . Thus, for this

case we can expect uniform sampling probabilities of the four ground states in the long annealing time limit according to the first-order perturbation theory.

As the second example, we choose the 14-variable problem labelled as problem "3" and given in Tab. 4.1, for which the sampling probabilities of the four ground states are 0.139, 0.361, 0.361, and 0.139 for  $T_A = 1000$ . The four ground states of this problem Hamiltonian are  $|\psi_0^1\rangle = |00100000000000\rangle$ ,  $|\psi_0^2\rangle = |00000100000000\rangle$ ,  $|\psi_0^3\rangle = |00100100000000\rangle$ , and  $|\psi_0^4\rangle = |00001100000000\rangle$ . The first-order perturbation matrix in this case is

$$V = \begin{pmatrix} 0 & 0 & -1 & 0 \\ 0 & 0 & -1 & -1 \\ -1 & -1 & 0 & 0 \\ 0 & -1 & 0 & 0 \end{pmatrix}, \quad (4.2)$$

and the lowest eigenvector of  $V$  is given as  $|\nu_1\rangle = (0.372, 0.601, 0.601, 0.372)$ . Thus, the probability to obtain ground state  $|\psi_0^i\rangle$ , where  $i = 1, 2, 3, 4$  given by  $|a_i|^2$ , are obtained to be 0.138, 0.362, 0.362, and 0.138, respectively. These values are in close agreement with the sampling probabilities obtained numerically for this problem with annealing time  $T_A = 1000$ .

Lastly, we look at the more extreme case of unfair sampling, i.e., we consider problem "230" where the sampling probability of the third ground state was found to be totally suppressed even for  $T_A = 1000$ . The four ground states of this problem Hamiltonian are  $|\psi_0^1\rangle = |11110100100101\rangle$ ,  $|\psi_0^2\rangle = |11110100110101\rangle$ ,  $|\psi_0^3\rangle = |10100101000111\rangle$ , and  $|\psi_0^4\rangle = |11110100100111\rangle$ . The perturbation matrix for this problem is thus

$$V = \begin{pmatrix} 0 & -1 & 0 & -1 \\ -1 & 0 & 0 & 0 \\ 0 & 0 & 0 & 0 \\ -1 & 0 & 0 & 0 \end{pmatrix}. \quad (4.3)$$

From Eq. (4.3), we can clearly see that the third ground state of the Hamiltonian is completely decoupled from the rest of the three ground states. The eigenvector of the first-order perturbation matrix with the smallest eigenvalue is  $|\nu_1\rangle = 1/2(\sqrt{2}, 1, 0, 1)$ . This implies that the sampling probability of the ground state  $|\psi_0^3\rangle$  can be expected to be zero, which was indeed the result of the simulations corresponding to  $T_A = 1000$  (see Tab. 4.2). Such a suppression of the ground state is not observed for  $T_A = 10$ , where the sampling probabilities of the degenerate ground states are comparable and the total success probability is much smaller. This is, as explained previously, due to the fact that the annealing time  $T_A = 10$  is too short for preventing the state of the system from leaking out of the ground-state subspace following the cascade of anticrossings. Furthermore, in the presence of noise and temperature effects, as in the case of the D-Wave annealers, the evolution of the state of the system need not be adiabatic, in spite of long annealing times, and thus higher energy levels can still be involved. These energy levels might then have a finite overlap also with the ground state  $|\psi_0^3\rangle$  which is expected to have a suppressed sampling probability according to the ground state of the perturbed Hamiltonian. This is indeed observed in the sampling behavior from DWAdv, where the sampling probabilities of the four ground states are almost fair for problem "230" and other such problems in the

set. Thus, put differently, beyond the adiabatic limit, one is not guaranteed to witness a suppression of any of the ground states that one would expect based on perturbation theory.

## 4.2. Reverse annealing

Having discussed the performance of the standard forward quantum annealing protocol in sampling the ground states of degenerate problem Hamiltonians, we now turn to analyzing the same using reverse annealing. The reverse annealing feature in the D-Wave annealers is accompanied by many annealing controls. In order to compare the sampling performances of the D-Wave systems and the simulations, we implement similar choices of controls in our simulations. These include the forward and reverse annealing times, the reversal distance, inclusion of the waiting time, and the choice of the initial state. In the following, we discuss the impact of these choices one by one, starting first with the simulation results, and then moving to those obtained using DWAdv. For this analysis we use the 14-variable problem "230" discussed in the previous section, whose third ground state is theoretically expected to have a sampling probability of zero in the long annealing time limit.

### 4.2.1. Simulation results

In this section, we focus on the simulation results for the sampling of the four degenerate ground states of the problem Hamiltonian for different choices of the annealing controls. We choose one of the ground states of the problem Hamiltonian as the initial state of the algorithm. From the view point of obtaining a better solution, it is not useful to start the reverse annealing algorithm in the ground state of the problem Hamiltonian, as the protocol cannot yield any lower classical state in the end. However, this is a valid choice for studying the sampling behavior of the ground states.

#### Varying the annealing time

We start with studying the effects of various annealing times on the sampling probabilities of the four ground states obtained using the simulations. For this, we choose equal reverse and forward annealing times, no waiting time, a reversal distance  $s_r = 0.7$ , and initialize the system in the first ground state. Similar in spirit to our discussion above, choosing large values like  $s_r = 0.7$  for the reversal distances is also not a good choice for reverse annealing to yield a better solution, as starting from one of the low-lying excited states, the reverse annealing protocol can only be useful if the system is allowed to reach a reversal distance comparable to the  $s$  value corresponding to the relevant anticrossing(s) so that lower energy levels become accessible. However, from the sampling point of view, such a choice can be considered as a valid choice.

Table 4.3 shows the resulting probabilities of the four ground states of the considered degenerate problem Hamiltonian corresponding to different annealing times from which a couple of observations follow. We note that the total success probability, which is simply the sum of the sampling probabilities of the four ground states, is close to 1 for all

Table 4.3.: Sampling probabilities of the degenerate ground states  $|\psi_0^i\rangle$ ,  $i = 1, 2, 3, 4$ , of the problem "230", corresponding to different annealing times  $T_A$ , where the reverse annealing time is chosen to be same as the forward annealing time. The initial state is chosen to be  $|\psi_0^1\rangle$ , the reversal distance is  $s_r = 0.7$ , and no waiting times are added.

State	$T_A = 10$	$T_A = 50$	$T_A = 90$	$T_A = 100$	$T_A = 500$	$T_A = 1000$
$ \psi_0^1\rangle$	0.1891	0.4348	0.9011	0.0296	0.7374	0.2614
$ \psi_0^2\rangle$	0.4053	0.2822	0.0495	0.4051	0.1313	0.3693
$ \psi_0^3\rangle$	$1.47 \times 10^{-4}$	$2.73 \times 10^{-5}$	$2.87 \times 10^{-6}$	$4.92 \times 10^{-6}$	$2.83 \times 10^{-7}$	$3.21 \times 10^{-8}$
$ \psi_0^4\rangle$	0.4031	0.2829	0.0493	0.4852	0.1313	0.3692
Total	0.9976	0.9990	1.000	1.0000	1.0000	1.000

the annealing times, and increases as the annealing time increases. This is an expected behavior, as according to the Landau-Zener theory, upon increasing the annealing time, the probability of the amplitude to get transferred from the ground state (in this case the ground subspace) to the higher excited level (in this case the fourth excited state) should decrease. This results in an increase in the total success probability.

Next, we observe that as the annealing time increases from  $T_A = 10$  to  $T_A = 1000$ , the sampling probability of the first ground state, i.e., the state from which the algorithm starts, fluctuates, and gets distributed over the second and fourth ground state of the problem Hamiltonian. This can be understood as follows. In terms of the new basis chosen for the degenerate subspace of the problem Hamiltonian, as described in section 4.1.3, the first ground state is given as

$$|\psi_0^1\rangle = \frac{1}{\sqrt{2}} |\nu_1\rangle - \frac{1}{\sqrt{2}} |\nu_4\rangle, \quad (4.4)$$

where  $|\nu_1\rangle = 1/2(\sqrt{2}, 1, 0, 1)$  and  $|\nu_4\rangle = 1/2(-\sqrt{2}, 1, 0, 1)$  are the eigenvectors corresponding to the smallest and the largest eigenvalues of the perturbation matrix, respectively. Let us assume that at the end of the annealing process, the final state of the system, restricted to the subspace of the ground state is

$$|\psi\rangle = R_1 e^{i\phi_1} |\nu_1\rangle + R_2 e^{i\phi_2} |\nu_2\rangle + R_3 e^{i\phi_3} |\nu_3\rangle + R_4 e^{i\phi_4} |\nu_4\rangle, \quad (4.5)$$

where  $R_i$  is the real part of the complex amplitude of the final state,  $\phi_i$  is the acquired phase, and  $i = 1, 2, 3, 4$ . However, taking into account the overlap of the system state during the annealing process with the lowest four instantaneous energy states of the Hamiltonian, shown in Fig. 4.4, we observe that in terms of the instantaneous energy eigenbasis, the amplitudes present in the first and the fourth states remain nearly constant during the annealing process. This suggests that the chosen annealing time is sufficiently long for a nearly adiabatic evolution. Thus, we can approximate the final state at the end of the annealing protocol as

$$|\psi\rangle = \frac{1}{\sqrt{2}} e^{i\phi_1} |\nu_1\rangle + \frac{1}{\sqrt{2}} e^{i\phi_4} |\nu_4\rangle. \quad (4.6)$$

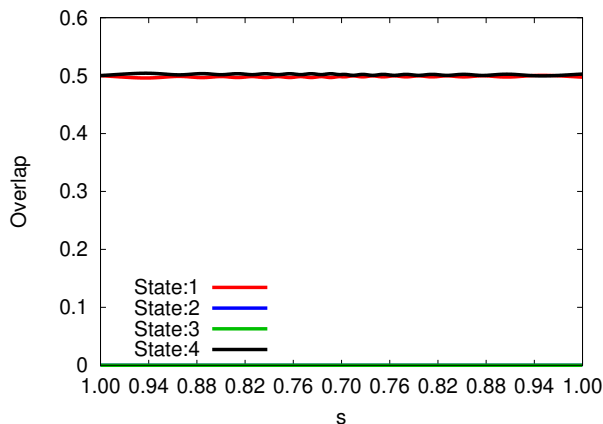


Figure 4.4.: Instantaneous overlap of the state of the system with the four lowest energy eigenstates of the Hamiltonian for  $s_r = 0.7$  and  $T_A = 100$  during the reverse annealing phase ( $s$  changes from 1 to  $s_r$ ) followed by the annealing phase ( $s$  changes from  $s_r$  to 1).

Since the four eigenvectors  $|\nu_i\rangle$  are mutually orthogonal, the individually acquired phases  $\phi_i$  are physically irrelevant if the sampling probabilities are measured in the eigenbasis of the perturbation Hamiltonian. However, as the computational basis is generally chosen to be the measurement basis, and the ground states  $|\psi_0^i\rangle$  of the problem Hamiltonian have finite overlaps with the  $|\nu_i\rangle$ 's, we have

$$\langle \psi_0^i | \psi \rangle = R_1 e^{i\phi_1} \langle \psi_0^i | \nu_1 \rangle + R_4 e^{i\phi_4} \langle \psi_0^i | \nu_4 \rangle. \quad (4.7)$$

Thus, when the sampling probabilities are measured in the computational basis, i.e.,  $|\psi_0^i\rangle$ , the individual phases  $\phi_i$  lead to interference, and in turn to fluctuations in the sampling probabilities of the ground states of the problem Hamiltonian. As the third ground state of the problem Hamiltonian does not have any overlap with  $|\nu_1\rangle$  or  $|\nu_4\rangle$ , the sampling probability of this state remains fairly low at the end of the anneal, and decreases systematically with increasing the annealing time.

### Varying the reversal distance

We now study the sampling probabilities of the ground states of the problem Hamiltonian as a function of different reversal distances. We fix the annealing time to  $T_A = 1000$ , do not add any waiting times, start with the first ground state, and vary the reversal distance such that  $0.4 \leq s_r \leq 0.8$ . The resulting sampling probabilities of the four ground states are shown in Tab. 4.4. We observe that the total success probability, which is the sum of the sampling probabilities of the four ground states, decreases as the value of the reversal distance is decreased, except for  $s_r = 0.4$ . This decrease can be explained on the basis of the energy spectrum of this problem Hamiltonian, given in Fig. 4.2. For this problem, the

Table 4.4.: Sampling probabilities of the degenerate ground states  $|\psi_0^i\rangle$ ,  $i = 1, 2, 3, 4$ , of the problem "230", corresponding to different reversal distances  $s_r$ , with annealing time  $T_A = 1000$ ,  $|\psi_0^1\rangle$  as the initial state, and without any waiting time.

State	$s_r = 0.4$	$s_r = 0.5$	$s_r = 0.6$	$s_r = 0.7$	$s_r = 0.8$
$ \psi_0^1\rangle$	0.0703	0.4507	0.8310	0.2614	0.6147
$ \psi_0^2\rangle$	0.2874	0.0513	0.0566	0.3693	0.1926
$ \psi_0^3\rangle$	0.0012	0.0010	$1.84 \times 10^{-6}$	$3.21 \times 10^{-8}$	$8.66 \times 10^{-10}$
$ \psi_0^4\rangle$	0.2739	0.0789	0.0579	0.3692	0.1926
Total	0.6396	0.5820	0.9454	1.0000	1.0000

anticrossing between the instantaneous fourth excited state and fifth excited state occurs around  $s_r = 0.62$ , while that between the instantaneous ground state and the first excited state occurs around  $s = 0.42$ . Lowering the reversal distance to these values promotes the transfer of the amplitude present within the ground subspace to leak out of the ground subspace. This results in an overall decrease in the total success probability.

From Tab. 4.4, we also see that the sampling probability of the first ground state of the problem Hamiltonian is not 1, while those of the second and the fourth ground states are non-zero. This can once again be explained on the basis of interference between the complex amplitudes when the instantaneous energy eigenbasis is chosen to express the state of the system, since  $|\nu_i\rangle$  have finite overlaps with  $|\psi_0^i\rangle$  for  $i = 1, 2, 3, 4$ . To understand the underlying dynamics in more detail, we look at the instantaneous overlaps of the state of the system with the ten lowest energy eigenstates of the Hamiltonian for  $s_r = 0.6$  and  $s_r = 0.4$ , and  $T_A = 100$ .

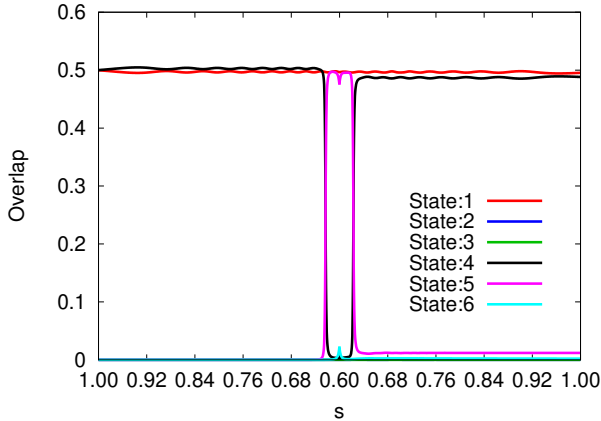


Figure 4.5.: Instantaneous overlap of the state of the system with the four lowest energy eigenstates of the Hamiltonian for  $s_r = 0.6$  and  $T_A = 100$ .

Starting first with the overlap of the state vector with the instantaneous low-lying states

of the Hamiltonian for  $s_r = 0.6$  (see Fig. 4.5), we observe that in this case, the amplitude present in the first state ( $|\nu_1\rangle$ ) stays approximately the same throughout the annealing process, except for small fluctuations. On the other hand, almost all of the amplitude present in the fourth state shifts to the fifth state at the anticrossing between them that occurs around  $s = 0.62$  (see the corresponding energy spectrum in Fig. 4.2). Some of the amplitude present in the fifth state then gets transferred to the sixth state at the anticrossing between the sixth and fifth energy states around  $s = 0.6$ , all of which returns to the fifth state as the forward part of the protocol starts at  $s_r = 0.6$ . Upon reaching  $s = 0.62$  most of the amplitude in the fifth state returns to the fourth state, though some of it still stays in the fifth state. From this point on, the amplitude present in the fourth state remains more or less constant.

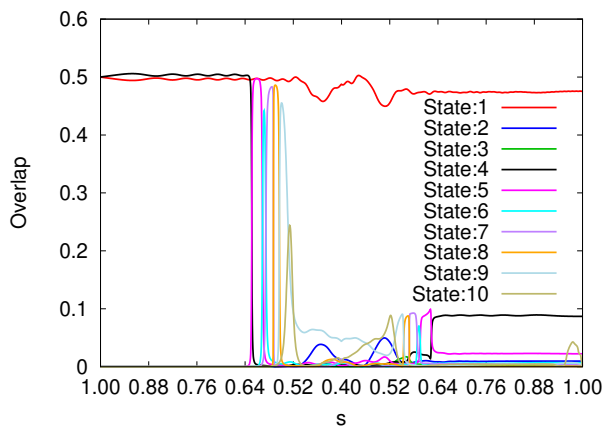


Figure 4.6.: Instantaneous overlap of the state of the system with the four lowest energy eigenstates of the Hamiltonian for  $s_r = 0.4$  and  $T_A = 100$ .

Moving on next to the instantaneous overlap corresponding to  $s_r = 0.4$ , shown in Fig. 4.6, we can immediately observe the involvement of the higher energy levels in this case. It can be noted that while the amplitude present in the first state still stays comparable to the initial amplitude at the end of the annealing algorithm, the amplitude present in the fourth state is significantly smaller at the end. We observe that the amplitude present in the fourth state goes up to the tenth state, following the intermediate states sequentially at the respective anticrossings (see Fig. 4.2 for the corresponding energy spectrum), from where most of the amplitude is lost to the higher excited states. The remaining amplitude returns to the fourth state following the same trajectory in the forward part of the anneal. Additionally, some of the amplitude present in the first state is shifted to the second state around the point of anticrossing between these two levels, which occurs around  $s = 0.42$ , but returns to the first state in the forward part of the annealing protocol. Another feature of interest observed in all the cases shown in Tab. 4.4 is that the sampling probability of the third ground state stays the smallest for all values of reversal distances. However, this probability increases as the value of the

reversal distance is decreased. This is an expected behavior, since for small enough  $s$  values, the third state can also be accessed via the other three lowest lying states through the relevant anticrossings.

### Varying the waiting time

Keeping the annealing time fixed at  $T_A = 100$ , and the reversal distance fixed at  $s_r = 0.7$ , we next investigate how the sampling probabilities of the ground states change with different waiting times. As before, we start with the first ground state as the initial state. The waiting time is varied from 0 to 40. With the chosen values of the annealing time and the reversal distance, the total success probability remains close to 1. In Fig. 4.7, we show the resulting sampling probabilities of the first and the third ground states. As the first observation, we note that on varying the waiting time  $T_W$ , the sampling probabilities of both the ground states oscillate. The reason behind this oscillation is that different components of the wavefunction (expressed in the instantaneous energy eigenbasis) acquire different phases, which depend on the duration of the wait. This results in different initial states for the forward part of the algorithm, which then lead to different sampling probabilities in the end. Secondly, from Fig. 4.7(b), we observe that although the sampling probability of the third ground state is also oscillating, the probability itself is of the order  $\mathcal{O}(10^{-6})$ .

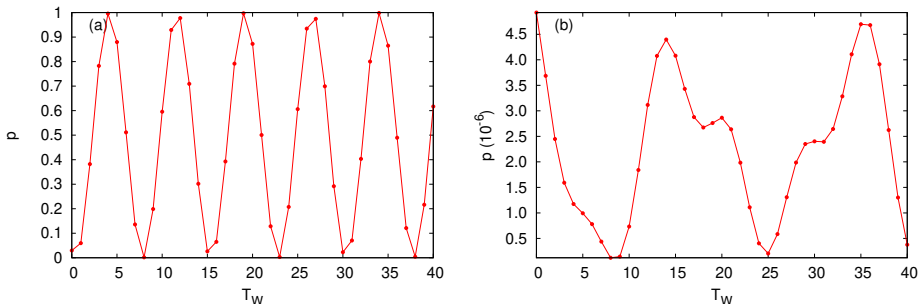


Figure 4.7.: Success probability of (a) the ground state  $|\psi_0^1\rangle$  and (b)  $|\psi_0^3\rangle$  as a function of different waiting times.

### A different choice for the initial state

Lastly, we discuss the effects of starting with a different ground state, namely the third ground state, whose sampling probability was found to be suppressed in the simulation for forward annealing for long annealing times. We vary the annealing time while setting  $s_r = 0.7$  and do not include any waiting times. The resulting sampling probabilities are given in Tab. 4.5. As before, for this setting, the total success probability remains close to 1. The main difference in this case, compared to the case where the system is initialized in the first ground state is that even for relatively smaller annealing times, e.g.,  $T_A = 10$ , most

Table 4.5.: Sampling probabilities of the degenerate ground states  $|\psi_0^i\rangle$ ,  $i = 1, 2, 3, 4$ , of the problem "230", corresponding to different annealing times  $T_A$ , where the reverse annealing time is chosen to be same as the forward annealing time. The initial state is chosen to be  $|\psi_0^3\rangle$ , the reversal distance is  $s_r = 0.7$ , and no waiting times are added.

State	$T_A = 10$	$T_A = 100$	$T_A = 1000$
$ \psi_0^1\rangle$	$1.47 \times 10^{-4}$	$4.92 \times 10^{-6}$	$3.21 \times 10^{-8}$
$ \psi_0^2\rangle$	$3.07 \times 10^{-4}$	$3.71 \times 10^{-3}$	$1.97 \times 10^{-5}$
$ \psi_0^3\rangle$	0.9963	0.9928	0.9996
$ \psi_0^4\rangle$	$4.28 \times 10^{-4}$	$3.41 \times 10^{-3}$	$1.72 \times 10^{-5}$
Total	0.9968	1.0000	1.0000

of the amplitude comes back to the state in which the algorithm starts, i.e.,  $|\psi_0^3\rangle$ , and thus the sampling probabilities of the other ground states remain fairly low. This is because for this problem the third ground state, or equivalently, the second excited state is decoupled from the rest of the four lowest lying instantaneous eigenstates according to perturbation theory. As per Eq. (4.3), the initial Hamiltonian cannot drive transitions between the second excited states, and the other three lowest lying energy states. Furthermore, as expected, with increasing annealing time, the sampling probability of the third ground state is found to increase.

#### 4.2.2. D-Wave results

Having discussed the performance of the ideal reverse annealing algorithm in the context of fairly sampling the ground states of degenerate problem Hamiltonians, we now turn to do the same using DWAdv. In doing so, we study the impact of the above-mentioned controls offered with the reverse annealing feature on the D-Wave systems one by one. It should however be emphasized here that the energy scale on the D-Wave annealers is very different from that in simulations, and the annealing time of 1000 in simulations roughly corresponds to 50 ns in the D-Wave systems. Another point of difference is that the D-Wave systems do not follow a linear annealing schedule, unlike the one chosen for the simulations.

#### Varying the annealing time

As in the case of simulations, we start with varying the annealing time, while keeping the reversal distance fixed at  $s_r = 0.7$  and without adding any waiting time. Once again, we choose the first ground state as the initial state. The obtained sampling probabilities are shown in Tab. 4.6. Firstly, we note that for the chosen parameters, the total success probability remains very close to 1. Secondly, in this case, we find the sampling probability of the third ground state, i.e., the energy eigenstate that is decoupled from the other lowest four eigenstates at  $s \approx 1$  as per Eq. (4.3), to be zero for all the considered annealing

Table 4.6.: Sampling probabilities of the degenerate ground states  $|\psi_0^i\rangle$ ,  $i = 1, 2, 3, 4$ , of the problem "230" obtained using DWAdv, corresponding to different annealing times  $T_A$ , where the reverse annealing time is chosen to be same as the forward annealing time. The initial state is chosen to be  $|\psi_0^1\rangle$ , the reversal distance is  $s_r = 0.7$ , and no waiting times are added.

State	$T_A = 0.5\mu s$	$T_A = 4\mu s$	$T_A = 10\mu s$	$T_A = 50\mu s$	$T_A = 100\mu s$	$T_A = 200\mu s$
$ \psi_0^1\rangle$	0.9991	0.9873	0.9805	0.6709	0.7380	0.5405
$ \psi_0^2\rangle$	0.0006	0.0063	0.0091	0.1470	0.1075	0.2490
$ \psi_0^3\rangle$	0	0	0	0	0	0
$ \psi_0^4\rangle$	0.0003	0.0064	0.0099	0.0830	0.1545	0.2105
Total	1.0000	1.0000	0.9995	0.9009	1.0000	1.0000

times. This suggests that just as for the simulation results with long annealing times, the initial Hamiltonian  $H_I$  cannot transfer amplitude from the other three of the four lowest instantaneous eigenstates to the second excited state in the D-Wave annealer too. However, it is seen that the sampling probability of the first ground state fluctuates as the annealing time increases, and gets distributed over the other two ground states, i.e.,  $|\psi_0^2\rangle$  and  $|\psi_0^4\rangle$ . Although on much longer annealing time scales, such a behavior is similar to that observed from the simulation results, and may be attributed to the interference between the phases acquired in the different components of the final state, when expressed in the eigenbasis of the perturbation matrix. In our results for the sampling probabilities using forward annealing, we observed that the D-Wave systems are not ideal, and noise and temperature effects also facilitate the exchange of amplitudes within the low-lying energy states of the annealing Hamiltonian, thereby affecting the sampling probabilities in case of forward annealing. However, in this case, since the sampling probability of the third ground state is found to be zero, this suggests that in this regime, the noise and temperature effects do not play as significant a role as in the case of forward annealing.

### Varying the reversal distance

Moving on to the effects that different reversal distances might have on the sampling probabilities, we vary the reversal distances between  $s_r = 0.8$  to  $s_r = 0.3$ , while keeping the annealing time  $T_A = 20\mu s$  fixed and choosing the first ground state to be the initial state, without adding any waiting times. Table 4.7 shows the obtained sampling probabilities. It is observed that the sampling probabilities of  $|\psi_0^2\rangle$ ,  $|\psi_0^3\rangle$ , and  $|\psi_0^4\rangle$  are non-zero. This can again be explained on the basis of the phases acquired by the different components of the final state and/or the noise and temperature effects which cause an exchange of amplitudes between the low-lying energy eigenstates of the Hamiltonian. While the sampling probability of the third ground state remains the smallest as compared to the other three ground states for all the values of  $s_r$ , this value increases as the value of the reversal distance is lowered. This can be understood on the basis of the anticrossing between instantaneous ground state and the first excited state (see Fig. 4.2). As in the

#### 4. Fair sampling

---

Table 4.7.: Sampling probabilities of the degenerate ground states  $|\psi_0^i\rangle$ ,  $i = 1, 2, 3, 4$ , of the problem "230" obtained using DWAdv, corresponding to different reversal distances  $s_r$ , with annealing time  $T_A = 20\mu s$ ,  $|\psi_0^1\rangle$  as the initial state, and without any waiting time.

State	$s_r = 0.3$	$s_r = 0.4$	$s_r = 0.5$	$s_r = 0.6$	$s_r = 0.7$	$s_r = 0.8$
$ \psi_0^1\rangle$	0.2173	0.4080	0.3412	0.3120	0.9287	1.0000
$ \psi_0^2\rangle$	0.2468	0.3235	0.4269	0.4075	0.0401	0
$ \psi_0^3\rangle$	0.1725	0.0065	0.0005	0	0	0
$ \psi_0^4\rangle$	0.2665	0.2556	0.2279	0.2751	0.0295	0
Total	0.9031	0.9936	0.9965	0.9946	0.9983	1.0000

case of the simulations, in the case of the D-Wave system also we observe that some of the amplitude from the state vector can leak out to higher excited states when one reaches  $s$  values close to those corresponding to the cascade of anticrossings. This can also render the second excited state accessible, which is otherwise decoupled from three of the of the lowest four instantaneous eigenvectors of the annealing Hamiltonian in the limit  $s \approx 1$  according to perturbation theory.

#### Varying the waiting time

Next, we focus on the effects of choosing different waiting times  $T_W$  on the sampling probabilities. For this we fix  $T_A = 4\mu s$ ,  $s_r = 0.7$ , and start with the first ground state as the initial state. The obtained sampling probabilities are shown in Tab. 4.8. Although for short waiting times, we obtain the first ground state as the most probable state, as the waiting time increases the sampling probability of the  $|\psi_0^1\rangle$  decreases, albeit with some fluctuations. This can be explained on the basis of accumulation of different phases in the components corresponding to the instantaneous energy states, and the noise and temperature effects present in the system. On the other hand, though the sampling probability of  $|\psi_0^1\rangle$  is found to be oscillating, the sampling probability of the third ground state stays exactly zero.

Table 4.8.: Sampling probabilities of the degenerate ground states  $|\psi_0^i\rangle$ ,  $i = 1, 2, 3, 4$ , of the problem "230" obtained using DWAdv, corresponding to different waiting times  $T_W$ , with  $T_A = 4\mu s$ . The initial state is chosen to be  $|\psi_0^1\rangle$ , and the reversal distance is  $s_r = 0.7$ .

State	$T_W = 5\mu s$	$T_W = 10\mu s$	$T_W = 20\mu s$	$T_W = 50\mu s$	$T_W = 100\mu s$	$T_W = 500\mu s$	$T_W = 1000\mu s$
$ \psi_0^1\rangle$	0.7904	0.6894	0.4114	0.3161	0.1480	0.2490	0.1888
$ \psi_0^2\rangle$	0.0968	0.1674	0.3092	0.2558	0.1479	0.4410	0.1988
$ \psi_0^3\rangle$	0	0	0	0	0.0066	0.0010	0.0112
$ \psi_0^4\rangle$	0.1102	0.1403	0.2617	0.4271	0.1304	0.2210	0.2250
Total	0.9974	0.9971	0.9922	0.9990	0.4329	0.9120	0.6238

On a side remark, we note that except for annealing times  $T_W = 100 \mu s$  and  $T_W = 1000 \mu s$ , the total success probability stays close to 1, which is expected for the chosen annealing time and the reversal distance. Since the total success probability should ideally be independent of the waiting time, the values obtained for these two annealing times appears to be an anomaly. As the DWAdv system has been replaced by Advantage\_system5.3 in the mean time, we rerun the 14-variable problem labelled as "230" on this solver. The resulting sampling probabilities are given in Tab. 4.9. Not only do the results obtained from the rerun of the problem have a larger total success probability for  $T_A = 100, 1000 \mu s$ , but the total success probability is obtained to be one for all the waiting times now, while the sampling probability of the third ground state is exactly zero for all waiting times, suggesting that the new system has certain improvements compared to the previous version of DWAdv.

Table 4.9.: Sampling probabilities of the degenerate ground states  $|\psi_0^i\rangle$ ,  $i = 1, 2, 3, 4$ , of the problem "230" obtained using Advantage\_system5.3, corresponding to different waiting times  $T_W$ , with  $T_A = 4\mu s$ . The initial state is chosen to be  $|\psi_0^1\rangle$ , and the reversal distance is  $s_r = 0.7$ .

State	$T_W = 5\mu s$	$T_W = 10\mu s$	$T_W = 20\mu s$	$T_W = 50\mu s$	$T_W = 100\mu s$	$T_W = 500\mu s$	$T_W = 1000\mu s$
$ \psi_0^1\rangle$	0.7621	0.5577	0.5225	0.3152	0.4205	0.4680	0.4050
$ \psi_0^2\rangle$	0.0994	0.2148	0.2026	0.4306	0.2990	0.3000	0.3262
$ \psi_0^3\rangle$	0	0	0	0	0	0	0
$ \psi_0^4\rangle$	0.1385	0.2275	0.2749	0.2542	0.2805	0.2320	0.2688
Total	1.0000	1.0000	1.0000	1.0000	1.0000	1.0000	1.0000

### A different choice for the initial state

Lastly, we focus on the sampling performance of the reverse annealing feature of the D-Wave system when the system is initialized in a state different from first the ground state. As for the simulations, we choose the third ground state for this purpose, and look at the success probabilities of the four ground states for different annealing times, reversal distances, and waiting times.

We start by discussing the effects of varying the annealing times on the sampling probabilities of the ground states. These results are not shown explicitly. In this case, we note that for various annealing times chosen (ranging from 4 to 500  $\mu s$ ) and  $s_r = 0.7$ ,  $|\psi_0^3\rangle$  is sampled with a probability larger than 0.9, except for  $T_A = 500 \mu s$ , where the sampling probability is 0.7945. The sampling probability of the other ground states is found to be zero. This is in contrast to the system being initialized in the first ground state, where the sampling probability of the other ground states, except for the third ground state, was observed to be non-zero. Such a result suggests that the sampling behavior from DWAdv is consistent with the perturbation matrix Eq. (4.3), according to which the second excited state of the instantaneous Hamiltonian at  $s \approx 1$  does not have any overlap with the other lowest four eigenstates. Similar results (not shown) are obtained upon adding different waiting times (with  $T_A = 4 \mu s$  and  $s_r = 0.7$ ). Changing the reversal distance while keeping

all the other parameters fixed results in a similar sampling behavior as noted when the system is initialized in  $|\psi_0^1\rangle$  (see Tab. 4.10).

Table 4.10.: Sampling probabilities of the degenerate ground states  $|\psi_0^i\rangle$ ,  $i = 1, 2, 3, 4$ , of the problem "230" obtained using DWAdv, corresponding to different reversal distances  $s_r$ , with annealing time  $T_A = 20\mu s$  and  $|\psi_0^3\rangle$  as the initial state, and without any waiting time.

State	$s_r = 0.3$	$s_r = 0.4$	$s_r = 0.5$	$s_r = 0.6$	$s_r = 0.7$	$s_r = 0.8$
$ \psi_0^1\rangle$	0.2642	0.1109	0.0165	0	0	0
$ \psi_0^2\rangle$	0.2267	0.1033	0.0357	0.0001	0	0
$ \psi_0^3\rangle$	0.1086	0.4304	0.8473	0.9329	0.9953	1.0000
$ \psi_0^4\rangle$	0.3603	0.1682	0.0231	0.0002	0	0
Total	0.9598	0.8128	0.9226	0.9332	0.9953	1.0000

### 4.3. Summary

Although the success probability of finding the correct solution is the main metric used for gauging the performance of approaches like quantum annealing for solving optimization problems, there are a few other performance measures that become relevant in specific contexts. One such measure is the efficiency of quantum annealing in yielding all the solutions to an optimization problem with more than one possible solution, which was the focus of this chapter. To this end, we studied two annealing protocols using both simulations as well as the D-Wave quantum annealer Advantage\_system5.1 (DWAdv). The first protocol used was the standard quantum annealing protocol, in which the system starts in a uniform superposition state and slowly approaches a classical state, which should ideally be the solution to the encoded optimization problem. The other protocol was the reverse annealing protocol, as implemented by D-Wave, wherein the system starts in a low-energy classical state, and anneals backwards up to a certain reversal distance, by increasing the strength of the transverse field, which is then lowered to return to a classical state again. This was done in the hope of finding more than one degenerate ground state of the problem Hamiltonian.

For the purpose of this study, we used a set of newly constructed 2-SAT problems with four satisfying assignments, with the number of variables in the problems varying from  $6 \leq N \leq 20$ . Using simulations and DWAdv, we then studied the sampling probabilities of four ground states of all the problem Hamiltonians for different annealing times.

While for a majority of the problems we found the simulations for the standard quantum annealing algorithm to sample the ground states with approximately equal probabilities, for a few problems the sampling probability of one of the ground states was found to be totally suppressed, even for long annealing times. This could be justified on the basis of perturbation theory and we focused on such problems for understanding how the two protocols sample the ground states for different choices of annealing parameters. Such a

suppression was not observed if the chosen annealing time was short, in which case the total success probability (the sum of the sampling probabilities of the four ground states) was found to be small. This could be explained on the basis of the energy spectrum of the annealing Hamiltonian. Furthermore, using the reverse annealing protocol, we did find a suppression in the sampling probability of the ground state theoretically predicted to have a zero sampling probability. The sampling behavior in this case depended significantly on the choice of the parameters like the annealing time, reversal distance, inclusion of a waiting time at the point of reversal, and the initial state, and could be uniform for a few choices of these parameters.

Employing the DWAdv system, a similar analysis for gauging the sampling behavior was performed. In the case of standard quantum annealing, however, we did not witness any suppression in the sampling probability of any ground state, and the four ground states were sampled with an almost equal probability of 0.25. This made apparent that the D-Wave systems are not ideal quantum annealers, and noise and temperature effects play a significant role in their performance. On the other hand, for the reverse annealing protocol the results were in better agreement with the theoretical predictions based on the ideal system, i.e., we could observe a suppression in the sampling probability of a ground state, although as for the simulations, the annealing controls played a major role in deciding the sampling behavior. We therefore concluded that in the regime of large reversal distances like  $s_r = 0.7$ , the noise and temperature effects play a less significant role in the D-Wave system.



## 5. Adding the trigger Hamiltonian

So far, we have only considered annealing Hamiltonians and annealing features that could be implemented on real quantum annealers, like the ones from D-Wave Inc. In this chapter we expand the scope of the discussion beyond such Hamiltonians using simulations. The focus of this chapter is therefore on the performance of the ideal annealing algorithm, i.e., annealing in the absence of temperature and noise effects. We start with the quantum annealing Hamiltonian that consists of the standard initial Hamiltonian, i.e., the uniform transverse Hamiltonian given by Eq. (1.20), and the final problem Hamiltonian that encodes the optimization problem that needs to be solved, and choose a linear annealing scheme. In addition to the set of 2-SAT problems, we use sets of nonstoquastic problems constructed using the 2-SAT problems for benchmarking the quantum annealing algorithm.

There are numerous studies indicating that introducing modifications to the standard algorithm for quantum annealing can have considerable effects on its performance. These include exploring different choices for the initial Hamiltonian, modifying the annealing path, inclusion of nonstoquastic terms in the annealing Hamiltonian, and manipulating the anneal path for each qubit individually [FGG02; Far+09; MNK09; SN12a; SN12b; Cro+14; SN15; ZZS16; NT17; Hor+17; ÖJV18; Alb19; Hsu+19; Kön+19; TYN20; Cha20; Meh+21]. The effects of these modifications depend also on the optimization problem at hand.

In this chapter, we focus on the performance of the quantum annealing Hamiltonian with the introduction of an additional term, called the trigger Hamiltonian, to the standard quantum annealing Hamiltonian given by Eq. (1.19), for solving the given sets of 2-SAT and nonstoquastic problems. The trigger Hamiltonian is chosen to consist of transverse couplings, which vanish at the beginning and the end of the annealing process. This ensures that one can still start in the easy-to-prepare ground state of the initial Hamiltonian, and obtain the solution to the given problem at the end of the algorithm. We choose a linear scheme for the initial and the final Hamiltonians, such that,

$$H(t) = (1 - s)H_I + s(1 - s)H_T + sH_P, \quad (5.1)$$

where  $H_T = -g \sum J_{i,j}^x \sigma_i^x \sigma_j^x$ , and parameter  $g$  controls the strength of the trigger Hamiltonian. In this work, we only consider trigger Hamiltonians of the ferromagnetic ( $J = 1$ ) and antiferromagnetic ( $J = -1$ ) kind [Hor+17], and leave the study of other types for future research.

As discussed in section 1.3, nonstoquastic Hamiltonians can have positive and/or imaginary off-diagonal elements when represented in the computational basis. Such Hamiltonians cannot be efficiently simulated using quantum Monte Carlo methods due to the sign problem [Loh+90; TW05; GH20]. There are various studies suggesting that the

inclusion of a nonstoquastic term in the quantum annealing Hamiltonian can be beneficial for its performance [SN12a; Hor+17; NT17; SJN17; Alb19; Cro+20; Lyk+21]. The addition of the antiferromagnetic trigger Hamiltonian makes the annealing Hamiltonian nonstoquastic, and it is therefore interesting to study its effect on the performance of quantum annealing. We also utilize quantum annealing for solving nonstoquastic problem Hamiltonians, by extending the set of problem Hamiltonians corresponding to the 2-SAT problems, by adding couplings along the  $y$ - direction, with strength 0.5, according to the graph of the 2-SAT problem Hamiltonian, i.e.,

$$H_P = - \sum_i h_i^z \sigma_i^z - \sum_{i,j} \left( J_{i,j}^z \sigma_i^z \sigma_j^z + \frac{1}{2} \sigma_i^y \sigma_j^y \right). \quad (5.2)$$

In the following subsections, we discuss the effects of adding the two types of trigger Hamiltonians, with three choices of the strength parameter, namely,  $g = 0.5, 1.0, 2.0$ , on the performance of quantum annealing in terms of the minimum energy gap between the ground state and the first excited state of the annealing Hamiltonian (determined using the Lanczos algorithm), and the final success probability corresponding to different annealing times (making use of the Suzuki-Trotter product formula algorithm). In addition, by investigating a few individual cases, we identify some of the non-adiabatic mechanisms that can be advantageous for the performance of quantum annealing.

We choose three sets of 2-SAT and nonstoquastic problems, with problem sizes  $N = 8, 12$  and 18. As we observe similar results for the three problem sets, we only show the ensemble results for the  $N = 18$  sets, while the results from  $N = 12$  sets are shown as examples for some special cases.

In this chapter, we showcase the results obtained from implementing the standard quantum annealing Hamiltonian, as well as the annealing Hamiltonians with the ferromagnetic and the antiferromagnetic trigger Hamiltonians, for solving the sets of 2-SAT and nonstoquastic problems. We start by discussing the results for the 18-variable 2-SAT problems, and then focus on the results for the nonstoquastic problems.

## 5.1. 2-SAT problems

In the following subsections, we discuss the performance of the three variants of the quantum annealing algorithm introduced above, one by one.

### 5.1.1. Standard Hamiltonian

We start with the analysis of the performance of the standard quantum annealing Hamiltonian, given by Eq. (1.19) for solving the 2-SAT problems. First, we determine the minimum energy gap  $\Delta^O$  between the ground state and the first excited state of the annealing Hamiltonian, for all the 2-SAT problems. Then, we perform the simulations for the dynamics of the quantum annealing algorithm for all the problems, using annealing times  $T_A = 10, 100, 1000$  and 10000. Since the ground state of these problems is already known, the success probability  $p^O$  is then obtained by computing the overlap of the final state resulting from the algorithm with the known ground state of the problem.

As explained in section 1.3.2, if the annealing time chosen is sufficiently long for the evolution to be almost adiabatic, Eq. (1.24) can give an estimate of the success probability in terms of the minimum energy gap between the relevant energy levels. Following the same argument, if the success probability can show a Landau-Zener like dependence on the minimum energy gap between the ground state and the first excited state, the evolution of the state during the annealing process can be taken to be roughly adiabatic. To investigate these aspects, in Fig. 5.1 we show the scatter plot of the success probability  $p^O$ , against the minimum energy gap  $\Delta^O$ . Fixing the parameter  $b$  obtained from fitting the function

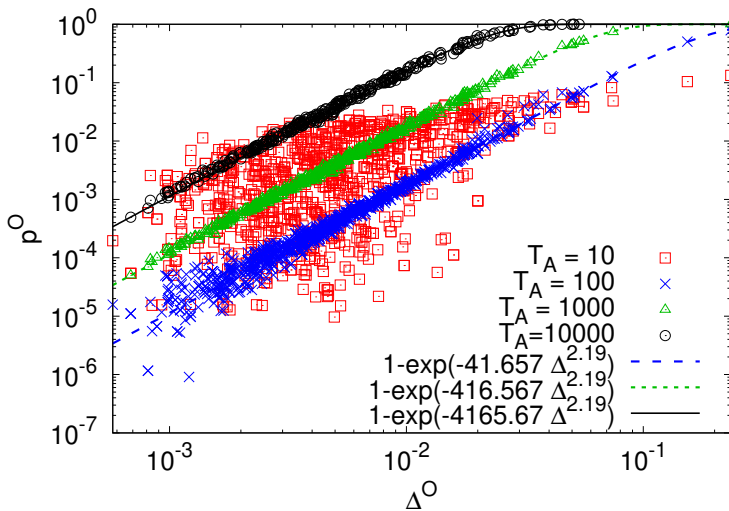


Figure 5.1.: Success probability  $p^O$  versus minimum energy gap  $\Delta^O$  for 18-variable 2-SAT problems for various annealing times  $T_A$ , for the standard quantum annealing Hamiltonian given by Eq. (1.19).

$p = 1 - \exp(-a\Delta^b)$  to the data corresponding  $T_A = 10000$ , we reduce the parameter  $a$  by a factor of 10 and 100 for the fits for the data corresponding to  $T_A = 1000$  and  $T_A = 100$ , respectively. The resulting curves match well with the data, and the exponent  $b$  is found to be 2.19. This makes the form of the fitting function similar to the Landau-Zener formula Eq. (1.24), for which  $b = 2$ , and parameter  $a$  is related to the inverse of the speed of sweep. The formula therefore predicts an increase in the success probability as the annealing time increases, which can also be observed from Fig. 5.1. Although the Landau-Zener formula is derived for a two-level system, it seems that its predictions also hold for more complicated systems if the chosen annealing times are sufficiently long, i.e., in the limit where the system can be approximated by a two-level system. However, in this case, the parameter  $b$  can deviate slightly from 2, as is true for the 18-variable problems considered here. For short annealing times, on the other hand, the success probability need not follow the Landau-Zener formula, and hence, we observe a significant scattering in the data corresponding to  $T_A = 10$  in Fig. 5.1. A fit for the data corresponding to

$T_A = 10$  has been omitted for this reason. As shall become clear from section 5.1.3, for the annealing time  $T_A = 10$ , the non-adiabatic mechanism of fast annealing can enhance the success probability despite of a small minimum energy gap.

Furthermore, it can be noted from Fig. 5.1 that even for an annealing time  $T_A = 10000$ , the success probability for the problems with small minimum energy gaps (present in the tail of the fitting functions) is on the order of  $\mathcal{O}(10^{-3})$ . Although these problem sizes are rather small, i.e.,  $N \leq 18$ , these problems are hard to solve using the standard quantum annealing Hamiltonian.

### 5.1.2. Hamiltonian with the ferromagnetic trigger Hamiltonian

Next, we analyze the effects of adding the ferromagnetic trigger Hamiltonian to the standard quantum annealing Hamiltonian given by Eq. (1.19) in terms of the minimum energy gap and the success probability of the annealing Hamiltonian.

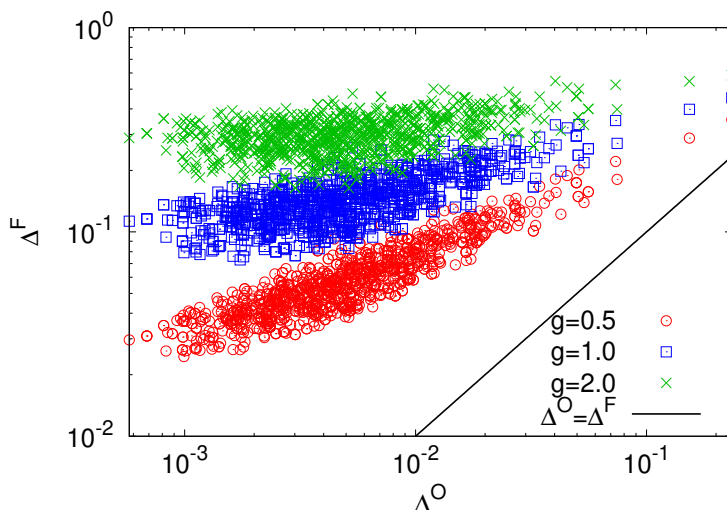


Figure 5.2.: Minimum energy gap  $\Delta^F$  for 18-variable 2-SAT problems after adding the ferromagnetic trigger Hamiltonian to the standard quantum annealing Hamiltonian Eq.(1.19) versus minimum energy gap  $\Delta^O$  without adding the trigger Hamiltonian, for various trigger strengths  $g$ .

As noted from the adiabatic theorem (Eq. (1.22)), the minimum energy gap between the ground state and the first excited state of the annealing Hamiltonian is crucial for the performance of the annealing algorithm. We therefore start by observing how the inclusion of the ferromagnetic trigger Hamiltonian affects the minimum energy gaps. We find that the number of anticrossings between the ground state and the first excited state does not change upon adding the ferromagnetic trigger Hamiltonian, but the position of the anticrossings shifts towards larger values of  $s$ . Figure 5.2 shows a scatter plot of the minimum

energy gaps  $\Delta^F$  upon adding the ferromagnetic trigger Hamiltonian (Eq. (5.1)), against the minimum energy gaps  $\Delta^O$  from the standard annealing Hamiltonian (Eq. (1.19)), for the problem set with  $N = 18$  and  $g = 0.5, 1.0, 2.0$ . In this case, we observe an enlargement of the minimum energy gaps for all the problems belonging to the set, and for all the chosen  $g$  values. Furthermore, we observe that the enlargement of the minimum energy gaps increases as the strength of the trigger Hamiltonian increases.

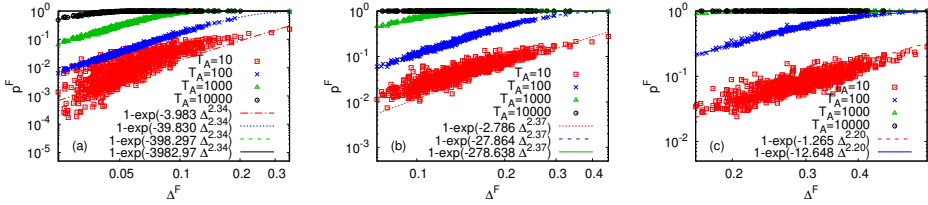


Figure 5.3.: Success probability  $p^F$  versus the minimum energy gap  $\Delta^F$  for the 18-variable 2-SAT problems upon adding the ferromagnetic trigger Hamiltonian to the Hamiltonian Eq. (1.19) for trigger strengths (a)  $g = 0.5$ , (b)  $g = 1.0$  and (c)  $g = 2.0$ .

In Fig. 5.3, we show scatter plots of the success probability  $p^F$  obtained upon adding the ferromagnetic trigger Hamiltonian to the annealing Hamiltonian given by Eq. (1.19), against the resulting minimum energy gap  $\Delta^F$  for  $g = 0.5, 1.0, 2.0$ . We observe a successive increase in the success probability with increasing annealing time, as well as increasing strength of the trigger Hamiltonian. Such a behavior follows from the Landau-Zener theory, where for a given minimum energy gap the success probability increases with increasing annealing time, and for a given annealing time, an increase in the minimum energy gap (in this case, a consequence of increasing the trigger strength) also leads to an increase in the success probability. Furthermore, as in the previous section, the Landau-Zener kind of curves are found to fit the data well, with parameter  $b$  ranging between the values of 2.20 and 2.34. Although there is some scattering of the data points at the tail for  $T_A = 10$ , its extent is much smaller compared to that obtained with the standard annealing Hamiltonian (Fig. 5.1).

Next, in order to understand the extent to which adding the ferromagnetic trigger Hamiltonian can enhance the success probability, in Fig. 5.4 we show the distribution of the relative success probability, defined as the ratio of the success probability obtained upon adding the trigger Hamiltonian with a certain strength to that obtained from the standard quantum annealing Hamiltonian, for  $g = 0.5, 1.0, 2.0$  and  $T_A = 10, 100, 1000$ . From the figure it can be clearly seen that the success probabilities resulting from the quantum annealing Hamiltonian with the ferromagnetic trigger (Eq. (5.1)) are larger than the success probabilities obtained from the standard quantum annealing Hamiltonian (Eq. (1.19)), i.e.,  $p^F/p^O > 1$ , for all  $g$  and  $T_A$ , except for 17 problems with  $g = 0.5$  and  $T_A = 10$ . The latter observation can be explained on the basis of the flat tail observed in Fig. 5.1 for  $T_A = 10$  due to the non-adiabatic mechanism of fast annealing (discussed in Section 5.1.3) for the standard quantum annealing Hamiltonian (Eq. (1.19)), which

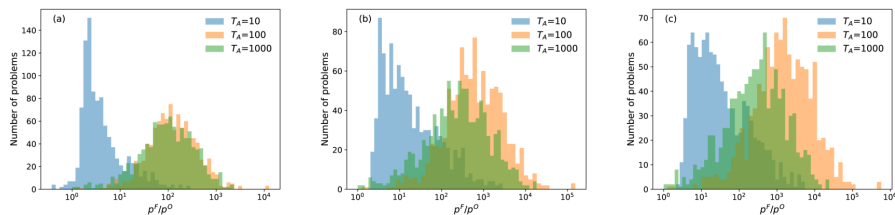


Figure 5.4.: Distribution for the relative success probability  $p^F/p^O$  upon adding the ferromagnetic trigger Hamiltonian to the Hamiltonian Eq. (1.19) with trigger strengths (a)  $g=0.5$ , (b)  $g=1.0$  and (c)  $g=2.0$  for annealing times  $T_A = 10, 100, 1000$ .

results in a relatively large  $p^O$ . We also note that the relative success probability is at least of the order  $\mathcal{O}(10^2)$  for long annealing times  $T_A = 100$  and  $1000$  for the three values of  $g$  studied. Another observation that follows from the figure is that upon increasing the strength of the trigger Hamiltonian, the number of problems with a large relative success probability increases systematically for all values of  $T_A$ . This can be attributed to the systematic increase in the minimum energy gap as the strength of the ferromagnetic trigger Hamiltonian increases (see Fig. 5.2). Furthermore, it can be noted that although the distributions of  $p^F/p^O$  corresponding to  $T_A = 100$  and  $T_A = 1000$  are similar in the case where the trigger is added with a strength  $g = 0.5$ , as the trigger strength increases, the maximum value of the relative success probability corresponds to  $T_A = 100$  and not  $T_A = 1000$ . This can be explained on the basis of Fig. 5.1 from where it is evident that for a majority of the problems the success probability  $p^O$  is the smallest for  $T_A = 100$  (on the order of  $\mathcal{O}(10^{-6})$  in the worst case), while upon adding the ferromagnetic trigger (see Fig. 5.3) the success probability  $p^F$  is significantly enlarged (on the order of  $\mathcal{O}(10^{-1})$  in the worst case). As the annealing time increases from  $T_A = 100$  to  $1000$ ,  $p^O$  improves significantly but there is no margin for that large improvement in  $p^F$ . Thus, for the ferromagnetic trigger Hamiltonian, we obtain the largest value of the relative success probability for  $g = 2.0$  and  $T_A = 100$  (almost  $\mathcal{O}(10^6)$ ).

### 5.1.3. Hamiltonian with the antiferromagnetic trigger Hamiltonian

In addition to altering the minimum energy gaps between the ground state and the first excited state of the annealing Hamiltonians, the addition of the antiferromagnetic trigger Hamiltonian to the standard quantum annealing Hamiltonian (Eq. (1.19)) can vastly affect the energy spectrum of the annealing Hamiltonian in other ways. The most prominent of these changes is the increase in the number of anticrossings between the ground state and the first excited state of the annealing Hamiltonian. As can be seen from Tab. 5.1, a majority of the problems have more than one anticrossing with the addition of the antiferromagnetic trigger. Furthermore, the number of problems with a larger number of anticrossings between the lowest two energy levels increases as the strength of the trigger is increased, such that for  $g = 2.0$ , a maximum number of problems have four such

Table 5.1.: Number of 18-variable 2-SAT problems with different numbers of anticrossings,  $N_A$ , after adding the antiferromagnetic trigger Hamiltonian with strengths  $g$ , to the Hamiltonian Eq. (1.19). The whole set consists of 1000 problems.

$N_A$	$g = 0.5$	$g = 1.0$	$g = 2.0$
1	796	37	0
2	204	394	24
3	0	468	182
4	0	99	424
5	0	2	290
6	0	0	68
7	0	0	12

anticrossings, while the maximum number of anticrossings is seven. The addition of the antiferromagnetic trigger Hamiltonian can also lead to a stretching of the anticrossing (such that the lowest two states stay in close vicinity for a more extended range of the annealing parameter  $s$ ), and a leftward shift in the position of the anticrossings, i.e., to a smaller value of  $s$ . Thus the inclusion of the antiferromagnetic trigger Hamiltonian can affect the performance of the quantum annealing algorithm in various ways, which depends greatly on the problem itself. In the present section, we study the effects of adding the antiferromagnetic trigger on the performance of the quantum annealing algorithm by conducting a similar analysis as with the ferromagnetic trigger Hamiltonian, and inspect a few individual cases to identify some non-adiabatic mechanisms accompanied with the addition of the former.

Table 5.2.: Number of 18-variable 2-SAT problems with increased success probabilities after adding the antiferromagnetic trigger with strengths  $g$ , to the Hamiltonian Eq. (1.19). The whole set consists of 1000 problems.

$g$	$T_A = 10$	$T_A = 100$	$T_A = 1000$
0.5	732	10	3
1.0	627	798	992
2.0	41	754	844

Starting with the analysis of the minimum energy gap, we note that the inclusion of the antiferromagnetic trigger Hamiltonian can either increase or decrease the minimum energy gap between the ground state and the first excited state, in comparison to that of the standard quantum annealing Hamiltonian. For the set of 1000 2-SAT problems with  $N = 18$ , only 4 out of the 1000 problems are found to have a larger minimum energy gap compared to that of the standard quantum annealing Hamiltonian for  $g = 0.5$ , but this number increases to 565 and 792 for  $g = 1.0$  and  $g = 2.0$ , respectively. While this trend of increasing number of cases with an enlarged minimum energy gap as a consequence of

## 5. Adding the trigger Hamiltonian

adding the antiferromagnetic trigger Hamiltonian with higher strength is also present for the problem set with  $N = 12$ , only a small fraction of problems have a larger minimum energy gap for  $g = 2.0$  (202 problems out of the set of 1000 problems).

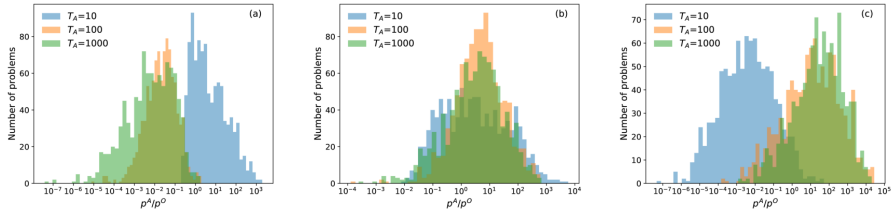


Figure 5.5.: Distribution for the relative success probability  $p^A/p^O$  upon adding the antiferromagnetic trigger Hamiltonian to the Hamiltonian Eq. (1.19) with trigger strengths (a)  $g=0.5$ , (b)  $g=1.0$  and (c)  $g=2.0$  for  $T_A = 10, 100, 1000$ .

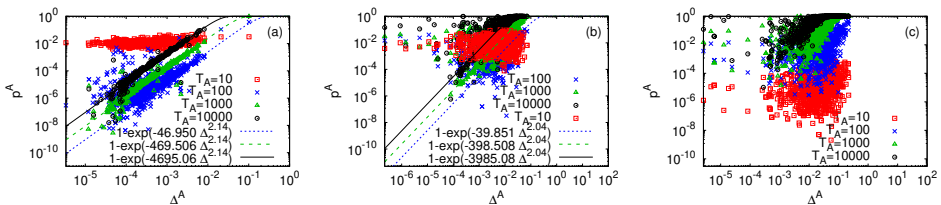


Figure 5.6.: Success probability  $p^A$  versus the minimum energy gap  $\Delta^A$  for the 18-variable 2-SAT problems upon adding the antiferromagnetic trigger Hamiltonian to the Hamiltonian Eq. (1.19) for trigger strengths (a)  $g = 0.5$ , (b)  $g = 1.0$  and (c)  $g = 2.0$ .

Like the minimum energy gaps, the success probability obtained from the annealing Hamiltonian upon adding the antiferromagnetic trigger Hamiltonian can also be smaller or larger than that obtained using the standard quantum annealing Hamiltonian, as shown in Tab. 5.2. For understanding the extent of the increase or decrease in the success probability, Fig. 5.5 shows the distribution of the relative success probability  $p^A/p^O$  when the antiferromagnetic trigger Hamiltonian with  $g = 0.5, 1.0, 2.0$  is added and  $T_A$  is chosen to be 10, 100, or 1000. A couple of observations follow from this figure. We note that for the case where the antiferromagnetic trigger Hamiltonian is added with strength  $g = 0.5$ , not only a majority of the problems have a significantly larger success probability for  $T_A = 10$ , but also the relative success probability is larger ( $\mathcal{O}(10^3)$ ) compared to that for  $T_A = 100$  and 1000. It can also be seen that for this case the smallest relative success probability is of the order  $\mathcal{O}(10^{-8})$  and corresponds to  $T_A = 1000$ . These observations are somewhat counter-intuitive and can be explained on the basis of the non-adiabatic mechanisms (discussed below) which play a significant role in the dynamics when the antiferromagnetic trigger Hamiltonian is added to the annealing Hamiltonian (Eq. (1.19)). Next, we observe

that as the strength of the antiferromagnetic trigger Hamiltonian increases to  $g = 1.0$  and  $g = 2.0$ , the distribution of  $p^A/p^O$  changes considerably. While for  $g = 1.0$  the spread of the relative success probabilities is similar for all the annealing times, for  $g = 2.0$  the values for the relative success probability is larger for  $T_A = 100$  and  $1000$  compared to that for  $T_A = 10$ . This is related to the increase in the minimum energy gaps as the strength of the antiferromagnetic trigger increases. The largest value of the relative success probability is found to be of the order  $\mathcal{O}(10^4)$  for  $g = 2.0$  and  $T_A = 100$  and  $1000$ .

Coming now to the success probability versus minimum energy gap plots, shown in Fig. 5.6, we observe a much more significant scattering in the data as compared to that for the standard annealing Hamiltonian as the strength of the trigger Hamiltonian increases. This can be explained on the basis of an increase in the number of anticrossings between the ground state and the first excited state as the strength of the trigger Hamiltonian increases. It can also be noted, that the distribution of the data points corresponding to  $T_A = 10$  and  $g = 0.5$  is rather flat. Since for  $g = 0.5$ , the minimum energy gap is reduced for almost all the problems of the set, the annealing time  $T_A = 10$  is too short for the system to follow the Landau-Zener formula. Such a behavior of the success probability is similar to the one where noise is present in the system, or when the system is coupled to a heat bath, and the transitions from the ground state to the higher states can occur at points other than those corresponding to the  $s$  value of the anticrossings. As the annealing time increases, the success probability follows the Landau-Zener formula more closely. Furthermore, as the minimum energy gaps increase with increasing strength of the trigger Hamiltonian, the flatness in the distribution of the data points corresponding to  $T_A = 10$  decreases.

The flatness in the distribution of the success probabilities for  $T_A = 10$  and  $g = 0.5$  suggests that despite of a small value of the minimum energy gap between the ground state and the first excited state, the resulting success probability is large. Moreover, there is a decrease in the success probability as the annealing time increases. Both these observations are incompatible with the implications of the Landau-Zener formula. To give plausible explanations for such observations, we look at some of the 12-variable problems, and identify three non-adiabatic mechanisms that are noted to be beneficial for the resulting success probability.

- Fast annealing: Although according to the Landau-Zener formula, long annealing times are required for high success probabilities, in some cases, a short annealing time can prove to be more advantageous than a longer intermediate value of annealing time. An example of one such problem is shown in Fig. 5.7 for  $g = 0.5$ . In this case, with an annealing time  $T_A = 100$ , the state of the system follows the instantaneous ground state closely till the point of anticrossing between the ground state and the first excited state. Upon reaching the anticrossing, however, the state of the system shifts most of its amplitude to the first excited state. As a consequence, the final state at the end of the annealing process has a small overlap with the ground state of the problem Hamiltonian, therefore resulting in a small success probability.

On the other hand, for a too short annealing time  $T_A = 10$ , the system state already deviates from the ground state before reaching the anticrossing. In this case, some

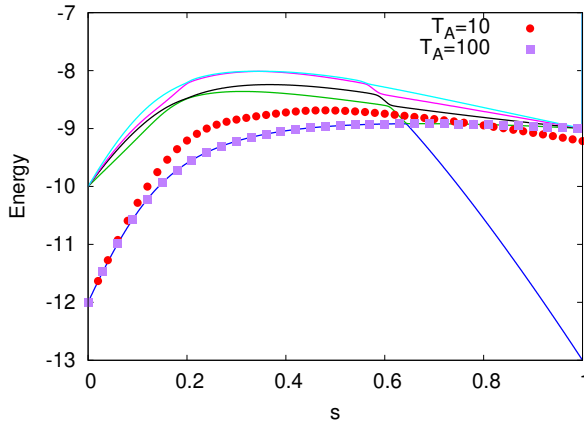


Figure 5.7.: Energy spectrum of the lowest lying states for a 12-variable problem showing fast annealing in the case that  $g = 0.5$ . The solid lines represent the energy spectrum of the lowest lying states of the problem while the markers represent the average energy of the instantaneous state of the system for  $T_A = 10$  and 100.

of the amplitude shifted to the first excited state returns to the ground state at the anticrossing, thereby increasing the final success probability. In some other cases it is found that even if the energy of the final state with  $T_A = 10$  is larger than that compared to  $T_A = 100$ , the resulting success probability can still be higher for the former. This is because in these cases the state of the system closely follows the first excited state after the anticrossing for  $T_A = 100$ , which has a negligible overlap with the ground state, while the combination of higher excited states that the system ends in with  $T_A = 10$  can coincidentally have a larger overlap with the ground state. Such an observation is also noted in [Cro+14].

- Even number of comparably small anticrossings: Another possible non-adiabatic mechanism observed to be beneficial for the success probability is the presence of an even number of comparably small anticrossings between the ground state and the first excited state of the annealing Hamiltonian, as shown in Fig. 5.8(a) for a 12-variable problem corresponding to  $g = 2.0$  with two anticrossings ( $s = 0.165$  and  $s = 0.248$ ) (indicated by the two dotted circles in the figure). For the given set of 2-SAT problems, such a combination of comparably small and even number of anticrossings is found to be rather rare, and we find at most two such anticrossings. From Fig. 5.8(b) for the overlap of the state of the system with the instantaneous ground state, first excited state, and the second excited state of the Hamiltonian, we can see that the amplitude from the system state is transferred from the ground state to the first excited state at the first anticrossing. Upon reaching the second anticrossing at  $s = 0.248$ , most of this amplitude returns to the ground state. This increases the overlap of the final state with the ground state.

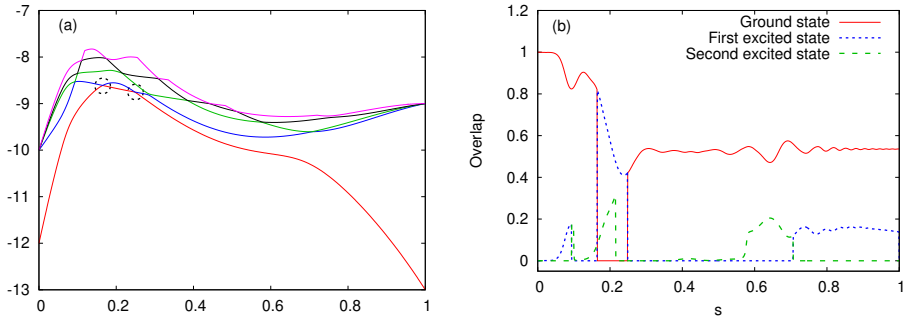


Figure 5.8.: (a) Energy spectrum of the lowest lying states represented by solid lines (the dotted circles indicate the positions of the two anticrossings between the ground state and the first excited state) and (b) the overlap of the state of the system with the instantaneous low energy states for  $T_A=100$  for a 12-variable 2-SAT problem with two comparably small anticrossings and  $g=2.0$ .

Such an evolution of the state of the system is similar to the one employed in [SNK12] for solving glued-tree problems [Chi+03]. An "almost" adiabatic evolution of the state of the system is suggested in this work, which makes use of the symmetry and gap structure of the spectrum to design a schedule that transits the state of the system from the ground state to the first excited state at the first anticrossing, and then from the first excited state to the ground state at the second anticrossing, to offer a (sub)exponential quantum speedup [AL18a].

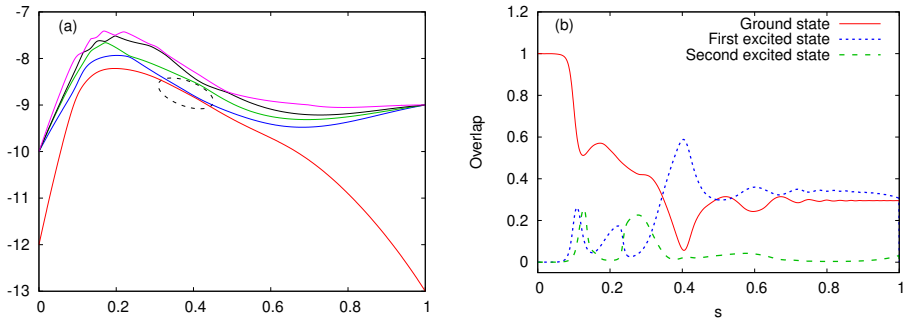


Figure 5.9.: (a) Energy spectrum of the lowest lying states: represented by solid lines (the dotted ellipse indicates the stretching of the anticrossing between the ground state and the first excited state) and (b) the overlap of the state of the system with the instantaneous low energy states for  $T_A=100$  for a 12-variable 2-SAT problem with a stretched anticrossing at  $g = 2.0$ .

- Stretching of the anticrossing: In some cases, it is also observed that adding the antiferromagnetic trigger Hamiltonian, as is the case for the problem shown in Fig. 5.9

for  $g = 2.0$ , alters the shape of the anticrossing such that it appears stretched (as indicated by the dotted ellipse in panel (a) of the figure). In this case, it is observed that the lowest two energy states stay in close proximity for a more extended range of  $s$ . According to the adiabatic theorem (Eq. (1.22)), the minimum annealing time required to ascertain an adiabatic evolution also depends on the rate of change of the Hamiltonian with respect to the annealing parameter. Adding the antiferromagnetic trigger Hamiltonian can alter this rate, and can therefore affect the final success probability. Moreover, the proximity of the ground state and the first excited state can also induce oscillations in the amplitude of the state of the system between the two levels, which can, coincidentally, lead to a higher success probability at the end of the annealing process.

## 5.2. Nonstoquastic problem Hamiltonians

For the sets of problems obtained using Eq. (5.2), we perform quantum annealing using the standard quantum annealing Hamiltonian (Eq. (1.19)), as well as the annealing Hamiltonians with ferromagnetic and antiferromagnetic trigger Hamiltonians (Eq. (5.1)).

Starting with the analysis of the minimum energy gaps using the standard quantum annealing Hamiltonian for solving the set of nonstoquastic problems, we observe that unlike the set of 2-SAT problems, in this case the number of anticrossings between the ground state and the first excited state is not necessarily 1. In the set of 1000 18-variable nonstoquastic problems, 353 problems are found to have two anticrossings, while 19 problems have three anticrossings. Another feature of difference observed in comparison to the 2-SAT problems is that the minimum energy gaps in case of the nonstoquastic problem are of  $\mathcal{O}(10)$  smaller.

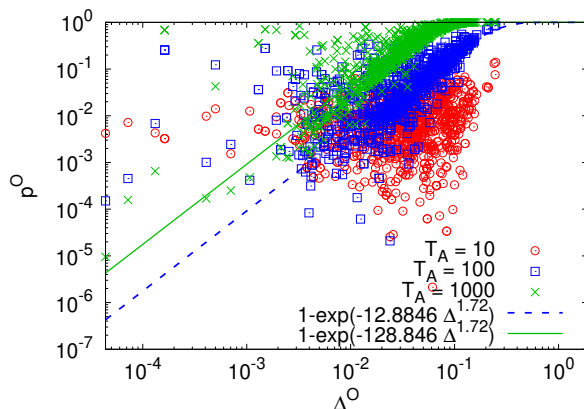


Figure 5.10.: Success probability  $p^o$  versus minimum energy gap  $\Delta^O$  for 18-variable nonstoquastic problems for various annealing times  $T_A$  for the standard quantum annealing Hamiltonian given by Eq. (1.19).

From Fig. 5.10 showing the scatter plot of the success probability obtained using the standard quantum annealing Hamiltonian (Eq. (1.19)) against the corresponding minimum energy gaps, we observe that the system still largely exhibits the Landau-Zener behavior for annealing times  $T_A = 100$  and  $T_A = 1000$ . However, due to an increase in the number of the anticrossings between the ground state and the first excited state, and a decrease in the value of the minimum energy gaps, which in turn makes the annealing time  $T_A = 10$  too short, giving way to the non-adiabatic mechanism of fast annealing, we observe more scattering of the data points in comparison to Fig. 5.1 for the problem Hamiltonian corresponding to the 2-SAT problems.

Unlike the case for the 2-SAT problems, the effects of including the ferromagnetic trigger Hamiltonian, are not as straightforward for the nonstoquastic problem Hamiltonians. In this case, the addition of the ferromagnetic trigger Hamiltonian is accompanied by an enlargement of the minimum energy gap between the ground state and the first excited state for a majority, but not all of the problems of the set. We find that the number of such cases increases with increasing the strength of the trigger Hamiltonian, and out of a set of 1000 18-variable problems, 656, 713, and 837 problems, have a larger minimum energy gaps compared to the standard quantum annealing Hamiltonian (Eq. (1.19)) for  $g = 0.5$ , 1.0, and 2.0, respectively. Furthermore, adding the ferromagnetic trigger Hamiltonian also decreases the number of anticrossings between the ground state and the first excited state of the annealing Hamiltonian. For the set of nonstoquastic problem Hamiltonians considered here, only 98, 23, and 5 problems out of the 18-variable problem set have two anticrossings upon adding the ferromagnetic trigger Hamiltonian with  $g = 0.5$ ,  $g = 1.0$ , and  $g = 2.0$ , respectively.

Table 5.3.: Number of 18-variable nonstoquastic problems with increased success probabilities after adding the ferromagnetic trigger Hamiltonian with strengths  $g$  to the Hamiltonian Eq. (1.19). The set consists of 1000 problems.

$g$	$T_A = 10$	$T_A = 100$	$T_A = 1000$
0.5	722	596	592
1.0	851	678	647
2.0	928	815	763

Moving next to a comparison between the success probabilities from the annealing Hamiltonian with the ferromagnetic trigger Hamiltonian and the standard quantum annealing Hamiltonian for solving the set of 18-variable nonstoquastic problems, Tab. 5.3 shows the number of problems with an enhanced success probability for different strengths of the trigger Hamiltonian and annealing times. We note, that a majority of problems have a larger success probability upon adding the ferromagnetic trigger Hamiltonian for all values of  $T_A$  and  $g$ . However, for a given trigger strength, the number of problems with an enhanced success probability decreases with increasing annealing time, although the values of both success probabilities are close to one. This observation is incompatible with the Landau-Zener formula, and to understand the reasons for it, we focus on the energy

## 5. Adding the trigger Hamiltonian

spectra and overlap of the state of the system of a 12-variable nonstoquastic problem with the lowest three instantaneous energy states (see Fig. 5.11).

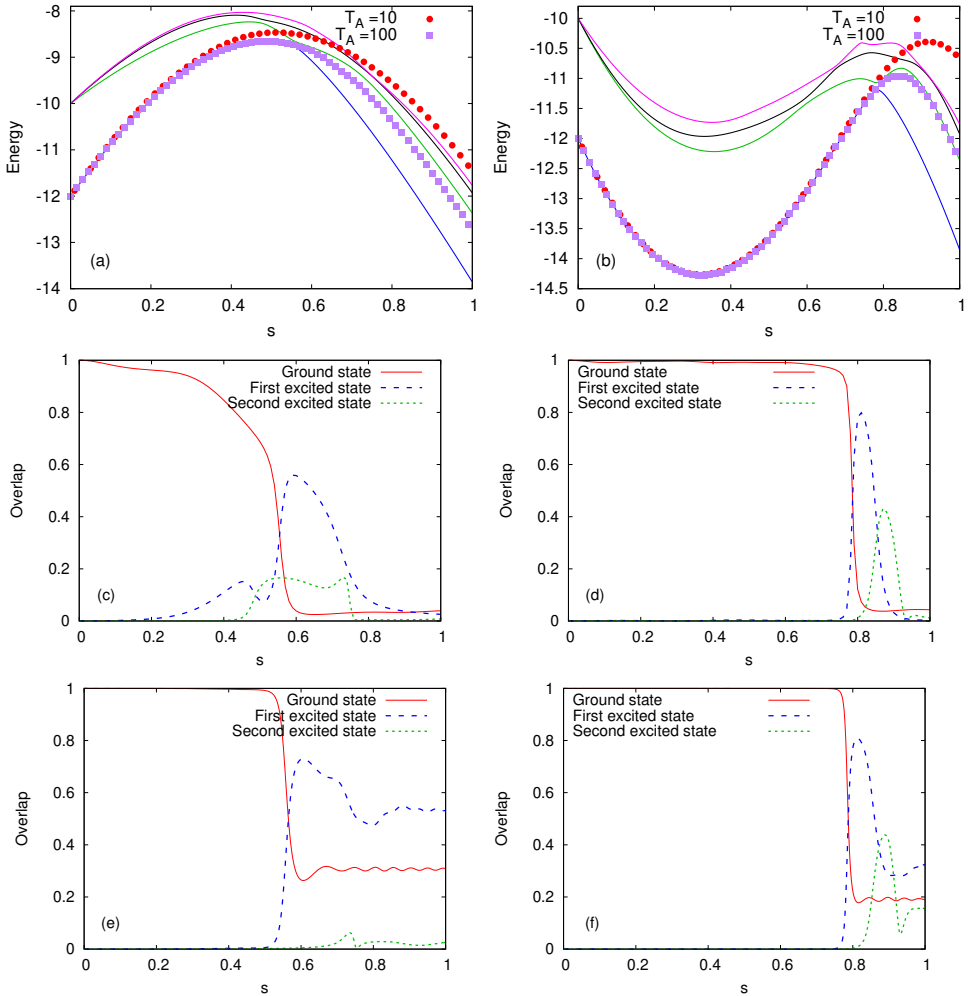


Figure 5.11.: (a), (c), (e) Energy of the lowest lying states and overlap of the ground state with the lowest three energy states for standard quantum annealing and (b), (d), (f) after adding a ferromagnetic trigger with  $g=2.0$  for a 12-variable nonstoquastic problem. The solid lines in panels (a) and (b) represent the lowest lying states while the points in panels (a) and (b) represent the average energy of the instantaneous state of the system for  $T_A=10, 100$ . The overlap is calculated for (c), (d)  $T_A=10$  and (e), (f)  $T_A=100$ .

As for the example shown in Fig. 5.11(b), the addition of the ferromagnetic trigger

Hamiltonian with  $g = 2.0$  leads to a change in the shape of the anticrossing between the ground state and the first excited state for many problems of the 18-variable set. According to the adiabatic theorem (Eq. (1.22)), the annealing time required to ascertain an adiabatic evolution depends, additionally, on the rate of change of the Hamiltonian with respect to the annealing parameter.

Considering first  $T_A = 10$ , from Fig. 5.11(c) we observe that for the standard quantum annealing Hamiltonian, the state of the system deviates from the ground state before the anticrossing between the lowest two energy levels, from where most of its amplitude is transferred to the higher energy levels. On the other hand, for the quantum annealing Hamiltonian with the ferromagnetic trigger Hamiltonian (see Fig. 5.11(d)), the amplitude from the state of the system is shifted to the first excited state only at the anticrossing, owing to a larger gap between the lowest two energy levels. Coincidentally, in this case, the final state at the end of the annealing with the ferromagnetic trigger Hamiltonian has a marginally larger overlap with the ground state of the problem Hamiltonian.

The annealing time  $T_A = 100$ , on the other hand, is long enough for the state of the system to follow the instantaneous ground state up till the anticrossing for the standard quantum annealing Hamiltonian (see Fig. 5.11(e)). The amplitude of the system state transferred to the first excited state at the anticrossing, in this case, is smaller than that for the annealing Hamiltonian with the ferromagnetic trigger Hamiltonian due to the shape of the anticrossing in the latter. This explains the reason for a decrease in the number of problems with enhanced success probabilities upon adding the trigger Hamiltonian as the annealing time increases.

Lastly, the success probability  $p^F$  versus the minimum energy gaps  $\Delta^F$  for the quantum annealing Hamiltonian with the ferromagnetic trigger for different  $T_A$  and  $g$  are shown in Fig. 5.12. Compared to the problem Hamiltonians corresponding to the 2-SAT problems (Fig. 5.3), the scatter plots for the nonstoquastic problems show much more scattering in the data, which can be attributed to an increase in the number of anticrossings between the ground state and the first excited state in the latter.

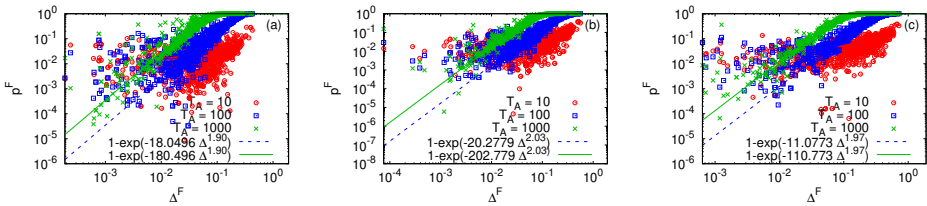


Figure 5.12.: Success probability  $p^F$  versus minimum energy gap  $\Delta^F$  for the 18-variable nonstoquastic problems after adding the ferromagnetic trigger Hamiltonian to Hamiltonian Eq. (1.19) with strengths (a)  $g=0.5$ , (b)  $g=1.0$ , (c) and  $g=2.0$  and for various annealing times  $T_A$ . The lines are fits to the data.

As the final case, we discuss the effects of adding the antiferromagnetic trigger Hamiltonian with different strengths to the annealing Hamiltonian for solving the nonstoquastic problem Hamiltonians. These effects are quite similar as those observed for the case of

the 2-SAT problems. The inclusion of the antiferromagnetic trigger Hamiltonian can either increase or decrease the minimum energy gap between the lowest two energy levels, although for the set of nonstoquastic problems a majority of the problems have a smaller gap as a result of adding the antiferromagnetic trigger. We observe that out of the 1000 problems belonging to the 18-variable set, 406, 442, and 367 problems have an enlarged minimum energy gap for  $g = 0.5$ ,  $g = 1.0$ , and  $g = 2.0$ , respectively. Furthermore, we also note an increase in the number of the anticrossings between the ground state and the first excited state as the strength of the annealing parameter increases (see Tab. 5.4).

Table 5.4.: Number of 18-variable nonstoquastic problems with different number of anticrossings,  $N_A$ , after adding the antiferromagnetic trigger Hamiltonian with strengths  $g$ , to the Hamiltonian Eq. (1.19). The set consists of 1000 problems.

$N_A$	$g = 0.5$	$g = 1.0$	$g = 2.0$
1	276	18	0
2	597	306	25
3	121	494	166
4	6	171	407
5	0	11	310
6	0	0	86
7	0	0	6

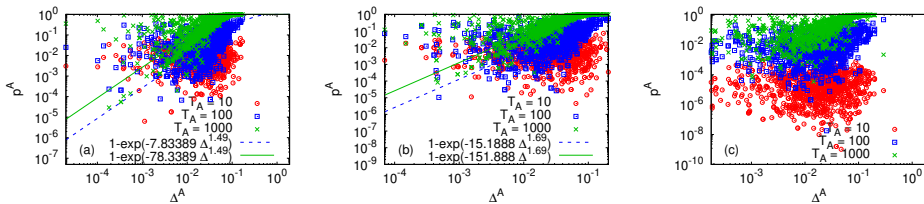


Figure 5.13.: Success probability  $p^A$  versus minimum energy gap  $\Delta^A$  for the 18-variable nonstoquastic problems after adding the antiferromagnetic trigger Hamiltonian to Hamiltonian Eq. (1.19) with strengths (a)  $g=0.5$ , (b)  $g=1.0$ , and (c)  $g=2.0$  and for various annealing times  $T_A$ . The lines are fits to the data.

Due to this increase, the success probability versus the minimum energy gap plots for the annealing Hamiltonian with the antiferromagnetic trigger for different annealing times and trigger strengths, given in Fig. 5.13, shows a larger deviation of the data points from the Landau-Zener behavior.

### 5.3. Summary

In this chapter, the focus was on expanding the scope of the quantum annealing Hamiltonians by adding an additional term to the standard quantum annealing Hamiltonian, namely, the trigger Hamiltonian. The trigger Hamiltonian was chosen such that it vanishes at the beginning and end of the annealing process. Furthermore, we employed two kinds of trigger Hamiltonians, one with ferromagnetic transverse couplings, and the other with antiferromagnetic transverse. The strength of these couplings was controlled using the strength parameter  $g = 0.5, 1, 2$ , and their graph was chosen to have the same couplings as in the problem Hamiltonian.

We found that compared to the standard quantum annealing Hamiltonian, the minimum energy gaps between the ground state and the first excited state of the annealing Hamiltonian are enlarged by the addition of the ferromagnetic trigger Hamiltonian, for a majority of the problems. This enlargement was observed to increase with increasing the strength of the trigger Hamiltonian, which led to an enhancement in the resulting success probability for a majority of the 2-SAT and nonstoquastic problems studied.

On the other hand, the addition of the antiferromagnetic trigger Hamiltonian to the standard quantum annealing Hamiltonian can affect the energy spectrum vastly. It can lead to an increase in the number of anticrossings between the ground state and the first excited state, or change in the shape of the anticrossing. Adding the antiferromagnetic trigger Hamiltonian could either increase or decrease the minimum energy gap between the ground state and first excited state. Furthermore, the inclusion of the antiferromagnetic trigger Hamiltonian can induce non-adiabatic mechanisms which could prove to be beneficial for the success probability of the quantum annealing process. Such mechanisms include fast annealing, or the presence of an even number of comparably small anticrossings.

Thus, we found that the addition of the ferromagnetic trigger Hamiltonian improved the performance of quantum annealing in a systematic manner by enlarging the minimum energy gaps of the annealing Hamiltonian more for larger values of the trigger strength in all the cases of the 2-SAT problems studied. We also found that the improvement in the success probability ( $p^F/p^O$ ) was of the order  $\mathcal{O}(10^2)$  for a majority of the problems with  $g = 1.0, 2.0$  and  $T_A = 100$  and  $1000$ , while the largest relative success probability was close to  $\mathcal{O}(10^6)$ . Though the enhancement in the success probability was not observed to be as probable for the annealing Hamiltonian with the antiferromagnetic trigger for the 2-SAT problems, the largest relative success probability was still  $\mathcal{O}(10^4)$ . It is worth mentioning that the conclusions drawn here are different from those in [Hor+17] where the antiferromagnetic trigger Hamiltonian was found to deliver the largest improvement in the relative success probability for solving spin-glass problems with up to 17 variables. We found that the underlying mechanisms resulting in an improvement were very different for the quantum annealing Hamiltonian with the antiferromagnetic trigger since they mostly relied on a non-adiabatic evolution of the state of the system. Thus, both kinds of trigger Hamiltonians considered in this work were found to be useful for solving 2-SAT problems under different circumstances as they are beneficial in different regimes.



## 6. Scaling and distribution of quantifiers of quantum annealing

As quantum annealing was originally developed as an optimization algorithm, there has been an active interest in gauging its efficiency for solving various optimization problems, ever since its conception [Bro+99; San+02; MST04; ST08; SN12a; SNK12; Sus+18; AL18a; Hsu+19; Hau+20; CL21]. To this end, numerous investigations have been conducted in the hopes of finding a speedup of quantum annealing over the existing classical algorithms [SN12a; Røn+14; AL18b]. An active direction of research has also been the study of the scaling behavior of quantum annealing as a function of the size of the problem for different optimization problems [Boi+14; Røn+14; Kin+15; Hen+15; Neu14b; AL18b; Wil+21; Kön+21; Meh+22a].

In this chapter, we study the distributions of the minimum energy gap between the ground state and the first excited state of the annealing Hamiltonian, and the success probability of quantum annealing for solving the sets of 2-SAT problems, corresponding to different problem sizes. Subsequently, we focus on the scaling complexity of quantum annealing, where we study the scaling of minimum energy gaps, and TTS99 (time to solution), which is the run-time required to obtain the ground state of the problem Hamiltonian, at least once, with 99% certainty in multiple runs of the annealing algorithm. We use both simulations and the D-Wave quantum annealers for solving these problems, and compare their performances.

In order to examine the effects of introducing modifications to the standard quantum annealing Hamiltonian on its performance, we also study the distributions and/or the scaling of the three quantifiers listed above upon the addition of the trigger Hamiltonian to the annealing Hamiltonian using simulations. For this, we use both the ferromagnetic and the antiferromagnetic trigger Hamiltonians described in the previous chapter (Chapter 5) with strength  $g = 1$ .

### 6.1. Analysis criteria

For analyzing the distributions and determining the scaling complexity, we again make use of the hard 2-SAT problems, with the number of variables  $N$  varying from 6 to 18. The problem sets with  $N \leq 9$  have 100 problems each, while the larger sets have 1000 problems. However, we note that in every set, some problems have exactly the same connectivity graph and biases, although different labels for the involved variables. Such redundant problems are removed from every set. The resulting sets have more than 70 problems each for  $N \leq 9$ , and more than 900 problems for  $10 \leq N \leq 18$  except for the sets with  $N = 15$  and 18, which have 557 and 789 problems, respectively.

As in the previous chapter, we use the Lanczos algorithm to determine the minimum energy gaps, and the second-order Suzuki-Trotter product formula algorithm to implement the dynamics of quantum annealing. In addition to this, we use two generations of quantum annealers, DW\_2000Q\_6 (DW2000Q) and Advantage\_system1.1 (DWAdv) for solving the 2-SAT problems.

In the following subsections, we briefly discuss the three observables considered in this work for assessing the complexity of the quantum annealing algorithm for solving the given 2-SAT problems.

### 6.1.1. Minimum energy gap

According to the Landau-Zener formula (Eq. (1.24)), the minimum energy gap between the ground state and the first excited state of the annealing Hamiltonian is a crucial factor for determining the success probability of the quantum annealing algorithm. Here, we study the distribution of the minimum energy gaps for sets of 2-SAT problems corresponding to fixed sizes, as well as the scaling of the minimum energy gaps as a function of the system size. The distribution functions used as fits for the minimum energy gap distributions are given in Appendix G.

For determining the scaling complexity of the minimum energy gaps as a function of the size of the system, we calculate and plot the deciles of the minimum energy gaps for the standard quantum annealing Hamiltonian, as well as for the Hamiltonian with ferromagnetic and antiferromagnetic trigger Hamiltonians, all as a function of the problem size. The scaling is then obtained by fitting appropriate functions to these deciles.

For sufficiently long annealing times, where the Landau-Zener theory holds (Eq. (1.24)), the scaling behavior of the minimum energy gaps can be employed to obtain an estimate of the scaling behavior of the annealing time required for an adiabatic evolution of the state of the system. Defining, the correlation length  $\xi = 1/\Delta_{min}$ , according to the Landau-Zener theory

$$T_A \propto \xi^2, \tag{6.1}$$

which suggests that if the correlation length increases exponentially, the annealing time required to ascertain an adiabatic evolution of the state of the system also grows exponentially, with an exponent twice as large.

### 6.1.2. Success probability

The next observable is the dynamic quantifier of quantum annealing, the success probability, which is the probability of obtaining the ground state of the problem Hamiltonian. It is determined by calculating the overlap of the final state obtained at the end of the annealing process with the known ground state of the problem Hamiltonian. We study the distribution of the success probability for problem sets with fixed size, using both simulations and the D-Wave systems DW2000Q and DWAdv. While DW2000Q uses the Chimera qubit topology, the more recent DWAdv uses the more connected Pegasus topology. Since in the Pegasus topology, each qubit has a connectivity degree of 15, while

for the Chimera topology it is 6, a majority of the problems from each set could be directly embedded in DWAdv, whereas, approximately, only half of them could find a direct embedding on DW2000Q.

For the simulations of the dynamics of quantum annealing, we choose the annealing times  $T_A = 10, 100, 1000$ , and use the Hamiltonian Eq. (1.19) and Eq. (5.1) with ferromagnetic and antiferromagnetic trigger Hamiltonian with  $g = 1$ . As seen in Chapter 5, for the set of problems with  $N = 18$ , the annealing time  $T_A = 1000$  is sufficiently long to ensure an almost adiabatic evolution of the state of the system for a majority of the problems. On the contrary, the annealing time  $T_A = 10$  is generally too small for the success probability to follow the Landau-Zener formula, and the non-adiabatic mechanisms (see section 5.1.3) are dominant in this regime. It is therefore interesting to see how the non-adiabatic mechanisms affect the success probability. Lastly,  $T_A = 100$  is the intermediate time between the two regimes, which can be sufficiently long for the easy problems of the set but for the hard problems, i.e., the problems with a small minimum energy gap, the state of the system can still evolve non-adiabatically. Using the D-Wave energy scale, the annealing times  $T_A = 10, 100, 1000$  roughly correspond to annealing times 0.5 ns, 5 ns, and 50 ns, respectively. However, on the D-Wave systems, we use much longer annealing times,  $T_A = 4, 20, 100 \mu\text{s}$ .

To plot the success probability distributions, we map the raw success probabilities  $p$  obtained from the simulations and the D-Wave systems such that the average mapped success probability of the whole set is  $1/2$ , i.e.,  $\langle P_{succ} \rangle = 1/2$ , where

$$P_{succ} = 1 - (1 - p)^R, \quad (6.2)$$

and  $R$  is the number of repetitions (or equivalently, a scaling factor for the annealing time), determined using the whole set of problems, that shifts the average success probability of the set to 0.5.

In the long annealing time limit, it is possible to find a mapping between the minimum energy gap and the success probability using the Landau-Zener formula (Eq. (1.24)). Since,

$$p = 1 - e^{-\gamma \Delta_{min}^2}, \quad (6.3)$$

where  $\gamma$  controls the speed of sweep, which is in turn controlled by the annealing time, and therefore,

$$\Delta_{min} = \gamma^{-1/2} \{-\ln(1 - p)\}^{1/2}. \quad (6.4)$$

The Jacobian  $\|\partial \Delta_{min} / \partial p\|$  is given by

$$\|\partial \Delta_{min} / \partial p\| = \frac{1}{2} \gamma^{-1} \frac{1}{\Delta_{min}} e^{\gamma \Delta_{min}^2}. \quad (6.5)$$

Hence, the distribution of the success probability can be determined up to the normalization constant  $C^{-1}$  if the probability distribution function for the minimum energy gaps  $PDF(\Delta_{min})$  is known [Neu14b], since

$$PDF(p) dp = C^{-1} PDF(\Delta_{min}) \gamma^{-1} \frac{1}{\Delta_{min}} e^{\gamma \Delta_{min}^2} dp. \quad (6.6)$$

For example, for a minimum energy gaps distribution following the Weibull distribution function with  $k = 2$  (Eq. (G.2)), i.e.,

$$PDF(\Delta_{min}) = a \left( \frac{\Delta_{min}}{b} \right) e^{-\left( \frac{\Delta_{min}}{b} \right)^2}, \quad (6.7)$$

with parameter  $b$  and normalization constant  $a$ , substituting  $PDF(\Delta_{min})$  in Eq. (6.6), and setting the parameter  $\gamma = 1/b^2$ , we obtain  $PDF(P_{succ}) dP_{succ} = ab/C dP_{succ}$ , a flat distribution.

Similarly, it is possible to obtain unimodal or bimodal distributions for the success probability distribution  $PDF(P_{success})$  if one tunes the annealing time by means of  $\gamma$  to the point where  $\langle P_{succ} \rangle = 1/2$ , depending on the distribution functions that the minimum energy gaps follow.

### 6.1.3. Time to solution

Another metric considered for gauging the performance of the quantum annealing algorithm for solving an optimization problem is the time to solution (TTS), which is defined as the run-time required to obtain the ground state of the problem Hamiltonian at least once in multiple repeated runs of the algorithm with a certain probability. Mathematically,

$$TTS = \frac{\ln(1 - P_{target})}{\ln(1 - p)} T_A, \quad (6.8)$$

where  $P_{target}$  is the probability for which the correct solution is obtained at least once, and  $p$  is the success probability obtained with a given  $T_A$ . For what follows, we fix  $P_{target} = 0.99$ , and label the corresponding run-time as  $TTS99$ .

To evaluate the performance of quantum annealing using this metric, we plot deciles for  $TTS99$  as a function of the system size, for the success probabilities obtained from the simulations and the two D-Wave systems. The scaling of  $TTS99$  is then obtained by fitting appropriate functions to the resulting deciles. To allow for a fair comparison between the scaling behaviors obtained from the simulations and the D-Wave systems, we omit the problems for which the D-Wave software could not find a direct embedding on the system.

When the annealing time is sufficiently long to allow for an adiabatic evolution of the state of the system, the scaling behavior of  $TTS99$  is expected to be similar to that of the theoretical estimate of the run-time (Eq. (6.1)) obtained using the scaling of the minimum energy gaps. However, this need not be the case for short annealing times, where various non-adiabatic mechanisms play a significant role in determining the success probability and its scaling, and which are not taken in to account by the Landau-Zener formula. Thus, a comparison between the scaling behavior of  $TTS99$  and the theoretical run-time can provide an insight into the adiabaticity of the evolution.

## 6.2. Numerical results

After having discussed the three quantifiers to be used here for assessing the performance of quantum annealing for solving sets of hard 2-SAT problems, we move on to discuss the numerically obtained results first.

### 6.2.1. Minimum energy gaps

We start with the analysis of the static quantifier, the minimum energy gap, for the three quantum annealing Hamiltonians given by Eq. (1.19) and Eq. (5.1) with ferromagnetic and antiferromagnetic trigger Hamiltonians. We focus on the minimum energy gap distributions obtained from the simulations.

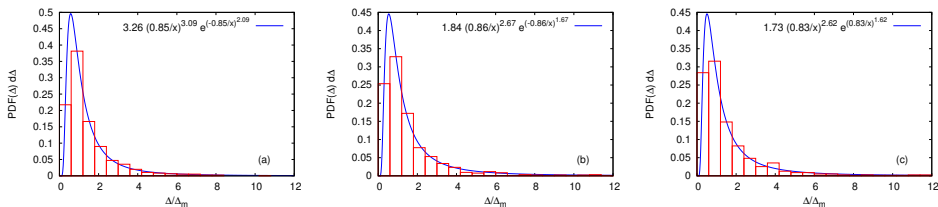


Figure 6.1.: Median-normalized minimum energy gap distributions  $PDF(x)dx$  for the standard quantum annealing Hamiltonian given by Eq. (1.19), for sets with (a)  $N = 16$ , (b)  $N = 17$ , and (c)  $N = 18$ , where  $x = \Delta/\Delta_m$  and  $\Delta_m$  is the median minimum energy gap of the set.

Figure 6.1 shows the median-normalized minimum energy gap distribution for the standard quantum annealing Hamiltonian given by Eq. (1.19) for sets of problems with  $N = 16$ , 17, and 18. The Fréchet functions given in Appendix (Eq. (G.1)) match the obtained distributions. It is also observed that the parameter  $k$  in the fit approaches 1 as the size of the problems increases.

One of the main consequences of adding the ferromagnetic trigger Hamiltonian to the annealing Hamiltonian (Eq. (5.1)) is the enlargement of the minimum energy gaps for all the problems of the set, as has been discussed in section 5.1.2. Similar observations have also been reported in [Hor+17]. Therefore, the median-normalized minimum energy gap distribution for the annealing Hamiltonian with the ferromagnetic trigger Hamiltonian, shown in Fig. 6.2, is significantly different from that for the standard annealing Hamiltonian (Fig. 6.1), and appears more like a normal distribution.

The fits to the distribution in this case are obtained by using translated-Weibull functions to the median-normalized distribution for the correlation length  $\xi = 1/\Delta_{min}$ . The extent of translation in this case, i.e.,  $\mu$  according to Eq. (G.3), represents the increase in the minimum energy gaps as a result of adding the ferromagnetic trigger Hamiltonian. Fixing parameters  $\mu$ ,  $b$ , and  $k$  obtained from the fits for the correlation length, we fit the transformed-translated-Weibull function (Eq. (G.4)) to the median-normalized minimum energy gap distribution via a parameter  $a$ . The obtained fits match the form of the

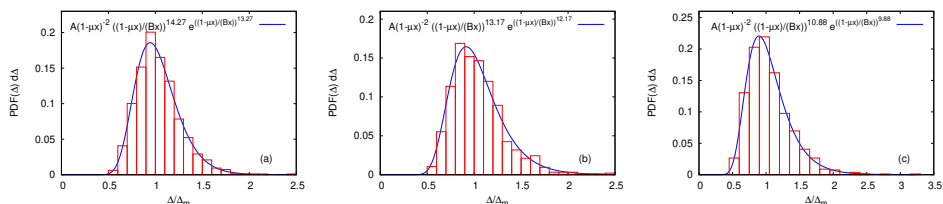


Figure 6.2.: Median-normalized minimum energy gap distributions  $PDF(x)dx$  for the annealing Hamiltonian given by Eq. (5.1) with the ferromagnetic trigger Hamiltonian, for sets with (a)  $N = 16$  ( $A = 6.9 \times 10^4$ ,  $\mu = 0.20$ ,  $B = 0.82$ ), (b)  $N = 17$  ( $A = 2.5 \times 10^4$ ,  $\mu = 0.10$ ,  $B = 0.93$ ), and (c)  $N = 18$  ( $A = 3410.0$ ,  $\mu = 0.10$ ,  $B = 0.94$ ), where  $x = \Delta/\Delta_m$  and  $\Delta_m$  is the median minimum energy gap of the set.

distributions well.

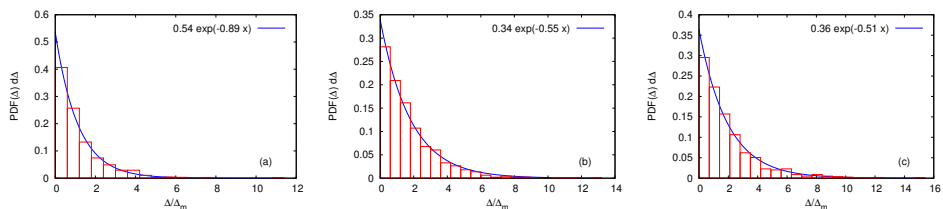


Figure 6.3.: Median-normalized minimum energy gap distributions  $PDF(x)dx$  for the annealing Hamiltonian given by Eq. (5.1) with the antiferromagnetic trigger Hamiltonian, for sets with (a)  $N = 16$ , (b)  $N = 17$ , and (c)  $N = 18$ , where  $x = \Delta/\Delta_m$  and  $\Delta_m$  is the median minimum energy gap of the set.

The median-normalized minimum energy gap distribution for the annealing Hamiltonian with the antiferromagnetic trigger Hamiltonian (Eq. (5.1)), shown in Fig. 6.3, follows exponentially decaying functions, which are equivalent to the Weibull function with  $k = 1$  (Eq. (G.2)).

Thus, we obtain three distinct minimum-energy-gap distributions for the annealing Hamiltonians considered in this work, and therefore, we may anticipate to find differences in the corresponding success probability distributions.

The second important aspect of the minimum energy gaps in the context of the performance of quantum annealing is their scaling as a function of the problem size. Figure 6.4 shows the odd deciles for the minimum energy gaps for the three annealing Hamiltonians considered in this work, as a function of the number of variables in the problem, with  $6 \leq N \leq 18$ .

For all three Hamiltonians, we find the minimum energy gaps to be scaling exponentially with the size of the problem. We therefore fit the exponential functions of the form  $\Delta_{min} = De^{-r\Delta^N}$  to the deciles for  $N \geq 15$  for the Hamiltonian Eq. (1.19) and Eq. (5.1)

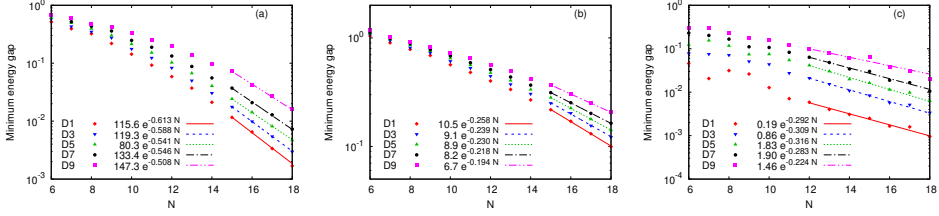


Figure 6.4.: Deciles for the minimum energy gaps for the annealing Hamiltonians given by (a) Eq. (1.19), (b) Eq. (5.1) with the ferromagnetic trigger Hamiltonian, and (c) Eq. (5.1) with the antiferromagnetic trigger Hamiltonian.

with the ferromagnetic trigger Hamiltonian, and for  $N \geq 12$  for the Hamiltonian Eq. (5.1) with the antiferromagnetic trigger Hamiltonian. For the standard quantum annealing Hamiltonian, we find the median minimum energy gap (given by the fifth decile  $D5$ ) to be scaling with an exponent  $r_\Delta = 0.541$ . According to Eq. (6.1), the run-time required to ascertain an adiabatic evolution of the state of the system for the given set of problems should also increase exponentially with an exponent  $r_{TR} = 2r_\Delta$ , i.e.,  $r_{TR} = 1.082$ , where  $T_A = De^{r_{TR}N}$  is the theoretical run-time. This scaling behavior is worse compared to even the scaling of the brute-force search of the ground state of the problem Hamiltonian, which scales as  $2^N$  (corresponding to a scaling exponent of 0.693). On the other hand, although these problems have been designed to be difficult to be solved using simulated annealing, and the resulting scaling for the run-time is exponential in the size of the problems, the scaling exponent  $r_{SA}$  is much smaller ( $r_{SA} = 0.34$ ). Thus, the standard quantum annealing Hamiltonian given by Eq. (1.19) is unsuitable for solving the given set of problems.

The addition of the trigger Hamiltonians, on the other hand, improves the scaling of the minimum energy gaps significantly, especially for the ferromagnetic trigger Hamiltonian. In this case, the median minimum energy gap scales with an exponent  $r_\Delta = 0.230$ , and thus the theoretical run-time for ensuring an adiabatic evolution of the state of the system grows with a scaling exponent of  $r_{TR} = 0.460$ , which is not only better compared to the scaling exponent of the theoretical run-time for the standard quantum annealing Hamiltonian (Eq. (1.19)), but also better compared to the scaling of the brute-force search of the ground state. Similarly, for the annealing Hamiltonian given by Eq. (5.1) with the antiferromagnetic trigger Hamiltonian,  $r_\Delta = 0.316$ , and therefore  $r_{TR} = 0.632$ , which is smaller than the scaling exponent of the run-time for the standard quantum annealing Hamiltonian, as well as than that for the brute-force search.

### 6.2.2. Success probability

Focusing next on the dynamic quantifier, i.e., the success probability, Fig. 6.5 shows the mapped success probability distribution (using Eq. (6.2)) obtained from the standard quantum annealing Hamiltonian (Eq. (1.19)) for  $T_A = 10, 100, 1000$  and problem sets corresponding to  $N = 17$  and  $N = 18$ . We observe that for both problem sets, the mapped success probability distributions for all the three annealing times is bimodal. Bimodality

of the success probability distribution has also been noted in previous work [Boi+14], using simulated quantum annealing and the D-Wave One system for solving spin glass problems.

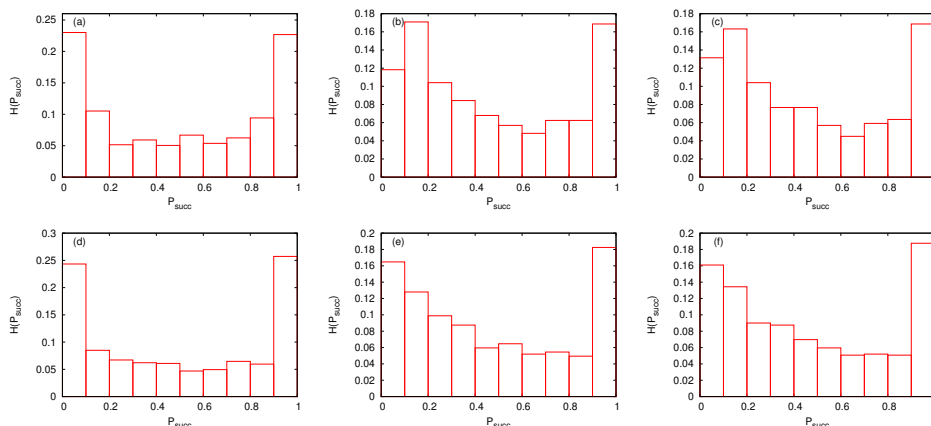


Figure 6.5.: Success probability distributions using the standard quantum annealing Hamiltonian given by Eq. (1.19) for (a), (b), (c)  $N = 17$ , and (d), (e), (f)  $N = 18$  for (a), (d)  $T_A = 10$ , (b), (e)  $T_A = 100$ , and (c), (f)  $T_A = 1000$ .

Adding the ferromagnetic trigger Hamiltonian to the standard quantum annealing Hamiltonian, however, yields quite distinct results for the success probability distribution. As shown in Fig. 6.6, in this case the distribution is unimodal, which on the contrary, is also the case if one uses simulated annealing for solving spin glass problems, see [Boi+14].

Lastly, in Fig. 6.7, we show the mapped success probability distribution obtained from the annealing Hamiltonian given by Eq. (5.1) with the antiferromagnetic trigger Hamiltonian for  $T_A = 10, 100, 1000$ , corresponding to problem sets  $N = 17$  and  $N = 18$ . We observe two kinds of distributions in this case. The first is the constant distribution observed for the short annealing time  $T_A = 10$ , while the other is the bimodal distribution obtained for longer annealing times  $T_A = 100$  and  $1000$ . Although, as shown in section 6.1.2, it is possible to theoretically obtain a constant success probability distribution for certain distributions of the minimum energy gap, the case at hand is not one such instance, the reason being that the annealing time  $T_A = 10$  is not sufficient for the system to be approximated as a two-level system and the Landau-Zener formula cannot be employed. Moreover, the addition of the antiferromagnetic trigger Hamiltonian to the standard annealing Hamiltonian changes the energy spectrum in ways that bolster certain non-adiabatic mechanisms to favor the success probability (section 5.1.3). This has also been observed in [Cro+14; Hor+17]. Thus, we obtain three distinct success probability distributions, unimodal, bimodal and constant.

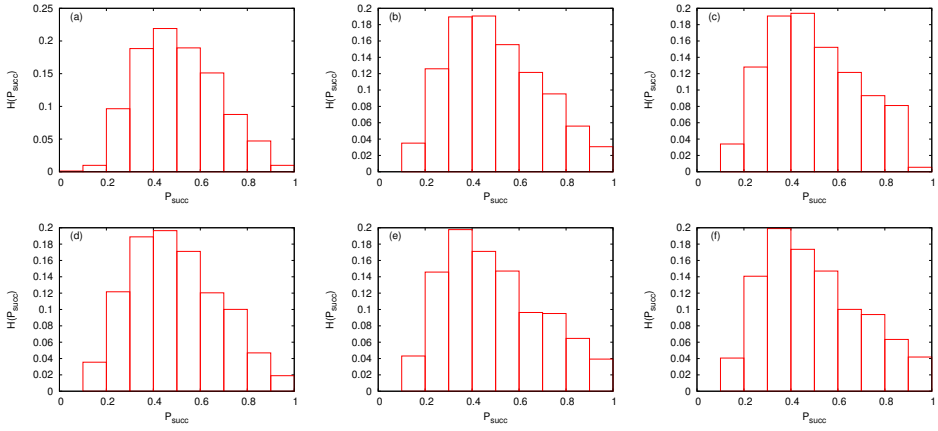


Figure 6.6.: Success probability distributions using the quantum annealing Hamiltonian given by Eq. (5.1) with the ferromagnetic trigger Hamiltonian for (a), (b), (c)  $N = 17$ , and (d), (e), (f)  $N = 18$  for (a), (d)  $T_A = 10$ , (b), (e)  $T_A = 100$ , and (c), (f)  $T_A = 1000$ .

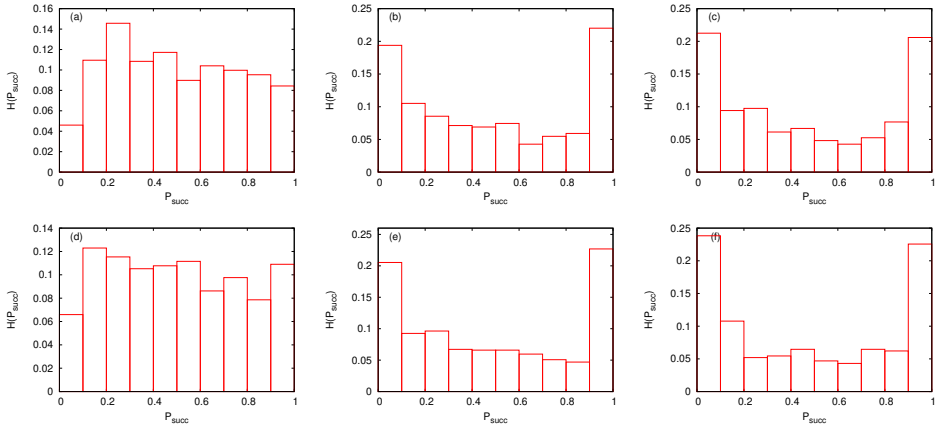


Figure 6.7.: Success probability distributions using the quantum annealing Hamiltonian given by Eq. (5.1) with the antiferromagnetic trigger Hamiltonian for (a), (b), (c)  $N = 17$ , and (d), (e), (f)  $N = 18$  for (a), (d)  $T_A = 10$ , (b), (e)  $T_A = 100$ , and (c), (f)  $T_A = 1000$ .

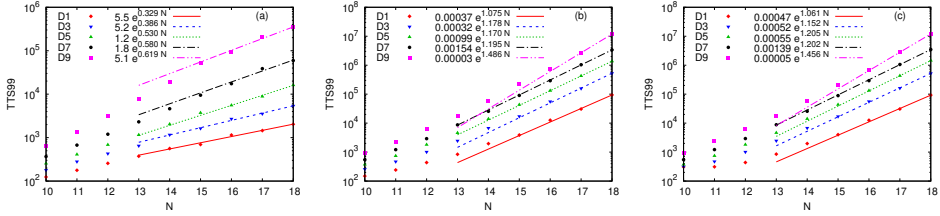


Figure 6.8.: Deciles for TTS99 for the annealing Hamiltonian given by Eq. (1.19) for (a)  $T_A = 10$ , (b)  $T_A = 100$ , and (c)  $T_A = 1000$ .

### 6.2.3. TTS99

In this section, we discuss the results for the third quantifier for the simulations of quantum annealing, which is TTS99. Starting with the scaling of TTS99 obtained using the success probabilities for the standard quantum annealing Hamiltonian (Eq. (1.19)), from Fig. 6.8 we observe an exponential scaling of all the deciles as a function of the system size for the three annealing times, as expected from the scaling of the minimum energy gap for this case. Furthermore, the median TTS99 scales with an exponent of  $r_{TTS99} = 1.170$  and  $r_{TTS99} = 1.205$  for  $T_A = 100$  and  $T_A = 1000$ , respectively, where  $TTS99 = De^{r_{TTS99}N}$ . These exponents deviate slightly from the theoretical scaling exponent  $r_{TR} = 1.082$  predicted using the scaling of the minimum energy gaps. This is due to the difference between the exponent  $b$  for the minimum energy gap obtained (see Section 5.1.1) by plotting the success probability as a function of the minimum energy gap (see Fig. 5.1) and the value of two obtained from the Landau-Zener formula. Upon using the exponent  $b = 2.19$  obtained in Section 5.1.1, we obtain  $r_{TR} = 1.18$ , which is closer to the exponents  $r_{TTS99}$  for  $T_A = 100, 1000$ . However, in case of  $T_A = 10$ , we find  $r_{TTS99} = 0.530$  which is significantly smaller to  $r_{TR}$ , and also smaller than the scaling exponent for the brute-force search.

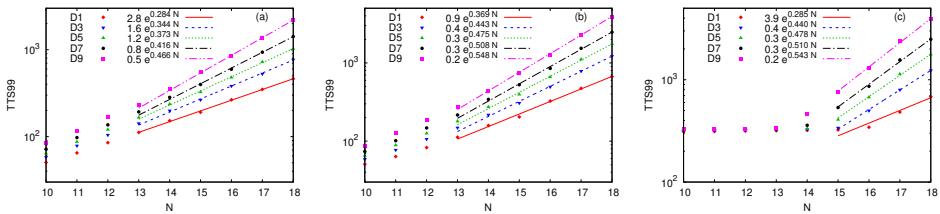


Figure 6.9.: Deciles for TTS99 for the annealing Hamiltonian given by Eq. (5.1) with the ferromagnetic trigger Hamiltonian for (a)  $T_A = 10$ , (b)  $T_A = 100$ , and (c)  $T_A = 1000$ .

A similar trend is also observed for the annealing Hamiltonian given by Eq. (5.1) with the ferromagnetic trigger Hamiltonian (shown in Fig. 6.9) where median TTS99 scales with  $r_{TTS99} = 0.373$  for  $T_A = 10$ , and the antiferromagnetic trigger Hamiltonian (shown in Fig. 6.10) where median TTS99 scales with  $r_{TTS99} = 0.277$  for  $T_A = 10$ . This behavior can

be explained on the basis of the non-adiabatic mechanisms which are dominant for short annealing times such as  $T_A = 10$ , and can favor the success probability and hence the scaling of  $TTS99$ . Since the addition of the antiferromagnetic trigger results in changing the energy spectra of the annealing Hamiltonian in ways that facilitate a non-adiabatic evolution of the state of the system, for a short annealing time, the resulting scaling exponent is the smallest when the antiferromagnetic trigger is added to the Hamiltonian Eq. (5.1). On the other hand, for long annealing times, where the evolution of the system state is mostly adiabatic, the addition of the ferromagnetic trigger yields the smallest scaling exponent of  $r_{TTS99} = 0.478$ . Thus, we observe significant improvements in the scaling behavior of the quantum annealing algorithm with the inclusion of the trigger Hamiltonian for the given set of hard 2-SAT problems.

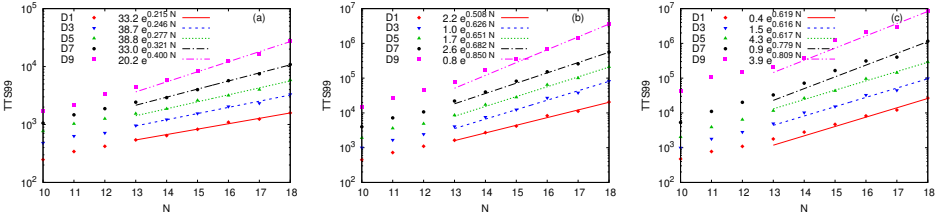


Figure 6.10.: Deciles for  $TTS99$  for the annealing Hamiltonian given by Eq. (5.1) with the antiferromagnetic trigger Hamiltonian for (a)  $T_A = 10$ , (b)  $T_A = 100$ , and (c)  $T_A = 1000$ .

## 6.3. D-Wave results

In this section, we perform a similar analysis as the one above with data obtained by using two different D-Wave systems, and compare the results with those obtained by numerical experiments.

### 6.3.1. Success probability

We begin with the distributions for the success probability obtained using the D-Wave annealers DW2000Q and DWAdv for solving sets of problems with  $N = 17$  and  $N = 18$  for annealing times  $T_A = 4, 20, 100 \mu s$ . As in the case of the simulations, the raw success probabilities are mapped such that  $\langle P_{succ} \rangle = 1/2$  using Eq. (6.2). Figure 6.11 shows the mapped success probability distribution obtained with the DW2000Q annealer. We observe that like the success probability distributions obtained numerically using the standard quantum annealing Hamiltonian given by Eq. (1.19), the distributions obtained using DW2000Q are also bimodal for the three annealing times chosen.

The success probability distributions obtained with the DWAdv system, shown in Fig. 6.12, are significantly different. Just like the constant success probability distribution obtained numerically using the quantum annealing Hamiltonian given by Eq. (5.1)

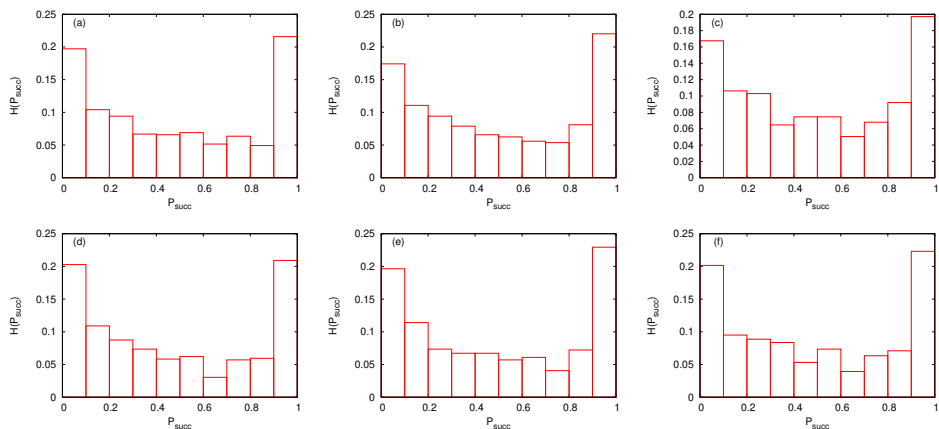


Figure 6.11.: Success probability distributions obtained using a DW2000Q system for (a), (b), (c)  $N = 17$ , and (d), (e), (f)  $N = 18$  for (a), (d)  $T_A = 4 \mu\text{s}$ , (b), (e)  $T_A = 20 \mu\text{s}$ , and (c), (f)  $T_A = 100 \mu\text{s}$ .

with the antiferromagnetic trigger Hamiltonian for  $T_A = 10$ , and the unimodal success probability distribution obtained using the ferromagnetic trigger Hamiltonian, the resulting success probabilities obtained with DWAdv are constant and unimodal. However, it should be noted that the D-Wave systems can only implement the standard quantum annealing Hamiltonian given by Eq. (1.19). The different success probability distributions in this case are an indicator of imperfections in the systems and hint towards the presence of noise and temperature effects. Nevertheless, as for the simulations, we obtain the three distinct success probability distributions using the D-Wave systems as well.

### 6.3.2. TTS99

In this section, we discuss the scaling behavior of  $TTS99$  calculated using the success probabilities resulting from the D-Wave systems DW2000Q and DWAdv. Figure 6.13 shows the odd deciles for  $TTS99$  obtained from DW2000Q for sets of problems with  $10 \leq N \leq 18$ . Recall that problems which did not allow for a direct mapping on the D-Wave system have been omitted.

As in the case of our numerical experiments, we find an exponentially increasing  $TTS99$  as the size of the system grows. However, despite the much longer annealing times compared to those used in the simulations, the scaling exponent in this case is significantly smaller than the exponent  $r_{TR}$  estimated theoretically from the scaling of the minimum energy gaps of the given problems, as well as from the numerically obtained values of  $r_{TTS99}$  for the standard quantum annealing Hamiltonian for long annealing times. Using DW2000Q for  $T_A = 4, 20, 100 \mu\text{s}$ , the median  $TTS99$  scales with exponents 0.674, 0.511, and 0.546, respectively, which is comparable to the scaling exponent of the median  $TTS99$  for the simulations of the standard quantum annealing Hamiltonian for  $T_A = 10$ , i.e., in the

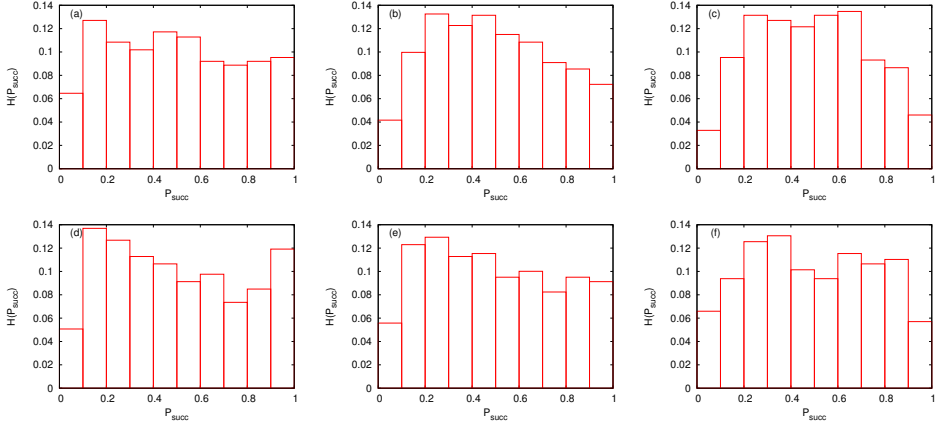


Figure 6.12.: Success probability distributions obtained using DWAdv system for (a), (b), (c)  $N = 17$ , and (d), (e), (f)  $N = 18$  for (a), (d)  $T_A = 4 \mu\text{s}$ , (b), (e)  $T_A = 20 \mu\text{s}$ , and (c), (f)  $T_A = 100 \mu\text{s}$ .

regime where the non-adiabatic mechanisms are dominant and can prove to be favorable for the success probability. Such a behavior is also suggestive of noise and temperature effects being dominant in the system.

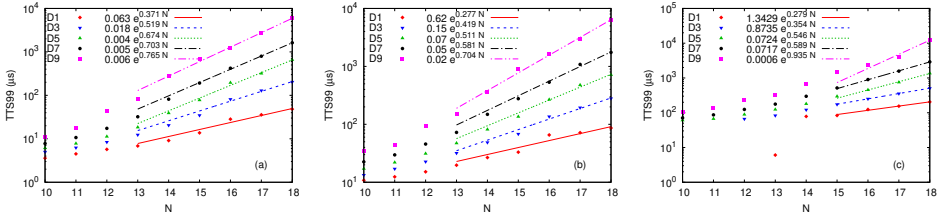


Figure 6.13.: Deciles for TTS99 obtained using DW2000Q for (a)  $T_A = 4 \mu\text{s}$ , (b)  $T_A = 20 \mu\text{s}$ , and (c)  $T_A = 100 \mu\text{s}$ .

The scaling exponents of  $TTS99$  obtained from DWAdv, as shown in Fig. 6.14, are even smaller than those obtained from DW2000Q. In this case, the median  $TTS99$  scales with an exponent of 0.393, 0.325, and 0.302 for  $T_A = 4, 20, 100 \mu\text{s}$ , respectively. Such scaling exponents are numerically obtained for short annealing times, e.g.,  $T_A = 10$  for the annealing Hamiltonian given by Eq. (5.1) with the ferromagnetic and the antiferromagnetic trigger Hamiltonian. Not only are these values better than the theoretical estimate of the scaling exponent  $r_{TR}$  for the annealing time required to keep the evolution of the state of the system adiabatic, but also significantly better than the scaling of the brute-force search of the ground state. Furthermore, for long annealing times  $T_A = 20, 100 \mu\text{s}$ , the scaling exponent is also slightly better than that for simulated annealing for solving these sets of problems.

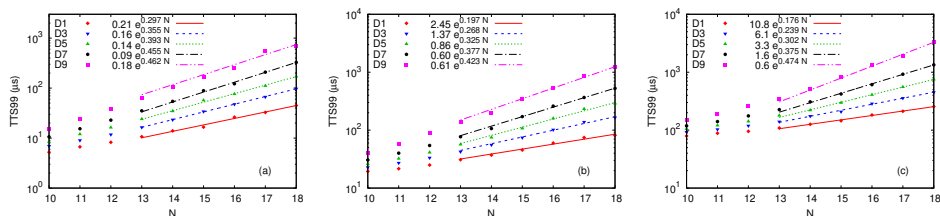


Figure 6.14.: Deciles for  $TTS99$  obtained using DWAdv for (a)  $T_A=4 \mu\text{s}$ , (b)  $T_A=20 \mu\text{s}$ , and (c)  $T_A=100 \mu\text{s}$ .

## 6.4. Summary

In this chapter, we assessed the suitability of the standard quantum annealing Hamiltonian, as well as the annealing Hamiltonians with the addition of the ferromagnetic and the antiferromagnetic trigger Hamiltonian, for solving sets of hard 2-SAT problems. We analyzed the performance of quantum annealing with the help of three metrics: the minimum energy gap between the ground state and the first excited state of the annealing Hamiltonian, the success probability of the algorithm, and the time to solution.

We found three different kinds of distributions for the minimum energy gaps, each corresponding to one of the three annealing Hamiltonians considered in this work. While the median-normalized minimum energy gap distribution for the standard quantum annealing Hamiltonian given by Eq. (1.19) followed the Fréchet functions, the transformed-translated-Weibull functions and the exponentially-decaying functions fit well to the distributions corresponding to the annealing Hamiltonian given by Eq. (5.1) with the ferromagnetic and the antiferromagnetic trigger Hamiltonian, respectively. In the long annealing time regime, one could use the Landau-Zener formula to map the distributions of the minimum energy gaps to the success probability distributions. From the simulations, we obtained three distinct distributions for the success probability, namely, unimodal, bimodal, and constant distributions. Interestingly, we also obtained these three distributions for the success probability using the D-Wave annealers DW2000Q and DWAdv for solving the set of 2-SAT problems.

We found an exponential scaling of the minimum energy gaps and the run-time  $TTS99$  with the size of the problem, for all the annealing times considered in this work, and using both simulations and the D-Wave systems. For sufficiently long annealing times, we found an agreement between the numerically obtained scaling exponents of  $TTS99$  and the theoretically predicted scaling of the annealing time required to ascertain an adiabatic evolution of the state of the system as the size of the problems grows (based on the scaling exponent of the minimum energy gaps) for all the three annealing Hamiltonians considered. This led to a rather poor scaling of the  $TTS99$  for the standard quantum annealing Hamiltonian (Eq. (1.19)) compared not only with the scaling of the run-time using simulated annealing ( $r_{SA} = 0.34$ ), but also compared to that for a brute-force search of the ground state. However, for short annealing times like  $T_A = 10$ , the scaling exponent showed great improvements, as in this limit non-adiabatic mechanisms such as fast

annealing became dominant and can help enhance the success probability.

Although still exponential, the scaling of the minimum energy gaps, and hence  $TTS99$ , was greatly improved with the addition of both the trigger Hamiltonians compared to that of the standard quantum annealing Hamiltonian. Furthermore, we obtained smaller scaling exponents also compared to the scaling of the brute-force search for the ground state for both types of the trigger Hamiltonians and all the annealing times considered. In addition, in some cases, we found a better scaling behavior than that of simulated annealing. Since the addition of the antiferromagnetic trigger Hamiltonian facilitates the non-adiabatic mechanisms, this choice for the annealing Hamiltonian could result in a much better scaling in the short annealing time limit. On the other hand, the improvement in the case of adding the ferromagnetic trigger Hamiltonian was mainly due to an enlargement of the minimum energy gaps, and therefore for long annealing times resulted in the best scaling of  $TTS99$ .

Lastly, compared to the simulation results, the scaling exponents for  $TTS99$  obtained using the two D-Wave systems were significantly smaller, especially for the new generation DWAdv of the annealers. Moreover, in some cases, the scaling behavior was better than that for simulated annealing. However, since the D-Wave systems only implement the standard quantum annealing Hamiltonian, the deviations from the simulations results, despite of much longer annealing times on the D-Wave systems, were indicative of the presence of noise and temperature effects in the system. It should however be reemphasized that the D-Wave systems do not implement the linear annealing scheme adopted in the simulation work.



## 7. Modifying the initial Hamiltonian

Quantum annealing is believed to possess certain features that can give it an edge in solving combinatorial optimization problems over simulated annealing. One of the main reasons behind this conjecture is that in the case of simulated annealing, while searching for the configuration with the lowest energy from the energy landscape of the problem Hamiltonian, the state of the system can get trapped in a local minimum if the potential barrier becomes too high. On the other hand, quantum annealing, making use of quantum tunnelling, can cause the state of the system to tunnel through such a barrier to continue the search for the global minimum. This tunnelling is facilitated by the addition of a non-commuting initial Hamiltonian, generally the 1-local uniform transverse field, to the Ising Hamiltonian encoding the optimization problem.

Previous studies have indicated that in case of degenerate problem Hamiltonians, including higher-order coupling terms to the initial Hamiltonian can help in sampling all the ground states (i.e., yield all the solutions to the encoded optimization problem) [MNK09; Kön+19]. In this chapter we assess the effects of such initial Hamiltonians on the overall performance of the quantum annealing Hamiltonian for solving 2-SAT problems with unique satisfying assignments.

To this end, we first discuss the types of initial Hamiltonians considered for this work, and then proceed to study their effects on the minimum energy gaps between the ground state and the first excited state of the annealing Hamiltonian, and the success probability of the quantum annealing algorithm. We also analyze the scaling behavior of the minimum energy gap and the time to solution (TTS99) as a consequence of adding higher-order couplings to the standard initial Hamiltonian.

### 7.1. Choices for the initial Hamiltonian

In this section, we discuss the choices for the initial Hamiltonian considered in this work. To the standard 1-local uniform transverse field Hamiltonian, used as the initial Hamiltonian by the D-Wave systems, we add up to 3-local transverse field coupling terms. As in the case of the trigger Hamiltonians (Chapter 5), these couplings can be chosen to be of either ferromagnetic or antiferromagnetic type. While the inclusion of the ferromagnetic  $x$ -couplings in the initial Hamiltonian retains the uniform superposition state as the ground state of the initial Hamiltonian, the antiferromagnetic  $x$ -couplings in the initial Hamiltonian can result in a degenerated ground state. Moreover, determining the ground state of the initial Hamiltonian is not as straightforward in case that the initial Hamiltonian consists antiferromagnetic couplings, making it an unsuitable choice for the quantum annealing algorithm. For concreteness, we fix the strength of all the additional 2-local  $x$ -couplings to 1, while that for the 3-local couplings to 0.5.

Furthermore, we observe that other than the type of the higher-order x-couplings, the geometry in which they are added to the initial Hamiltonian also plays an important role in determining the performance of the resulting quantum annealing Hamiltonian. For this work, we consider the following three geometries and their combinations.

- **Graph:** In this geometry, the higher-order couplings are added according to the graph of the problem Hamiltonian. For the additional 2-local terms, it is straightforward to identify all the 2-local z-couplings from the problem Hamiltonian, as they are explicitly written in the Ising form of the problem. On the other hand, for adding the 3-local x-couplings according to the problem graph, we determine all possible 3-variable connections from the graph edges, and then add the 3-local x-couplings between them. We label the initial Hamiltonian with additional 2-local terms added in the graph geometry as "2x-graph". However, for the 3-local terms, we have an option of including or excluding the 2-local terms. This results in the initial Hamiltonian "3x-graph" consisting of 3-local terms and 2-local terms, both added according to the problem graph, and the initial Hamiltonian "3x-graph-w/o-2x" without the 2-local terms.
- **Chain:** For this choice, the higher-order couplings are added to the standard initial Hamiltonian, in a chain-like manner, independently of the problem graph, such that each variable occurs at most twice in the additional 2-local or 3-local terms. For example, for a 5-variable problem, the additional 2-local terms in the driver Hamiltonian are  $\sigma_1^x \sigma_2^x$ ,  $\sigma_2^x \sigma_3^x$ ,  $\sigma_3^x \sigma_4^x$ , and  $\sigma_4^x \sigma_5^x$  while for an 8-variable problem, the additional 3-local terms following the chain geometry are  $\sigma_1^x \sigma_2^x \sigma_3^x$ ,  $\sigma_3^x \sigma_4^x \sigma_5^x$  and  $\sigma_5^x \sigma_6^x \sigma_7^x$ . The resulting initial Hamiltonian with the addition of the 2-local x-couplings will be referred to as the "2x-chain" initial Hamiltonian. While adding the 3-local terms to the initial Hamiltonian in a chain-like manner, two questions become relevant regarding the addition of the 2-local terms, namely, whether or not to include them and which geometry to choose for them in case they are added. Out of all the possible choices, we consider the initial Hamiltonians "3x-chain" with 3-local x-couplings added in the chain geometry and the 2-local terms according to the problem graph, and "3x-chain-w/o-2x" with 3-local x-couplings in the chain geometry, and without the 2-local terms.
- **Ring:** In this case, the additional 3-local couplings are independent of the problem Hamiltonian, and are added in ring-like manner, such that each variable of the problem contributes three 3-local terms to the initial Hamiltonian, except for the first, second, and the last variable which occur only twice. In this work, we choose this geometry for the additional 3-local terms, while choosing the 2-local x-couplings in accordance with the problem graph. The resulting Hamiltonian is labelled as "3x-ring" initial Hamiltonian.

## 7.2. Results

We focus now on gauging the performance of the quantum annealing algorithm with different initial Hamiltonians for solving the set of 1000 12-variable 2-SAT problems. In order to do so, we study first the minimum energy gaps between the ground state and the first excited state of the annealing Hamiltonian, and subsequently investigate the resulting success probabilities corresponding to different annealing times. We also analyze the scaling of the minimum energy gap and the time to solution (TTS99) for 9 sets of 2-SAT problems with the size of the problems ranging from 10-variable to 18-variable problems.

### 7.2.1. Minimum energy gaps

As established in section 1.3, according to the adiabatic theorem (Eq. (1.22)), the minimum energy gap between the ground state and the first excited state of the annealing Hamiltonian plays a crucial role in determining the performance of the quantum annealing algorithm. This subsection focuses on the effects that different choices for the initial Hamiltonian have on the minimum energy gap. In Fig. 7.1, we show the scatter plots

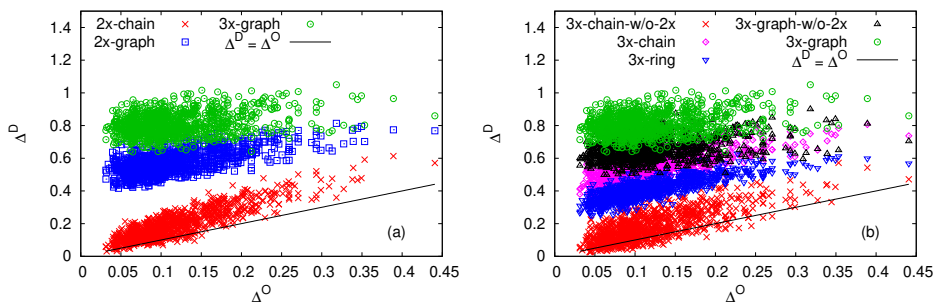


Figure 7.1.: Minimum energy gaps for the quantum annealing algorithm with different initial Hamiltonians,  $\Delta^D$ , against the minimum energy gap using the standard initial Hamiltonian,  $\Delta^O$ .

for the minimum energy gaps  $\Delta^D$  obtained upon adding the additional couplings to the standard initial Hamiltonian, against the minimum energy gaps  $\Delta^O$  obtained using the standard initial Hamiltonian. For more legibility, we have separated the results for the different initial Hamiltonians in two plots, while keeping the results for the annealing Hamiltonian with the 3x-graph initial Hamiltonian in both the plots to allow for an easy comparison.

As the first observation, we note that as a consequence of including higher-order coupling terms in the initial Hamiltonian, the resulting annealing Hamiltonian has a larger minimum energy gap between the lowest two energy levels, for a majority of the problems belonging to the set, for all choices of the initial Hamiltonians. Quantitatively, for all the choices of the initial Hamiltonians considered, at least 850 problems out of the 1000

problems in the set have an enlarged minimum energy gap compared to the standard quantum annealing Hamiltonian.

Next, we note from Fig. 7.1, that for all the choices of the initial Hamiltonian where either the 2-local or the 3-local couplings are added according to the problem graph (namely, 2x-graph, 3x-chain and 3x-ring, 3x-graph-w/o-2x and 3x-graph), all the problems of the set have an enlarged minimum energy gap compared to that for the standard quantum annealing Hamiltonian. On the other hand, although the other choices mostly result in an enlargement of the minimum energy gaps compared to those for the standard quantum annealing Hamiltonian, 41 and 150 problems of the set are found to have reduced minimum energy gaps for 2x-chain and 3x-chain-w/o-2x initial Hamiltonians, respectively.

Moreover, we observe that adding the 3-local couplings to the 2x-graph initial Hamiltonian in the chain or the ring geometry leads to a decrease in the minimum energy gap for a majority of the problems compared to the minimum energy gaps with the 2x-graph initial Hamiltonian. Only 180 problems using the 3x-chain initial Hamiltonian, and none of the problems upon choosing the 3x-ring initial Hamiltonian have a larger minimum energy gap compared to the gaps obtained with 2x-graph initial Hamiltonian. However, for 941 problems of the set, the minimum energy gap for the annealing Hamiltonian with the 3x-graph-w/o-2x initial Hamiltonian is larger compared to that with the 2x-graph initial Hamiltonian. Lastly, we observe that the largest increase in the minimum energy gaps is accompanied with choosing 3x-graph initial Hamiltonian for the quantum annealing algorithm. This suggests that adding the 2-local and 3-local coupling terms according to the problem graph is more favourable than in the cases where the higher-order couplings are independent of the problem Hamiltonian.

## 7.2.2. Success probability

Having discussed how the addition of different higher-order coupling terms to the standard initial Hamiltonian affects the minimum energy gaps between the lowest two energy levels of the annealing Hamiltonian, in this section, we discuss their effects on the success probability of the quantum annealing algorithm, i.e., the probability of the algorithm to find the ground state of the problem Hamiltonian. Figure 7.2 shows the scatter plots

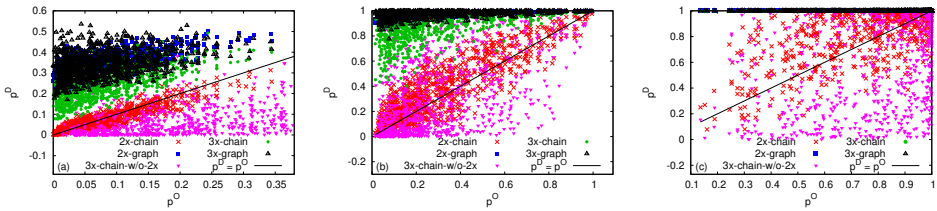


Figure 7.2.: Success probability  $p^D$  upon using different initial Hamiltonians against the success probability  $p^O$  using the standard initial Hamiltonian for quantum annealing, (a)  $T_A = 10$ , (b)  $T_A = 100$ , and (c)  $T_A = 1000$ .

of the success probabilities  $p^D$  obtained using the quantum annealing Hamiltonian with

the additional 2-local and 3-local couplings, against the success probabilities  $p^O$  obtained from the quantum annealing Hamiltonian with the standard 1-local initial Hamiltonian, for annealing times  $T_A = 10, 100, 1000$ . The results corresponding to initial Hamiltonians 3x-ring and 3x-graph-w/o-2x are similar to that for 3x-chain initial Hamiltonian, and have been omitted from the plot for an improved readability of the results.

We find that for all the annealing times considered and the chosen initial Hamiltonians, with the exception of the initial Hamiltonians 2x-chain and 3x-chain-w/o-2x, the resulting  $p^D$  is larger than  $p^O$  for almost all the problems of the set. This can be explained on the basis of the enlargement of the minimum energy gaps of the majority of the problems in the set for all, but 2x-chain and 3x-chain-w/o-2x initial Hamiltonians. This again is indicative of the fact that including additional couplings in the initial Hamiltonian according to the graph of the problem Hamiltonian is beneficial also for the success probability of the algorithm. Moreover, for annealing time  $T_A = 1000$ , the success probabilities corresponding to initial Hamiltonians 2x-graph, 3x-chain, and 3x-graph are close to 1 for almost all the problems in the set.

Table 7.1.: Number of problems with a larger success probability upon including different 3-local terms to the initial Hamiltonian compared to the success probability using 2x-graph initial Hamiltonian, for different annealing times  $T_A$ .

$T_A$	3x-chain-w/o-2x	3x-chain	3x-ring	3x-graph-w/o-2x	3x-graph
10	4	60	0	245	510
100	12	92	0	341	654
1000	2	298	685	216	3

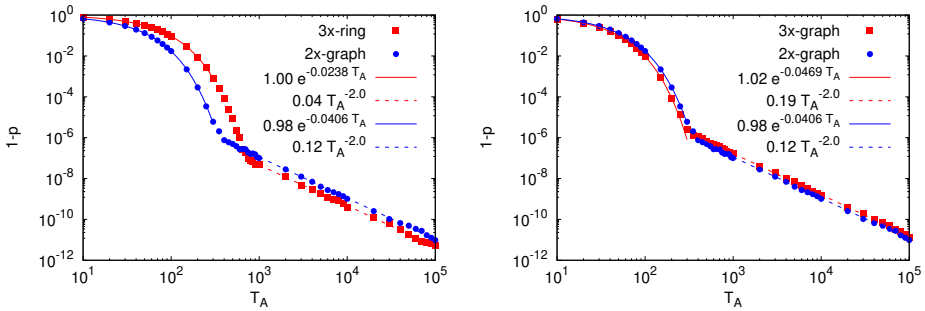


Figure 7.3.: Comparison of the transition probability  $1-p$  obtained using the initial Hamiltonian (a) 3x-ring and (b) 3x-graph, with the 2x-graph initial Hamiltonian, as a function of the annealing time.

Although the success probabilities  $p^D$  are fairly large for all the chosen initial Hamiltonians, and they increase with increasing annealing time, comparing the success probabilities resulting from the quantum annealing algorithm with initial Hamiltonians having 3-local

x-couplings, to that with the 2x-graph initial Hamiltonian, we note from Tab. 7.1 that the success probabilities follow a similar trend as the minimum energy gaps for initial Hamiltonians 3x-chain-w/o-2x and 3x-chain. Both these choices for the initial Hamiltonian result in a decrease in the minimum energy gap compared to the 2x-graph initial Hamiltonian, and hence the success probability compared to the 2x-graph initial Hamiltonian for a majority of the problems in the set. However, there are a few counter-intuitive observations. Although compared to the 2x-graph initial Hamiltonian, the initial Hamiltonian 3x-ring leads to a decrease in the minimum energy gaps for all the problems belonging to the set, 685 problems have a marginally larger success probability for the latter if  $T_A = 1000$ . Another observation is that despite of a majority of the cases having a significantly larger minimum energy gap when the 3-local couplings are added according to the problem graph, only 3 problems have larger success probabilities for  $T_A = 1000$  using the 3x-graph initial Hamiltonian compared to those obtained using the 2x-graph initial Hamiltonian.

A closer look at the success probabilities shown in Fig. 7.2(c) reveals that the success probabilities using these two initial Hamiltonians are actually comparable and close to 1. Although from a practical point of view, such marginal differences in the success probability are somewhat irrelevant, from a theoretical perspective, it is interesting to look for the mechanisms that lead to such differences. In order to understand the reasons for the change in the statistics of the problems with a larger success probability using the 3x-ring and 3x-graph initial Hamiltonians compared to the 2x-graph initial Hamiltonian upon increasing the annealing time, we choose a problem from the set which has a smaller success probability using the 3x-ring initial Hamiltonian compared to that using the 2x-graph initial Hamiltonian for  $T_A = 10$ , but not for  $T_A = 1000$ , and study the behavior of the transition probability,  $1 - p$ , as a function of the annealing time. The resulting plot is shown in Fig. 7.3(a). Additionally, we select a problem instance that has a larger success probability using the 3x-graph initial Hamiltonian compared to the 2x-graph initial Hamiltonian for annealing time  $T_A = 10$ , but not for  $T_A = 1000$ , and perform a similar analysis. The plot for the transition probability as a function of the annealing time for this problem is shown in Fig. 7.3(b). From both the plots, we observe an exponential dependence of the transition probability on the annealing time for the initial part of the annealing-time scan, which then changes to a polynomial-like dependence, for all the three involved initial Hamiltonians. This transition is related to a shift from the dominance of a Landau-Zener like evolution, where the transition probability is exponentially related to the annealing time (see Eq. (1.24)), to a more adiabatic evolution for which the transition probability is of the order  $\mathcal{O}(T_A^{-2})$  for long annealing times (see Appendix A). It is this shift in the behavior of the transition probability as a function of the annealing time that results in a cross-over in the statistics of the success probabilities of the initial Hamiltonians 3x-ring and 3x-graph with respect to the 2x-graph initial Hamiltonian. Since this shift in the behavior of the transition probability with the annealing time is not directly related to the minimum energy gaps between the lowest two energy states of the annealing Hamiltonian, the observations from Tab. 7.1 cannot be explained on the basis of comparing the minimum energy gaps between annealing Hamiltonians supplemented by various initial Hamiltonians.

### 7.2.3. Scaling

Having studied the effects of introducing additional couplings in the initial Hamiltonian on the minimum energy gap and the resulting success probability for different annealing times, we now investigate its scaling aspect. Since adding the 2-local terms according to the graph of the problem Hamiltonian appears to be the most promising choice for the initial Hamiltonian in terms of the success probability, we investigate the scaling of the minimum energy gap and the runtime for different annealing times for this choice.

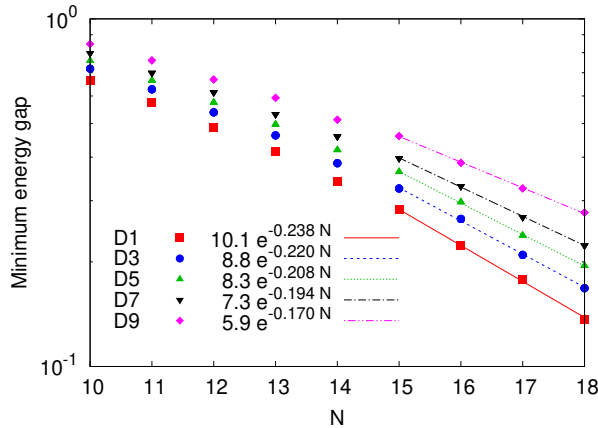


Figure 7.4.: Deciles for the scaling of the minimum energy gap between the ground state and the first excited state of the quantum annealing Hamiltonian with the 2x-graph initial Hamiltonian.

We start with the scaling of the minimum energy gap as function of the problem size. Shown in Fig. 7.4 are the deciles for the minimum energy gap for the quantum annealing Hamiltonian with the 2x-graph initial Hamiltonian. The problems having a smaller minimum energy gap than the first decile represent the hardest problems of the set, while those having larger minimum energy gap than the ninth decile represent the easiest problems. It can be observed that in comparison to the scaling of the minimum energy gap without the additional couplings in the initial Hamiltonian (see Fig.6.4(a)), the scaling upon adding the 2-local couplings according to the problem graph is significantly improved. While for the former, the median minimum energy gap, given by the fifth decile, scales exponentially with an exponent of 0.541 (see Fig.6.4(a)), the scaling exponent of the median minimum energy gap in the latter case is 0.208. Moreover, the spread of the deciles upon adding the extra coupling terms is much smaller than the case where they are excluded.

According to Eq. (6.1), for long annealing times, where the system can be approximated as a two-level system, the scaling of TTS99 should also exhibit a similar improvement. Thus, the median runtime required to keep the evolution of the state adiabatic during the annealing process, should scale exponentially as well, with a scaling constant of 0.416. This value is indeed comparable to the scaling of TTS99, which is the runtime required to

obtain the correct ground state of the problem Hamiltonian at least once with a certainty of 99% in multiple repeated runs of the algorithm, obtained from the simulations of the dynamics of quantum annealing for long annealing times, as shown in Fig. 7.5. For  $T_A = 100$  and 1000, the scaling constant for the median TTS99 is comparable to the theoretical prediction, with scaling exponents of 0.428 and 0.445, respectively. However, for the short annealing time  $T_A = 10$ , where certain non-adiabatic mechanisms can further play a role in improving the success probability, the scaling constant is significantly smaller and is 0.287. Thus, the scaling constants for TTS99 are not only better compared to the annealing algorithm using 1-local initial Hamiltonian, but also better compared to the scaling of the brute-force search method. Lastly, we note that for longer annealing times the scaling of the median TTS99 is slightly better upon introducing additional terms in the initial Hamiltonian compared to that using the quantum annealing algorithm with a trigger Hamiltonian of both ferromagnetic and antiferromagnetic type. On the other hand for short annealing times like  $T_A = 10$  where the non-adiabatic mechanisms are prominent, the algorithm using antiferromagnetic trigger Hamiltonian for annealing exhibits a better scaling.

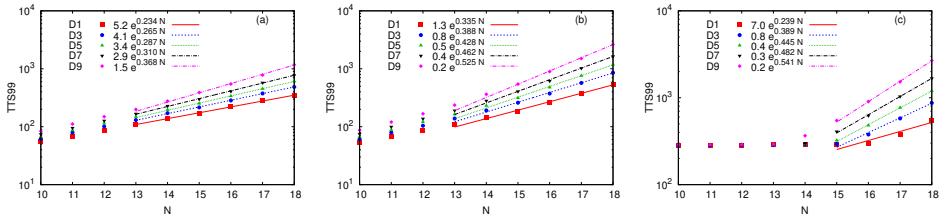


Figure 7.5.: Deciles for the scaling of TTS99 for the quantum annealing Hamiltonian with 2x-graph initial Hamiltonian for (a)  $T_A = 10$ , (b)  $T_A = 100$ , and (c)  $T_A = 1000$ .

### 7.3. Summary

In this chapter, we added higher-order coupling terms to the standard initial Hamiltonian (consisting of 1-local transverse field) used for quantum annealing, and studied its effects on the values and scaling of certain quantities like the minimum energy gap, success probability, and the time to solution TTS99. In designing the new initial Hamiltonians, we made a choice regarding the order of the locality of the extra couplings as well as the geometry in which these terms were added. These results were then compared to the standard choice of initial Hamiltonian. We considered up to 3-local terms transverse coupling terms, which could then be added in a chain-like geometry, ring-like geometry, or according to the graph of the problem Hamiltonian.

We found that the addition of the extra couplings was accompanied with an enlargement of the minimum energy gaps for a majority of the cases, especially if either the 2-local or 3-local terms were added according to the problem graph. The largest enhancement was thus witnessed for '3x-graph' initial Hamiltonian, where both the 2-local and 3-local terms are added according to the problem graph.

According to the Landau-Zener formula, an enlargement of the minimum energy gaps should lead to an increase in the success probability. This improvement in the success probability was indeed observed for all the problems belonging to the 12-variable 2-SAT problem set being considered for the three annealing times  $T_A = 10, 100, 1000$  considered here, except for two choices of initial Hamiltonians. These were the initial Hamiltonians where only 2-local or only 3-local couplings were added in a chain geometry. These were also the choices for the initial Hamiltonian that could lead to a reduction in the minimum energy gap. Although the largest enhancement in the minimum energy gaps corresponded to the 3x-graph initial Hamiltonian, the most reasonable choice for the initial Hamiltonian, in our opinion, would be the 2x-graph initial Hamiltonian, which with its 2-local terms can be implemented relatively easily on the hardware and yielded larger success probabilities compared to even the 3x-graph initial Hamiltonian.

Similar observations were also noted from the scaling analysis conducted using the initial Hamiltonian that delivered the maximum improvement in the success probability, i.e., the 2x-graph initial Hamiltonian. As in the case of including the trigger Hamiltonian in the standard quantum annealing Hamiltonian, the addition of 2-local couplings to the initial Hamiltonian according to the problem graph led to a better scaling of the minimum energy gaps compared to the standard choice of initial Hamiltonian. Furthermore, the scaling exponent of the median minimum energy gaps in this case was also slightly better than that obtained for the quantum annealing Hamiltonian with the ferromagnetic trigger. As a consequence, the scaling of the median TTS99 was also slightly better than the one obtained with the ferromagnetic trigger Hamiltonian, and hence significantly better compared also to the standard quantum annealing Hamiltonian, in the long annealing time limit. However, for short annealing times, the annealing Hamiltonian with the antiferromagnetic trigger Hamiltonian led to better scaling of the TTS99.



## 8. Summary

Quantum annealing is a metaheuristic for solving combinatorial optimization problems, which is inspired by simulated annealing, but where thermal fluctuations are replaced by quantum fluctuations. Quantum annealers are special-purpose quantum computers based on this idea, that specialize at the task of solving optimization problems.

Over the years, adiabatic quantum computing, which is closely related to quantum annealing, has gained the status of being another paradigm of quantum computing, the gate-based model of quantum computing being the other. Moreover, adiabatic quantum computing has been shown to be equivalent to the universal gate-based model of quantum computing.

The availability of commercial quantum annealers offered by D-Wave Quantum Systems Inc. has given an impetus to numerous research work for assessing the suitability of such systems for solving optimization problems. Furthermore, these quantum annealers being the largest quantum computers commercially available till date, have made it possible to implement various real-life and industry-based applications on such systems, in the hopes of finding a speedup of quantum annealing over the existing classical optimization algorithms.

In this work, we studied the performance of quantum annealing for solving several optimization problems by means of various criteria. These criteria included the probability of quantum annealing to solve the given problem, the fairness of annealing to yield all the possible solutions of a problem in case that the problem has more than one solution, as well as the scaling and distribution of some of the performance metrics for quantum annealing. In doing so, we performed, wherever possible, a comparative study of the performance of the ideal implementation of the annealing algorithm by making use of simulations, with the real quantum annealers from D-Wave. For benchmarking purposes, we mainly used sets of hard 2-SAT problems.

As a summary of this work, we discuss here the main findings of this study, addressing the above-mentioned criteria.

We start with one of the most important aspects of an optimization algorithm, that is its capability to solve the given problems. We found that for the chosen sets of hard 2-SAT problems up to 20 variables, the simulations for quantum annealing could solve all the problems belonging to the set, even if the resulting success probability was negligible (e.g.,  $O(10^{-6})$ ) for the hard problems of the set. Moreover, it was observed that the success probability increased with increasing the annealing time, given that one is not in the regime of fast annealing, where the success probability could coincidentally have a large value despite of a short annealing time. However, the simulations for the quantum annealing algorithm were constrained by the number of variables in the problem, as well as the annealing times chosen. On the other hand, the D-Wave systems operate with

much longer annealing times compared to those that can be simulated with a reasonable amount of computational resources. Since the size of the 2-SAT problems considered here is much smaller than the number of qubits available on the D-Wave annealers, most of these problems, as well as other problems derived from them were solvable using these annealers, although the resulting success probability was found to be low for the harder problems. The value of the success probability was noted to depend on the embedding of the problem graph onto the working graph of the annealers, as well as on the different annealing parameters offered such as the annealing time and chain strength between the physical qubits representing a logical qubit. To utilize a larger number of the available qubits, we used the so-called multiple-copies problem instances, which were created by joining copies of a given 12- or 18-variable 2-SAT problem. We found that for the instances consisting of 10-50 copies of a hard 18-variables 2-SAT problem, the D-Wave system could not yield the ground state of the whole problem, irrespective of the fact whether these copies were connected or unconnected to each other. Since the 2-SAT problems are sparsely connected, we also used sets of two kinds of QUBO problems with all-to-all connectivity and up to 200 variables, in order to use a larger number of the available couplers. With the Advantage\_system5.1, it was not possible to obtain the solutions of the random QUBO problems (which have randomly chosen magnetization and couplings in the interval  $[-1, 1]$ ) consisting of more than 80 variables, except for one instance of a 100-variable problem. For the other set of QUBO problems, namely, the regular problems for which the values of the magnetization and couplings were determined using a specific formula, the D-Wave system could solve problems up to 170 variables.

While for most practical problems, the most relevant quantifier for assessing the performance of quantum annealing is the probability of solving the problem, for problems that have more than one possible solution, another quantity of interest is the ability of the algorithm to sample all the solutions of the problem with a comparable sampling probability. For this purpose, we used a set of 2-SAT problems with four satisfying solutions and  $6 \leq N \leq 20$  variables. Using our simulations, we found that for a majority of the problems, quantum annealing could yield the four ground states of the problems with a uniform success probability if the annealing time was sufficiently long. However, in some cases, we found the sampling probabilities to be unequal even if the chosen annealing time was long enough for an almost adiabatic evolution of the state of the system. In yet more extreme cases, we also observed a total suppression of one of the ground states of the problem Hamiltonian. If the annealing times were long, such observations could be justified based on the ground state of the Hamiltonian towards the end of the annealing process, i.e., near  $s = 1$ , obtained using perturbation theory. On the contrary, the sampling probabilities of the ground states of such degenerate problems obtained from D-Wave's Advantage\_system5.1 did not show such a behavior, and the sampling probabilities of the four ground states were approximately equal. Despite of much longer annealing times used on the D-Wave systems ( $20 \mu s$  compared to approximately  $50 ns$  used in simulations), the sampling results were not in agreement with the simulation results, as well as with the theoretical predictions, suggesting that such observations confirmed the presence of imperfections like noise and temperature effects in the quantum annealers.

Next, while posing the same question of fair sampling of the solutions of problems with

---

more than a unique solution, we explored the efficiency of the reverse annealing protocol for the same. Reverse annealing is based on the motivation that starting from one of the low-energy classical states of the problem Hamiltonian, it could be possible to reach a state with lower energy or sample a larger number of ground states by annealing backwards (that is by increasing the strength of the transverse Hamiltonian) up to a certain reversal distance, and then continuing normally as in the case of standard quantum annealing. For this purpose, we implemented the reverse annealing algorithm with similar annealing parameters as offered by the D-Wave systems for the reverse annealing protocol, and used as a test for a 14-variable 2-SAT problem that was predicted to have a zero sampling probability for one of the four ground states. The reverse annealing protocol for the D-Wave system specifies various controls such as the reverse and forward annealing times, the reversal distance, waiting times, if at all included, and the initial state, all of which were probed in the context of sampling the ground states of the problem Hamiltonians. The numerical results indicated that the sampling probability of the ground state that was predicted to be totally suppressed according to perturbation theory, stayed fairly low for almost all the choices for the annealing parameters, if the algorithm did not start in the suppressed state. Furthermore, this sampling probability was found to fluctuate with the annealing times, and with varying the reversal distance, due to the accumulation of different phases in the final components of the wavefunction. For large values of reversal distance, the results obtained from the D-Wave system were in agreement with the simulation results, that is the sampling probability of the ground state predicted to be suppressed, was indeed found to be zero in this case for other choices of the annealing parameters. This suggests, that in the regime before the value of  $s$  corresponding to the anticrossing, the noise and temperature effects do not play a very significant role. However, lowering the value of the reversal distance leads to a more even sampling of the four ground states, as was also found to be the case for the standard quantum annealing protocol.

One of the most pertinent measures for deciding the suitability of an algorithm for solving a problem is the scaling of its performance metrics as a function of the size of the problem. The simulation of the quantum annealing algorithm suggested an exponential scaling of the minimum energy gap between the ground state and the first excited state of the annealing Hamiltonian. Furthermore, we found that the median TTS99 (the run-time required to obtain the solution of the problem at once in multiple runs of the algorithm with a certainty of 0.99) increases exponentially with the size of the problems with an exponent of 1.205 for an annealing time  $T_A = 1000$ . These scaling results were in agreement with the theoretical predictions for TTS99 based on the scaling of the minimum energy gaps between the ground state and the first excited state of these problems, in turn confirming that the minimum energy gap is a crucial quantity for determining the performance of the quantum annealing algorithm. These results indicated that in the long annealing time limit, the ideal quantum annealing performed even worse than a simple brute-force search of the ground state of the problem Hamiltonian which scaled exponentially but with an exponent of 0.693. For the short annealing time  $T_A = 10$ , however, the scaling exponent for the median TTS99 was 0.530 which was significantly better than the exponent in the adiabatic case, and slightly better than that for the brute-force search.

The reason behind such an improvement was the non-adiabatic mechanism of fast annealing where the state of the system deviates from the instantaneous ground state before the anticrossing to the next energy level, owing to the short annealing time. Upon reaching the anticrossing, some of the amplitude transferred to the higher energy states can return to the ground state, thus increasing the success probability. However, the scaling results from the D-Wave systems DW\_2000Q and Advantage\_system1.1 were quite distinct from the numerical results. Although still exponential, the scaling exponents for the median TTS99 for the former was 0.511, while for the latter was 0.377 for  $T_A = 20 \mu s$ . Although the exponent from the DW\_2000Q system was comparable to that obtained from the simulations for a short annealing time, the annealing times used on the D-Wave systems were significantly longer. For such time scales, the scaling of the TTS99 should have matched with the simulations and the theoretical estimates obtained from the scaling of the minimum energy gaps, had the D-Wave annealers been ideal systems. This deviation from the expected behavior once again made apparent the fact that the D-Wave systems are prone to noise and temperature effects.

We also used the D-Wave systems to determine the scaling complexity of the two classes of fully-connected QUBO problems, with problem sizes varying from 10 to 200. For this range of problem sizes, it was not feasible to determine the scaling of the ideal quantum annealing algorithm using simulations. We found the scaling of the mean success probability to be exponential for both the classes. However, the scaling exponents for these problems were 0.163 for the random problems, and 0.090 for the regular problems. For a comparison, the average success probability for the given 2-SAT problems scales with an exponent of 0.269 as a function of the system size. Thus, it was concluded that the performance of quantum annealing depended on the problems at hand, with the 2-SAT problems being the hardest and the regular problems being the easiest. These findings were found to correlate well with the estimates of hardness obtained from the Hamming distance analysis performed for the smaller problem instances of each class.

Since the ideal quantum annealing algorithm was found to perform rather poorly for the given set of hard 2-SAT problems, not only compared to the known classical algorithms but even a simple enumeration of all possible solutions, we studied the performance of the quantum annealing algorithm upon introducing two modifications to it by means of simulations. The first was to introduce an additional term in the standard quantum annealing algorithm, namely, the trigger Hamiltonian, which comprises of transverse couplings. This Hamiltonian vanishes at the beginning and end of the annealing process in order to preserve the respective ground states at these points. This trigger could further be of two types ferromagnetic and antiferromagnetic, and its strength could be controlled using a strength parameter. It was found that the addition of the ferromagnetic trigger Hamiltonian led to an enlargement of the minimum energy gap between the ground state and the first excited state of the annealing Hamiltonian for all the problems. This improved the scaling of the minimum energy gaps between the ground state and the first excited state of the problems significantly, thereby improving the scaling of the success probability in the adiabatic limit. In this case, the scaling exponent for the median TTS99 was found to be 0.478 for  $T_A = 1000$ , which is significantly smaller than that for the standard algorithm (1.205 for  $T_A = 1000$ ). On the other hand, while the addition of the antiferromagnetic

---

trigger Hamiltonian could either enlarge or reduce the minimum energy gap, it was noted that its inclusion could vastly alter the energy spectrum of the annealing Hamiltonian in ways that could facilitate certain non-adiabatic mechanisms. These included fast annealing, occurrence of an even number of comparably small anticrossings between the lowest two energy levels, or a change in the shape of the anticrossing. While the addition of this type of the trigger Hamiltonian improved the scaling of the minimum energy gap, and therefore the scaling exponent of the median TTS99 was smaller than the standard algorithm (0.619 for  $T_A = 1000$ ), the largest improvement in this case was noted for  $T_A = 10$ , the regime where the non-adiabatic mechanisms play a prominent role. The scaling exponent of the median TTS99 in this case was found to be 0.277, which was smaller than that for simulated annealing.

Lastly, we studied the effects of including higher-order couplings to the standard initial Hamiltonian chosen for the quantum annealing algorithm. We introduced up to 3-local terms to the initial Hamiltonian, and studied its effect on the values and/or scaling of the minimum energy gap between the ground state and the first excited state of the annealing Hamiltonian, the resulting success probabilities for different annealing times, and TTS99. Unlike the case for the trigger Hamiltonian, the higher-order couplings in the initial Hamiltonian were chosen to be of the ferromagnetic kind in order to ensure that the initial ground state is non-degenerate. Other than the order of these coupling terms, we also studied the effect of varying the geometries in which these extra couplings were added. It was observed that while all kinds of resulting initial Hamiltonian led to an increase in the minimum energy gap for a majority of the cases, the largest improvements were accompanied with the initial Hamiltonian consisting of 2-local and 3-local coupling terms added according to the same graph as that of the problem Hamiltonian. Similar observations were also noted for the success probability. For this reason, we chose the initial Hamiltonian with 2-local couplings according to the problem graph for studying the scaling of the TTS99 for the given set of problems. In this case, the scaling exponent of the median TTS99 was found to be slightly better than that obtained for the standard quantum annealing Hamiltonian with the ferromagnetic trigger for long annealing times  $T_A = 100, 1000$ .



# Appendices

# A. Proof of the adiabatic theorem

In this section, we present a proof for the adiabatic theorem, assuming that the system is initialised in the ground state of the initial Hamiltonian and that the instantaneous ground state of the Hamiltonian during the evolution is non-degenerate [Chi17]. For a more general treatment see [Teu03; JRS07].

We start with the TDSE, which is given by

$$i\frac{\partial}{\partial t}|\psi(t)\rangle = H(t)|\psi(t)\rangle, \quad (\text{A.1})$$

and replace the time  $t$  by a dimensionless variable  $s = t/T_A$ , where  $T_A$  is the total annealing time, so that Eq. (A.1) becomes

$$i\frac{\partial}{\partial s}|\psi(s)\rangle = T_A H(s)|\psi(s)\rangle. \quad (\text{A.2})$$

In terms of the unitary time evolution operator  $U(s)$  satisfying

$$i\dot{U}(s) = T_A H(s)U(s), \quad (\text{A.3})$$

we have

$$|\psi(s)\rangle = U(s)|\psi(0)\rangle. \quad (\text{A.4})$$

We initialize the system in the ground state  $|\phi(0)\rangle$  of the initial Hamiltonian  $H(0)$ , such that

$$H(0)|\phi(0)\rangle = E(0)|\phi(0)\rangle, \quad (\text{A.5})$$

where  $E(0)$  is the ground state energy of the initial Hamiltonian.

We wish to compare the evolution of the initial state according to the TDSE (Eq. (A.1)) with the ideal adiabatic evolution where  $|\psi(0)\rangle = |\phi(0)\rangle$  evolves into  $|\phi(s)\rangle$  which is the ground state of the instantaneous Hamiltonian  $H(s)$ , meaning that

$$H(s)|\phi(s)\rangle = E(s)|\phi(s)\rangle. \quad (\text{A.6})$$

To this end, we define a new Hamiltonian by

$$H_a(s) = T_A H(s) + i[\dot{P}(s), P(s)], \quad (\text{A.7})$$

where

$$P(s) = |\phi(s)\rangle\langle\phi(s)|, \quad (\text{A.8})$$

is the projection operator onto the ground state of the instantaneous Hamiltonian  $H(s)$  and  $\dot{P}(s) = \partial P(s)/\partial s$ .

---

Noting that  $[H, P] = 0$  and using Eq. (A.7) we find

$$[H_a, P] = T_A[H, P] + i[[\dot{P}, P], P] = i[\dot{P}P - 2P\dot{P}P + P\dot{P}]. \quad (\text{A.9})$$

Since  $P^2 = P$ , differentiating both sides we obtain

$$\dot{P} = \dot{P}P + P\dot{P}. \quad (\text{A.10})$$

Multiplying both sides of Eq. (A.10) by  $P$  yields

$$P\dot{P}P = 0. \quad (\text{A.11})$$

Upon substituting Eq. (A.10) in Eq. (A.9), we obtain

$$i\dot{P} = i\left(\frac{\partial}{\partial s}|\phi\rangle\right)\langle\phi| + i|\phi\rangle\frac{\partial}{\partial s}\langle\phi| = [H_a, P]. \quad (\text{A.12})$$

In terms of the unitary time evolution operator  $U_a(s)$  satisfying

$$i\dot{U}_a(s) = H_a(s)U_a(s), \quad (\text{A.13})$$

it follows immediately from Eq. (A.12) that

$$P(s) = U_a(s)P(0)U_a^\dagger(s). \quad (\text{A.14})$$

Therefore, the above construction guarantees that the time evolution of the initial state under  $H_a(s)$  obtained by solving

$$i\frac{\partial}{\partial s}|\psi(s)\rangle = H_a(s)|\psi(s)\rangle, \quad (\text{A.15})$$

results in the state  $|\psi(s)\rangle = e^{i\theta(s)}|\phi(s)\rangle$  with some irrelevant time-dependent phase  $\theta(s)$ . Therefore, the time evolution Eq. (A.15) solves the instantaneous eigenvalue problem Eq. (A.6) or, in other words, the time evolution starting from the ground state is transitionless. Thus, we may say that Eq. (A.7) defines the Hamiltonian that generates the exact adiabatic evolution.

Next, we derive a few relations that will be required to construct a proof of the adiabatic theorem, under the assumption that the ground state of the instantaneous Hamiltonian is non-degenerate for all values of  $0 \leq s \leq 1$ .

We focus on finding a bound on the transition probability, defined as the probability of the amplitude present in the initial state (the ground state of the initial Hamiltonian) to get transferred to other eigenstates, for a system evolving according to the TDSE [JRS07]. Defining the projection operator  $Q(s)$  as the projection of the wavefunction to the whole eigenspace of the instantaneous Hamiltonian excluding its ground state, i.e.,  $Q(s) = 1 - P(s)$ , the transition probability is given as  $\|Q(s)U(s)P(0)|\psi(0)\rangle\|^2$ . Note that from Eq. (A.14) it follows that  $Q(s) = U_a(s)Q(0)U_a^\dagger(s)$ . Therefore, we have

$$\|Q(s)U(s)P(0)|\psi(0)\rangle\|^2 = \|U_a(s)Q(0)\Omega(s)P(0)|\psi(0)\rangle\|^2 \leq \|Q(0)\Omega(s)P(0)\|^2, \quad (\text{A.16})$$

where we have defined  $\Omega(s) = U_a^\dagger(s)U(s)$ .

To find an upper bound on  $\|Q(0)\Omega(1)P(0)\|$ , we first note that

$$\dot{\Omega}(s) = iU_a^\dagger(s)(H_a - T_A H)U(s) = -U_a^\dagger(s)[\dot{P}(s), P(s)]U(s), \quad (\text{A.17})$$

such that upon integrating the latter we have

$$\Omega(1) = 1 - \int_0^1 U_a^\dagger(s)[\dot{P}(s), P(s)]U(s) ds. \quad (\text{A.18})$$

Second we define the operator,

$$F = R\dot{P}P + P\dot{P}R, \quad (\text{A.19})$$

and the resolvent,  $R$

$$R = \frac{1}{H - E}, \quad (\text{A.20})$$

where  $E$  is the ground state energy of the instantaneous Hamiltonian, and therefore a pole of the resolvent  $R$ . Here and in the following, in order to make the notation more compact, we omit the explicit  $s$  dependence wherever it is clear from context. Using  $F$  and  $R$ , we can express the commutator  $[H, F]$  as

$$\begin{aligned} [H, F] &= HR\dot{P}P + HP\dot{P}R - R\dot{P}PH - P\dot{P}RH \\ &= (1 + ER)\dot{P}P + EP\dot{P}R - ER\dot{P}P - P\dot{P}(1 + ER) = [\dot{P}, P], \end{aligned} \quad (\text{A.21})$$

where we have made use of the fact that  $(H - E)R = 1$  i.e.,  $HR = 1 + ER$ ,  $PH = EP$ , and that  $R$  and  $H$  commute. Defining

$$\tilde{F} = U^\dagger F U, \quad (\text{A.22})$$

so that

$$\begin{aligned} \dot{\tilde{F}} &= \dot{U}^\dagger F U + U^\dagger \dot{F} U + U^\dagger F \dot{U} = iT_A H U^\dagger F U + U^\dagger \dot{F} U - iU^\dagger F T_A H U \\ &= iT_A U^\dagger [H, F] U + U^\dagger \dot{F} U, \end{aligned} \quad (\text{A.23})$$

where we have used Eq. (A.3), and thus,

$$U^\dagger [\dot{P}, P] U = U^\dagger [H, F] U = \frac{1}{iT_A} (\dot{\tilde{F}} - U^\dagger \dot{F} U). \quad (\text{A.24})$$

Substituting Eq. (A.24) in Eq. (A.18), and integrating the first term by parts, we obtain

$$\begin{aligned} \Omega(1) &= 1 + \frac{i}{T_A} \int_0^1 U_a^\dagger U (\dot{\tilde{F}} - U^\dagger \dot{F} U) ds = 1 + \frac{i}{T_A} \left( U_a^\dagger U \tilde{F} \Big|_0^1 - \int_0^1 \left( \frac{d}{ds} (U_a^\dagger U) \tilde{F} + U_a^\dagger \dot{F} U \right) ds \right) \\ &= 1 + \frac{i}{T_A} \left( U_a^\dagger U \tilde{F} \Big|_0^1 - \int_0^1 (U_a^\dagger \dot{F} U - U_a^\dagger [\dot{P}, P] U \tilde{F}) ds \right), \end{aligned} \quad (\text{A.25})$$

where we have computed the derivative of  $U_a^\dagger U$  as in Eq. (A.17).

---

Returning to the quantity of interest given in Eq. (A.16), and using Eq. (A.25), we have

$$Q(0)\Omega(1)P(0) = \frac{i}{T_A} \left( Q(0)U_a^\dagger U\tilde{F} \Big|_0^1 P(0) - \int_0^1 (Q(0)U_a^\dagger \dot{F} U P(0) - Q(0)U_a^\dagger [\dot{P}, P] U \tilde{F} P(0)) ds \right), \quad (\text{A.26})$$

where the first term vanishes as operators  $Q(0)$  and  $P(0)$  are complementary to each other. Since,  $Q(0)U_a^\dagger = U_a^\dagger Q$ , Eq. (A.26) becomes

$$Q(0)\Omega(1)P(0) = \frac{i}{T_A} \left( Q(0)U_a^\dagger U\tilde{F} \Big|_0^1 P(0) - \int_0^1 (U_a^\dagger Q \dot{F} U P(0) - U_a^\dagger Q [\dot{P}, P] U \tilde{F} P(0)) ds \right). \quad (\text{A.27})$$

Appealing to the triangle inequality, we have

$$T_A \|Q(0)\Omega(1)P(0)\| \leq \|F(0)\| + \|F(1)\| + \int_0^1 (\|Q\dot{F}\| + \|Q\dot{P}PF\| + \|QP\dot{P}F\|) ds. \quad (\text{A.28})$$

Since operators  $Q$  and  $P$  are complementary to each other, the last term in Eq. (A.28) vanishes, and we obtain

$$\begin{aligned} T_A \|Q(0)\Omega P(0)\| &\leq \|F(0)\| + \|F(1)\| + \int_0^1 (\|Q\dot{F}\| + \|Q\dot{P}PF\|) ds \\ &\leq \|F(0)\| + \|F(1)\| + \int_0^1 (\|Q\dot{F}\| + \|\dot{P}\| \cdot \|F\|) ds. \end{aligned} \quad (\text{A.29})$$

We now consider the terms in Eq. (A.29) one by one. Using the definition of  $F$  from Eq. (A.19), and noting that  $\dot{P}P = (1 - P)\dot{P} = Q\dot{P}$

$$\|F\| \leq 2\|R\dot{P}P\| = 2\|RQ\dot{P}\| \leq 2\|RQ\| \cdot \|\dot{P}\|. \quad (\text{A.30})$$

Since the projector  $Q$  projects any wavefunction to the eigenspace barring the ground state,  $\|RQ\| \leq 1/\Delta$ , where  $\Delta$  is the energy gap between the ground state and the first excited state of the instantaneous Hamiltonian,

$$\|F\| \leq \frac{\|\dot{P}\|}{\Delta}. \quad (\text{A.31})$$

Moving on to the next term in Eq. (A.29), differentiating  $F$  given by Eq. (A.19) we have

$$\begin{aligned} \|Q\dot{F}\| &= \|Q\dot{R}\dot{P}P + QR\dot{P}P + QR\dot{P}^2 + Q\dot{P}^2R + QP\dot{P}R + QP\dot{P}R\| \\ &= \|Q\dot{R}\dot{P}P + QR\dot{P}P + QR\dot{P}^2 + Q\dot{P}^2R\|, \end{aligned} \quad (\text{A.32})$$

where the last two terms in the first step vanish as projectors  $Q$  and  $P$  are complementary. Using  $(H - E)R = 1$ , we find  $\dot{R} = -R\dot{H}R$ , we obtain

$$\|Q\dot{F}\| \leq \|QR\dot{H}RQ\dot{P}\| + \|QR\ddot{P}\| + \|QR\dot{P}^2\| + \|Q\dot{P}^2R\|. \quad (\text{A.33})$$

Let us now consider each term in Eq. (A.33) separately, we have

$$\|QR\dot{H}RQ\dot{P}\| \leq \|QR\| \cdot \|\dot{H}\| \cdot \|RQ\| \cdot \|\dot{P}\| \leq \frac{\|\dot{H}\| \cdot \|\dot{P}\|}{\Delta^2}, \quad (\text{A.34})$$

$$\|QR\ddot{P}\| = \|QR(Q + P)\ddot{P}\| \leq \|QR\| \cdot \|Q\ddot{P}\| \leq \|QR\| \cdot \|Q\dot{P}P\| \leq \frac{\|Q\dot{P}P\|}{\Delta}, \quad (\text{A.35})$$

where the term  $\|QR\dot{P}^2\|$  vanished because of  $Q$  and  $P$  being complementary,

$$\|QR\dot{P}^2\| \leq \|QR\| \cdot \|\dot{P}^2\| \leq \frac{\|\dot{P}^2\|}{\Delta}, \quad (\text{A.36})$$

and

$$\|Q\dot{P}^2R\| = \|Q\dot{P}(P + Q)\dot{P}R\| = \|Q\dot{P}P\dot{P}R + Q\dot{P}QR\| \leq \|Q\dot{P}^2QR\| \leq \frac{\|\dot{P}^2\|}{\Delta}, \quad (\text{A.37})$$

where we have used the relations  $Q\dot{P}Q = 0$  and  $P\dot{P} = \dot{P}Q$ . Substituting these bounds in Eq. (A.29), we get

$$T_A \|Q(0)\Omega P(0)\| \leq 2 \frac{\|\dot{P}(0)\|}{\Delta(0)} + 2 \frac{\|\dot{P}(1)\|}{\Delta(1)} + \int_0^1 \left( 4 \frac{\|\dot{P}\|^2}{\Delta} + \frac{\|Q\dot{P}P\|}{\Delta} + \frac{\|\dot{H}\| \cdot \|\dot{P}\|}{\Delta^2} \right) ds. \quad (\text{A.38})$$

Using lemma 8 from [JRS07], we can express  $\|\dot{P}\|$  and  $\|\ddot{P}\|$  in terms of  $H$ , such that

$$\|\dot{P}\| \leq \frac{\|\dot{H}\|}{\Delta}, \quad (\text{A.39})$$

and

$$\|Q\ddot{P}\| \leq \frac{\|\ddot{H}\|}{\Delta} + 4 \frac{\|\dot{H}\|^2}{\Delta^2}, \quad (\text{A.40})$$

and therefore,

$$T_A \|Q(0)\Omega(1)P(0)\| \leq 2 \frac{\|\dot{H}(0)\|}{\Delta^2(0)} + 2 \frac{\|\dot{H}(1)\|}{\Delta^2(1)} + \int_0^1 \left( 9 \frac{\|\dot{H}\|^2}{\Delta^3} + \frac{\|\ddot{H}\|}{\Delta^2} \right) ds. \quad (\text{A.41})$$

It should however be noted here that the bound derived in this manner, is not the optimal bound (see [JRS07] for a tighter bound), but serves to provide a reference. Thus, from Eq. (A.41) we observe that if we choose  $T_A$  such that

$$T_A \geq \frac{1}{\epsilon} \left( 2 \frac{\|\dot{H}(0)\|}{\Delta^2(0)} + 2 \frac{\|\dot{H}(1)\|}{\Delta^2(1)} + \int_0^1 \left( 9 \frac{\|\dot{H}\|^2}{\Delta^3} + \frac{\|\ddot{H}\|}{\Delta^2} \right) ds \right), \quad (\text{A.42})$$

where  $\epsilon$  is an arbitrarily small and positive real number, then,

$$\|Q(0)\Omega(1)P(0)\| \leq \epsilon. \quad (\text{A.43})$$

Returning to the quantity of interest, i.e., the transition probability, we find

$$\begin{aligned} \|Q(s)U(s)P(0)|\psi(0)\rangle\|^2 &\leq \|Q(0)\Omega(1)P(0)\|^2 \\ &\leq \frac{1}{T_A^2} \left( 2 \frac{\|\dot{H}(0)\|}{\Delta^2(0)} + 2 \frac{\|\dot{H}(1)\|}{\Delta^2(1)} + \int_0^1 \left( 9 \frac{\|\dot{H}\|^2}{\Delta^3} + \frac{\|\ddot{H}\|}{\Delta^2} \right) ds \right)^2, \end{aligned} \quad (\text{A.44})$$

which suggests that the transition probability decreases polynomially as the annealing time increases, more specifically as  $\mathcal{O}(T_A^{-2})$ , in agreement with earlier less rigorous qualitative estimates [SO05; MN08].

## Numerical illustration

After having derived a bound on the transition probability, we now go on to perform a numerical study of the dependence of the transition probability on the annealing time. To this end, we choose an instance of a 12-variable 2-SAT problem, and plot the transition probability, given as  $1 - p$ , where  $p$  is the success probability, for annealing times varying between 10 to  $10^5$ .

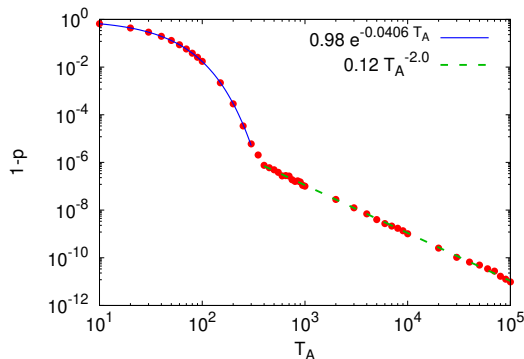


Figure A.1.: Scaling of transition probability  $1 - p$  as a function of annealing time

From Fig. A.1, we note two distinct behaviors of the transition probability as a function of the annealing time. While the transition probability decreases exponentially as the annealing time increases initially, for larger values of the annealing time the transition probability decreases polynomially showing the  $\mathcal{O}(T_A^{-2})$  dependence. The latter result is in agreement with the upper bound derived in Eq. (A.44), indicating that for sufficiently long annealing times the system evolves adiabatically. The exponential part of the scan, on the other hand, is a signature of the Landau-Zener model, where the transition between

the relevant energy levels occurs around the anticrossing between them (see Section 1.3.2). Thus, this result suggests that for these values of the annealing times already, the system can be approximated by a two-level system consisting of the the ground state and the first excited state. Similar observations have also been noted in [SO05; MN08].

It is worth to mention that from a practical point of view, the strict adiabatic regime of annealing, i.e., the regime where the transition probability shows a  $\mathcal{O}(T_A^{-2})$  dependence on the annealing time, is not of much relevance. For most practical applications, a much shorter annealing time, for example the regime for which  $1 - p \approx 10^{-4}$  suffices to yield useful results.

## B. Uniqueness of the ground state of the annealing Hamiltonian

As has been previously established, the minimum energy gap between the relevant energy levels, e.g., the ground state and the first excited state of the annealing Hamiltonian, is a pivotal quantity for the success of the quantum annealing algorithm. This approach is based on the mathematical model of the adiabatic theorem, which mandates the existence of such a minimum energy gap between these levels. However, it is not straightforward to argue in favor of the existence of such a gap. In this section, we provide a discussion, based on [Rus02], to motivate that under the suitable conditions, the ground state of the annealing Hamiltonian can be expected to be unique.

We start with the initial Hamiltonian,  $H_I$ , defined to be

$$H_I = - \sum_{i=1}^N h_i^x \sigma_i^x, \quad (\text{B.1})$$

where generally the  $h_i^x$  are uniformly chosen to be 1. For this section however, we choose a more general initial Hamiltonian, where the  $h_i^x$  can be different, but are all positive. In this case, it is straightforward to argue that the ground state of this Hamiltonian is unique and corresponds to the uniform superposition state, given by

$$|\psi\rangle = |+\rangle_1 |+\rangle_2 \dots |+\rangle_N, \quad (\text{B.2})$$

where

$$|+\rangle_i = \frac{|0\rangle_i + |1\rangle_i}{\sqrt{2}}. \quad (\text{B.3})$$

Another way to confirm the uniqueness of the ground state of the initial Hamiltonian Eq. (B.1) is by considering the operator

$$F = e^{-H_I} = \exp\left(\sum_{i=1}^N h_i^x \sigma_i^x\right) = F_0 \otimes F_1 \otimes \dots \otimes F_{N-1}, \quad (\text{B.4})$$

where

$$F_i = \exp(h_i^x \sigma_i^x) = \frac{1}{2} \begin{pmatrix} 1 & 1 \\ 1 & -1 \end{pmatrix} \begin{pmatrix} e^{h_i x} & 0 \\ 0 & e^{-h_i x} \end{pmatrix} \begin{pmatrix} 1 & 1 \\ 1 & -1 \end{pmatrix} = \begin{pmatrix} \cosh h_i^x & \sinh h_i^x \\ \sinh h_i^x & \cosh h_i^x \end{pmatrix}. \quad (\text{B.5})$$

Since for positive  $h_i^x$ , the matrix elements of  $F_i$  are strictly positive, their tensor product in turn makes the operator  $F$  strictly positive. Then, according to the Perron-Frobenius theorem, the largest eigenvalue of  $F$  should be unique [P07; Fro12]. Since all the  $h_i^x$

are positive, the largest eigenvalue of  $F$  corresponds to the uniform superposition state (Eq. (B.2)), and thus the Perron-Frobenius theorem also implies that the ground state of the initial Hamiltonian is unique.

We now move on to the annealing Hamiltonian with a linear annealing schedule

$$H(s) = (1 - s)H_I + sH_P, \tag{B.6}$$

where  $s$  is the annealing parameter and  $H_P$  is the problem Hamiltonian. Using the Lie-Trotter formula, we have

$$e^{-H} = \lim_{m \rightarrow \infty} (e^{-\frac{s}{m}H_P} e^{-\frac{1-s}{m}H_I})^m. \tag{B.7}$$

Since  $H_P$  is diagonal in the computational basis, the effect of  $\exp(-sH_P/m)$  is to multiply each row of  $\exp(-(1-s)H_I/m)$  by a positive number  $\exp(-s\lambda_i/m)$ , where  $\lambda_i$  are the eigenvalues of  $H_P$ . Thus the product  $\exp(-sH_P/m)\exp(-(1-s)H_I/m)$ , and therefore,  $\exp(-H)$  has non-negative elements. Using the Perron-Frobenius theorem again suggests that the largest eigenvalue of  $\exp(-H)$ , and thus the ground state of the annealing Hamiltonian is unique for  $0 \leq s < 1$ . This argument breaks down at  $s = 1$  since  $\exp(-(1-s)H_I/m) = \mathbb{I}$ , which has zero as the off-diagonal elements. Moreover, the ground state of the problem Hamiltonian can be degenerate. In this case, the energy gap between the ground state and the first excited state tends to zero as  $s \rightarrow 1$ .

## C. Pseudo-code for the Kosaraju-Sharir's algorithm

As discussed in section 1.4.1.1, the Kosaraju-Sharir's algorithm can be used for identifying the strongly-connected components of a 2-SAT problem, which can in turn help in checking whether the given 2-SAT problem is satisfiable, in polynomial time.

Given the implication graph (`graph`) of the 2-SAT problem and its transpose (`graph_transpose`), the Kosaraju-Sharir's algorithm can be implemented as follows [Kog+22].

---

```
def dfs1(i, used, order):
    used[i] = True
    for u in graph[i]:
        if not used[u]:
            dfs1(u, used, order)
    order.append(i)
```

```
def dfs2(v, j, comp):
    comp[v] = j
    for u in graph_transpose[v]:
        if comp[u] == -1:
            dfs2(u, j, comp)
```

```
def solve_2sat():
    order = []
    used = [False] * 2 * n
    comp = [-1] * 2 * n
    assignment = [0] * n
    j = 0

    for i in range(2 * n):
        if not used[i]:
            dfs1(i, used, order)

    for i in range(2 * n):
        v = order[2*n - i - 1]
        if comp[v] == -1:
            dfs2(v, j, comp)
            j += 1
```

```
for i in range(0, 2 * n, 2):
    if comp[i] == comp[i + 1]:
        return False
    else:
        # //2 discards fraction part
        assignment[i // 2] = 1 if comp[i] > comp[i + 1] else 0

assignments.append(assignment)
return True
```

---

## D. Discretizing a quantum Hamiltonian in continuous space

In the main text of the thesis, we have only considered problems represented by finite-dimensional matrices that can be expressed in terms of the Pauli operators. However the general Hamiltonian of a quantum system need not be of this form, and can have continuous degrees of freedom. In this appendix, we discuss how to solve the TDSE (Eq. (1.21)) numerically for quantum systems with Hamiltonians defined over the real space.

A Hamiltonian for a quantum system in real space can be written as

$$H = -\frac{\hbar^2}{2m}\nabla^2 + V(\mathbf{r}, t). \quad (\text{D.1})$$

Restricting to the 1-D case, and setting  $\hbar = m = 1$ , this Hamiltonian becomes

$$H = -\frac{1}{2}\frac{\partial^2}{\partial x^2} + V(x, t). \quad (\text{D.2})$$

For the numerical implementation, we need to discretize the Hamiltonian Eq. (D.2) by using a finite differencing scheme. For simplicity, we restrict ourselves to a regular spaced grid in the range  $x_{min} \leq x \leq x_{max}$ , and divide this interval in  $N_x$  equal spaced sub-intervals, such that

$$\Delta = \frac{x_{max} - x_{min}}{N_x - 1}, \quad (\text{D.3})$$

and  $x = x_{min} + j\Delta$ , where  $j = 0, 1, \dots, N_x - 1$ . We define the wavefunction at time  $t$ ,  $|\psi(t)\rangle$  as

$$|\psi(t)\rangle = \begin{pmatrix} \psi(x_1, t) \\ \psi(x_2, t) \\ \vdots \\ \psi(N_x - 1, t) \end{pmatrix}. \quad (\text{D.4})$$

Then, the second-order derivative of the wave function can be approximated as

$$\frac{\partial^2}{\partial x^2}\psi(x, t) \approx \frac{\psi(x + \Delta, t) - 2\psi(x, t) + \psi(x - \Delta, t)}{\Delta^2}, \quad (\text{D.5})$$

where  $x = x_{min} + j\Delta$ , and thus  $V(x, t) = V(x_{min} + j\Delta, t) \equiv V_j$ . At each point of time, the instantaneous Hamiltonian is a tridiagonal matrix of the form

$$H(t) = \Delta^{-2} \begin{pmatrix} 1 + \Delta^2 V_0 & -1/2 & 0 & 0 & & 0 \\ -1/2 & 1 + \Delta^2 V_1 & -1/2 & 0 & \dots & 0 \\ 0 & -1/2 & 1 + \Delta^2 V_2 & 0 & & 0 \\ \vdots & & & \ddots & & \\ 0 & \dots & & 0 & 1 + \Delta^2 V_{N_x-2} & -1/2 \\ 0 & & & 0 & -1/2 & 1 + \Delta^2 V_{N_x-1} \end{pmatrix}. \quad (\text{D.6})$$

Thus, the TDSE becomes

$$i \frac{\partial}{\partial t} |\psi(t)\rangle = \Delta^{-2} \begin{pmatrix} 1 + \Delta^2 V_0 & -1/2 & 0 & & & 0 \\ -1/2 & 1 + \Delta^2 V_1 & -1/2 & & & \\ 0 & -1/2 & 1 + \Delta^2 V_2 & & & \\ & & & \ddots & & 0 \\ & & & & 1 + \Delta^2 V_{N_x-2} & -1/2 \\ 0 & & & & 0 & -1/2 & 1 + \Delta^2 V_{N_x-1} \end{pmatrix} |\psi(t)\rangle \quad (\text{D.7})$$

As will become clear from Section 2.2, for a small time step  $\tau$ , the solution to Eq. (D.7) can be approximated as

$$|\psi(t + \tau)\rangle \approx e^{-i\tau H(t+\tau/2)} |\psi(t)\rangle. \quad (\text{D.8})$$

There are various ways in which Eq. (D.8) can be solved. Adopting the Suzuki-Trotter product formula algorithm (see Section 2.2.2) for computing approximations to this exponential, by decomposing the Hamiltonian in suitable Hamiltonian terms could be one of the convenient choices for this. Using this approach, it is possible to implement the TDSE without having to discretize the time derivative, and use the formal solution given by Eq. (D.8).

## E. Error bounds

In this appendix, we derive the bounds on the error that results from approximating the time evolution using, for example, the Crank-Nicolson algorithm and the Suzuki-Trotter product formula algorithm discussed in chapter 2. These proofs are based on [De 87].

### E.1. Crank-Nicolson algorithm

We start by computing the error involved in employing the Crank-Nicolson method for implementing the time evolution of the state of a quantum mechanical system. Put differently, we wish to calculate  $\|U(\tau) - U_{CN}(\tau)\| = \|e^{-i\tau H} - (1 + iH\tau/2)^{-1}(1 - iH\tau/2)\|$  (see Eq. (2.23)). For this, we define

$$\begin{aligned} F(\tau) &= 1 - U(\tau)^{-1}U_{CN}(\tau) \\ &= 1 - e^{i\tau H} \left(1 + \frac{iH\tau}{2}\right)^{-1} \left(1 - \frac{iH\tau}{2}\right). \end{aligned} \quad (\text{E.1})$$

Differentiating Eq. (E.1) with respect to  $\tau$  gives

$$\frac{\partial F(\tau)}{\partial \tau} = -\frac{iH^3\tau^2}{4} e^{i\tau H} \left(1 + \frac{iH\tau}{2}\right)^{-2}. \quad (\text{E.2})$$

Noting that  $F(0) = 0$ , integration of Eq. (E.2) over  $\tau$  yields,

$$F(\tau) = -\frac{iH^3}{4} \int_0^\tau d\lambda \lambda^2 e^{i\lambda H} \left(1 + \frac{iH\lambda}{2}\right)^{-2}. \quad (\text{E.3})$$

Multiplying by  $e^{-i\tau H}$  on both sides, we obtain

$$\|e^{-i\tau H} - (1 + iH\tau/2)^{-1}(1 - iH\tau/2)\| \leq \frac{1}{4} \int_0^\tau d\lambda \lambda^2 \left\| H^3 e^{i(\lambda-\tau)H} \left(1 + \frac{iH\lambda}{2}\right)^{-2} \right\|, \quad (\text{E.4})$$

where  $\|\cdot\|$  denotes the norm of the involved quantity. Since  $\|e^{i(\lambda-\tau)H}\| = 1$  and  $\|(1 + i\lambda H/2)^{-1}\| \leq 1$ ,

$$\|U(\tau) - (+iH\tau/2)^{-1}(1 - iH\tau/2)\| \leq \frac{\|H^3\|\tau^3}{12}. \quad (\text{E.5})$$

Since for matrices  $X$  and  $Y$  we have  $\|X^m - Y^m\| \leq \sum_{n=0}^{m-1} \|X - Y\| \|X\|^n \|Y\|^{m-n-1}$ , in case of unitary matrices  $X$  and  $Y$ ,  $\|X^m - Y^m\| \leq m\|X - Y\|$ . Thus, the accumulated error for  $m$  applications of the method reads

$$\|U(\tau)^m - U_{CN}(\tau)^m\| \leq m \frac{\|H^3\|\tau^3}{12} = \frac{t\|H\|^3\tau^2}{12}. \quad (\text{E.6})$$

## E.2. Suzuki-Trotter product formula algorithm

Next, following the proof in [De 87], we compute the bounds on the error involved in approximating the time evolution operator using the first- and the second-order product formula algorithm.

### E.2.1. First-order approximation

Assuming the Hamiltonian to be independent of time, we obtain a measure for  $\|e^{-i\tau H} - \prod_{k=1}^K e^{-i\tau H_k}\|$ . Considering first the case where the Hamiltonian is expressed as a sum of two matrices, we define the operator  $F(\lambda) = 1 - e^{\lambda A} e^{\lambda B} e^{-\lambda(A+B)}$ , where  $A = -iH_1$  and  $B = -iH_2$ . Differentiating  $F(\lambda)$  with respect to  $\lambda$ , we obtain

$$\frac{\partial F}{\partial \lambda} = e^{\lambda A} [e^{\lambda B}, A] e^{-\lambda(A+B)}. \quad (\text{E.7})$$

Furthermore, we have

$$[A, e^{\lambda B}] = \int_0^\lambda d\mu e^{(\lambda-\mu)B} [A, B] e^{\mu B} = \int_0^\lambda d\mu e^{\mu B} [A, B] e^{(\lambda-\mu)B}, \quad (\text{E.8})$$

and thus

$$\frac{\partial F}{\partial \lambda} = - \int_0^\lambda d\mu e^{\lambda A} e^{\mu B} [A, B] e^{(\lambda-\mu)B} e^{-\lambda(A+B)}. \quad (\text{E.9})$$

As  $F(0) = 0$ , integrating Eq. (E.9) results in

$$F(\tau) = - \int_0^\tau d\lambda \int_0^\lambda d\mu e^{\lambda A} e^{\mu B} [A, B] e^{(\lambda-\mu)B} e^{-\lambda(A+B)}. \quad (\text{E.10})$$

Therefore,

$$e^{\tau(A+B)} - e^{\tau A} e^{\tau B} = - \int_0^\tau d\lambda \int_0^\lambda d\mu e^{\lambda A} e^{\mu B} [A, B] e^{(\lambda-\mu)B} e^{(\tau-\lambda)(A+B)}. \quad (\text{E.11})$$

Substituting the definitions of  $A$  and  $B$  gives

$$\|e^{\tau(A+B)} - e^{\tau A} e^{\tau B}\| \leq \frac{\tau^2}{2} \|[A, B]\|, \quad (\text{E.12})$$

and similarly for the general case where  $H = \sum_{k=1}^K H_k$ ,

$$\|U(\tau) - \tilde{U}_1(\tau)\| = \|e^{-i\tau H} - \prod_{k=1}^K e^{-i\tau H_k}\| \leq \frac{\tau^2}{2} \sum_{1 \leq k < k' \leq K} \|[H_k, H_{k'}]\|. \quad (\text{E.13})$$

Thus, the error involved in  $m$  applications of the first-order approximation to the time evolution operator gives

$$\|U(\tau)^m - \tilde{U}_1(\tau)^m\| \leq \frac{\tau t}{2} \sum_{1 \leq k < k' \leq K} \|[H_k, H_{k'}]\|. \quad (\text{E.14})$$

## E.2.2. Second-order approximation

Moving now to the second-order approximation, we once again assume the case where the Hamiltonian is expressed as a sum of two matrices  $A$  and  $B$  introduced in the previous section.

As before, we define  $F(\lambda) = 1 - e^{\lambda A/2} e^{\lambda B} e^{\lambda A/2} e^{-\lambda(A+B)}$ , the derivative of which with respect to  $\lambda$  yields

$$\frac{\partial F}{\partial \lambda} = e^{\lambda A/2} e^{\lambda B} G(\lambda) e^{\lambda A/2} e^{-\lambda(A+B)}, \quad (\text{E.15})$$

where

$$G(\lambda) = \frac{1}{2} e^{-\lambda B} [e^{\lambda B}, A] + [e^{\lambda A/2}, B] e^{-\lambda A/2}. \quad (\text{E.16})$$

Making use of Eq. (E.8), we obtain

$$G(\lambda) = -\frac{1}{2} \int_0^\lambda d\mu e^{(\mu-\lambda)B} [A, B] e^{(\lambda-\mu)B} - \frac{1}{2} \int_0^\lambda d\mu e^{(\lambda-\mu)A/2} [B, A] e^{(\mu-\lambda)A/2}. \quad (\text{E.17})$$

Substituting Eq. (E.17) in Eq. (E.15) and integrating while noting  $F(0) = 0$ , we find

$$F(\tau) = -\frac{1}{2} \int_0^\tau d\lambda \int_0^\lambda d\mu e^{\lambda A/2} (e^{\mu B} [A, B] e^{(\lambda-\mu)B} e^{\lambda A/2} + e^{\lambda B} e^{(\lambda-\mu)A/2} [B, A] e^{\mu A/2}) e^{-\lambda(A+B)}, \quad (\text{E.18})$$

and thus,

$$\|e^{-i\tau H} - e^{-i\tau H_1/2} e^{-i\tau H_2} e^{-i\tau H_1/2}\| \leq \frac{\tau^2}{4} (\|[H_1, H_2]\| + \|[H_2, H_1]\|) = c_1 \tau^2, \quad (\text{E.19})$$

where  $c_1 = \|[H_1, H_2]\|/2$ . However, for a small  $\tau$ , the  $\mathcal{O}(\tau^0)$  terms in the integrand vanish in Eq. (E.18) (using Taylor expansion of the involved exponents), and hence it is possible to obtain an even tighter bound by doubly differentiating Eq. (E.16) with respect to  $\lambda$  to obtain

$$\frac{\partial G}{\partial \lambda} = \frac{1}{2} (e^{-\lambda B} [B, A] e^{\lambda B} + e^{\lambda A/2} [A, B] e^{-\lambda A/2}), \quad (\text{E.20})$$

and

$$\frac{\partial^2 G}{\partial \lambda^2} = \frac{1}{2} e^{-\lambda B} [B, [A, B]] e^{\lambda B} + \frac{1}{4} e^{\lambda A/2} [A, [A, B]] e^{-\lambda A/2}. \quad (\text{E.21})$$

Since  $G(0) = \partial G / \partial \lambda|_{\lambda=0} = 0$ , doubly integrating Eq. (E.21) gives

$$G(\lambda) = \int_0^\lambda d\mu \int_0^\mu d\nu \left( \frac{1}{2} e^{-\nu B} [B, [A, B]] e^{\nu B} + \frac{1}{4} e^{\nu A/2} [A, [A, B]] e^{-\nu A/2} \right). \quad (\text{E.22})$$

Substituting Eq. (E.22) in Eq. (E.15) yields

$$F(\tau) = \frac{1}{4} \int_0^\tau d\lambda \int_0^\lambda d\mu \int_0^\mu d\nu (e^{-\nu B} [2B, [A, B]] e^{\nu B} + e^{\nu A/2} [A, [A, B]] e^{-\nu A/2}), \quad (\text{E.23})$$

and therefore,

$$\|e^{-i\tau H} - e^{-i\tau H_1/2} e^{-i\tau H_2} e^{-i\tau H_1/2}\| \leq c_2 \tau^3, \quad (\text{E.24})$$

where  $c_2 = (\|[2H_2, [H_1, H_2]]\| + \|[H_1, [H_1, H_2]]\|)/24$ .

Generalizing to the case of the decomposition in  $K$  parts, we have

$$\|e^{-i\tau H} - \prod_{k=1}^K e^{-i\tau H_k}\| \leq c_3 \tau^3, \quad (\text{E.25})$$

for some constant  $c_3$ . Therefore, the accumulated error involved for a total of  $m$  applications becomes

$$\|U(\tau)^m - \tilde{U}_2(\tau)^m\| \leq m c_3 \tau^3 = c_3 \tau^2 t. \quad (\text{E.26})$$

## F. Quantum simulation

As was discussed in Chapter 1, it has been conjectured that quantum systems cannot be simulated efficiently on classical computers [Fey82]. However, the ability of performing such quantum simulations can offer valuable insights in the understanding of various physical phenomena like superconductivity, magnetism, and many more [NC10]. In the present section, we discuss how the Suzuki-Trotter product formula algorithm can be employed for studying the evolution of a quantum system on a quantum computer.

The dynamics of a quantum system is governed by the TDSE, the solution to which could be approximated by the exponentials of the form  $\exp(-i\tau H(t + \tau/2))$  for a system evolving from time  $t$  to  $t + \tau$ . The Hamiltonian matrix  $H$  can then be decomposed into Hamiltonian matrices  $H_k$  consisting of only local terms (see Eq. (2.26)). At this point, the second-order Suzuki-Trotter product formula algorithm (see Eq. (2.29)) can be used for carrying out the evolution on a quantum computer as follows. We start with the general Hamiltonian given by Eq. (2.36) and decompose it as

$$H(t) = H_x + H_y + H_z + H_{xx} + H_{yy} + H_{zz}, \quad (\text{F.1})$$

where  $H_\alpha = A(t) \sum_{i=0}^N h_i^\alpha \sigma_i^\alpha$  for  $\alpha = x, y, z$ , and  $H_{xx}$ ,  $H_{yy}$ , and  $H_{zz}$  are defined as before.

Using the gate-based model of quantum computing, it is straightforward to implement  $\exp(i\tau H_\alpha)$  using the rotation gates given by Eq. (1.12) for  $\alpha = x, y, z$ . We therefore move to the contributions from the Hamiltonian terms with higher-order coupling terms, and start with implementation of the  $\exp(-i\tau H_{zz})$ . This operation can be carried out using the CNOT gate and an ancillary qubit initialized in the state  $|0\rangle$  as shown in Fig. F.1 [NC10].

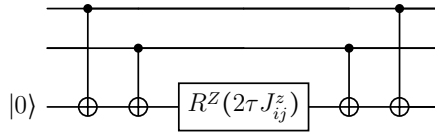


Figure F.1.: Quantum circuit for implementing  $\exp(-i\tau J_{ij}^z \sigma_i^z \sigma_j^z)$  on a quantum computer.

For the contributions arising from the  $H_{xx}$  and  $H_{yy}$  terms, we can start by applying rotation gates  $R^y(\pi/2)$  and  $(R^x(\pi/2))^\dagger$ , respectively, on all the input qubits, and then proceeding in the same manner as for the  $H_{zz}$  term. The resulting state can then be transformed back to the computational basis by applying the inverse rotations  $(R^y(\pi/2))^\dagger$  and  $R^x(\pi/2)$ , on all the input qubits.

It is straightforward to see that using this approach it is possible to implement quantum Hamiltonians with higher-order couplings. However, this procedure requires the use of

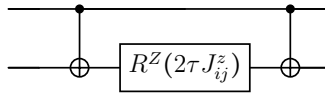


Figure F.2.: An alternative quantum circuit for implementing  $\exp(-i\tau J_{ij}^z \sigma_i^z \sigma_j^z)$  on a quantum computer.

an ancillary qubit. An alternative circuit for simulating  $\exp(-i\tau H_{zz})$ , without using an ancillary qubit is shown in Fig. F.2. As before, the contributions from the  $H_{xx}$  and  $H_{yy}$  terms can be implemented using the rotation gates.

## G. Distributions

In this appendix, we provide the distributions that have been used in chapter 6 to fit the minimum energy gap  $\Delta_{min}$  or the correlation length defined as  $\xi = 1/\Delta_{min}$ .

The first is the Fréchet distribution given by

$$F_k(x) = a \left( \frac{b}{x} \right)^{k+1} e^{-\left(\frac{b}{x}\right)^k}, \quad (\text{G.1})$$

for constants  $a$ ,  $b$ , and  $k$ .

Next, we move to the Weibull-distribution, defined as

$$W_k(x) = a \left( \frac{x}{b} \right)^{k-1} e^{-\left(\frac{x}{b}\right)^k}. \quad (\text{G.2})$$

Introducing a translation  $\mu$  in the Weibull distribution leads to the translated-Weibull distribution given by

$$W_k(x) = a \left( \frac{x-\mu}{b} \right)^{k-1} e^{-\left(\frac{x-\mu}{b}\right)^k}. \quad (\text{G.3})$$

Lastly, we define the transformed-translated distribution  $\widetilde{W}_k(y)$  for the variable  $y = 1/x$ , where  $x$  follows the translated-Weibull distribution,  $|\partial x/\partial y| = 1/y^2$  is the Jacobian of the transformation, and

$$\widetilde{W}_k(y) = a(1-\mu y)^{-2} \left( \frac{1-\mu y}{by} \right)^{k+1} e^{-\left(\frac{1-\mu y}{by}\right)^k}. \quad (\text{G.4})$$



# Bibliography

- [ACd89] B. Apolloni, C. Carvalho, and D. de Falco. “Quantum stochastic optimization”. *Stoch. Process. Their Appl.* 33 (1989), 233–244. DOI: 10.1016/0304-4149(89)90040-9 (cit. on p. 2).
- [Aha+07] D. Aharonov, W. van Dam, J. Kempe, Z. Landau, S. Lloyd, and O. Regev. “Adiabatic Quantum Computation is Equivalent to Standard Quantum Computation”. *SIAM J. Comput.* 37 (2007), 166–194. DOI: 10.1137/S0097539705447323 (cit. on p. 7).
- [AHY20] A. Ajagekar, T. Humble, and F. You. “Quantum computing based hybrid solution strategies for large-scale discrete-continuous optimization problems”. *Comput. Chem. Eng.* 132 (2020), 106630. DOI: 10.1016/j.compchemeng.2019.106630 (cit. on p. 1).
- [AL18a] T. Albash and D. A. Lidar. “Adiabatic quantum computation”. *Rev. Mod. Phys.* 90 (1 2018), 015002. DOI: 10.1103/RevModPhys.90.015002 (cit. on pp. 73, 81).
- [AL18b] T. Albash and D. A. Lidar. “Demonstration of a Scaling Advantage for a Quantum Annealer over Simulated Annealing”. *Phys. Rev. X* 8 (3 2018), 031016. DOI: 10.1103/PhysRevX.8.031016 (cit. on pp. 1, 81).
- [Alb19] T. Albash. “Role of nonstoquastic catalysts in quantum adiabatic optimization”. *Phys. Rev. A* 99 (4 2019), 042334. DOI: 10.1103/PhysRevA.99.042334 (cit. on pp. 63, 64).
- [Ami09] M. H. Amin. “Consistency of the adiabatic theorem”. *Phys. Rev. Lett.* 102 (22 2009), 220401. DOI: 10.1103/PhysRevLett.102.220401 (cit. on p. 8).
- [Ami15] M. H. Amin. “Searching for quantum speedup in quasistatic quantum annealers”. *Phys. Rev. A* 92 (5 2015), 052323. DOI: 10.1103/PhysRevA.92.052323 (cit. on p. 29).
- [Bar82] F. Barahona. “On the computational complexity of Ising spin glass models”. *Journal of Physics A: Mathematical and General* 15 (1982), 3241. DOI: 10.1088/0305-4470/15/10/028 (cit. on p. 15).
- [Ben80] P. Benioff. “The computer as a physical system: A microscopic quantum mechanical Hamiltonian model of computers as represented by Turing machines”. *J. Stat. Phys.* 22 (1980), 563–591. DOI: 10.1007/BF01011339 (cit. on p. 1).
- [BF28] M. Born and V. Fock. “Beweis des Adiabatensatzes”. *Z. Phys.* 51 (1928), 165–180. DOI: 10.1007/BF01343193 (cit. on p. 7).

- [BGM21] F. Bova, A. Goldfarb, and R. G. Melko. “Commercial applications of quantum computing”. *EPJ Quantum Technol.* 8 (2021), 2. DOI: 10.1140/epjqt/s40507-021-00091-1 (cit. on p. 1).
- [BL08] J. D. Biamonte and P. J. Love. “Realizable Hamiltonians for universal adiabatic quantum computers”. *Phys. Rev. A* 78 (1 2008), 012352. DOI: 10.1103/PhysRevA.78.012352 (cit. on p. 7).
- [Boi+14] S. Boixo, T. F. Rønnow, S. V. Isakov, Z. Wang, D. Wecker, D. A. Lidar, J. M. Martinis, and M. Troyer. “Evidence for quantum annealing with more than one hundred qubits”. *Nat. Phys.* 10 (2014), 218–224. DOI: 10.1038/nphys2900 (cit. on pp. 1, 81, 88).
- [Bro+99] J. Brooke, D. Bitko, T. F., null Rosenbaum, and G. Aeppli. “Quantum Annealing of a Disordered Magnet”. *Science* 284 (1999), 779–781. DOI: 10.1126/science.284.5415.779 (cit. on pp. 2, 81).
- [Bun+14a] P. I. Bunyk et al. “Architectural Considerations in the Design of a Superconducting Quantum Annealing Processor”. *IEEE Transactions on Applied Superconductivity* 24 (2014), 1–10. DOI: 10.1109/TASC.2014.2318294 (cit. on p. 29).
- [Bun+14b] P. I. Bunyk et al. “Architectural considerations in the design of a superconducting quantum annealing processor”. *IEEE Transactions on Applied Superconductivity* 24 (2014). DOI: 10.1109/TASC.2014.2318294 (cit. on p. 30).
- [BV97] E. Bernstein and U. Vazirani. “Quantum Complexity Theory”. *SIAM J. Comput.* 26 (1997), 1411–1473. DOI: 10.1137/S0097539796300921 (cit. on p. 1).
- [Cha17] N. Chancellor. “Modernizing quantum annealing using local searches”. *New J. Phys.* 19 (2017), 023024. DOI: 10.1088/1367-2630/aa59c4 (cit. on p. 43).
- [Cha20] N. Chancellor. “Fluctuation-guided search in quantum annealing”. *Phys. Rev. A* 102 (6 2020), 062606. DOI: 10.1103/PhysRevA.102.062606 (cit. on p. 63).
- [Chi+03] A. M. Childs, R. Cleve, E. Deotto, E. Farhi, S. Gutmann, and D. A. Spielman. “Exponential Algorithmic Speedup by a Quantum Walk”. In: *Proceedings of the Thirty-Fifth Annual ACM Symposium on Theory of Computing*. STOC '03. San Diego, CA, USA: Association for Computing Machinery, 2003, 59–68. ISBN: 1581136749. DOI: 10.1145/780542.780552 (cit. on p. 73).
- [Chi17] A. M. Childs. “Lecture notes on quantum algorithms”. *Lecture notes at University of Maryland* (2017) (cit. on p. 114).
- [CL21] E. J. Crosson and D. A. Lidar. “Prospects for quantum enhancement with diabatic quantum annealing”. *Nat. Rev. Phys.* (2021), 1–24. DOI: 10.1038/s42254-021-00313-6 (cit. on p. 81).

- [Cla+19] J. Clark, T. West, J. Zammit, X. Guo, L. Mason, and D. Russell. “Towards Real Time Multi-Robot Routing Using Quantum Computing Technologies”. In: *Proceedings of the International Conference on High Performance Computing in Asia-Pacific Region*. HPC Asia 2019. Guangzhou, China: Association for Computing Machinery, 2019, 111–119. ISBN: 9781450366328. DOI: 10.1145/3293320.3293333 (cit. on p. 3).
- [CN47] J. Crank and P. Nicolson. “A practical method for numerical evaluation of solutions of partial differential equations of the heat-conduction type”. *Math. Proc. Camb. Philos. Soc.* 43 (1947), 50–67. DOI: 10.1017/S0305004100023197 (cit. on p. 21).
- [Cor+22] B. A. Cordier, N. P. D. Sawaya, G. G. Guerreschi, and S. K. McWeeney. “Biology and medicine in the landscape of quantum advantages”. *J. R. Soc. Interface* 19 (2022), 20220541. DOI: 10.1098/rsif.2022.0541 (cit. on p. 1).
- [Cro+14] E. Crosson, E. Farhi, C. Y. Lin, H. Lin, and P. Shor. “Different strategies for optimization using the quantum adiabatic algorithm”. *arXiv preprint arXiv:1401.7320* (2014). DOI: 10.48550/arXiv.1401.7320 (cit. on pp. 63, 72, 88).
- [Cro+20] E. Crosson, T. Albash, I. Hen, and A. P. Young. “De-Signing Hamiltonians for Quantum Adiabatic Optimization”. *Quantum* 4 (2020), 334. DOI: 10.22331/q-2020-09-24-334 (cit. on p. 64).
- [CW02] J. K. Cullum and R. A. Willoughby. *Lanczos algorithms for large symmetric eigenvalue computations: Vol. I: Theory*. SIAM Philadelphia, 2002. DOI: 10.1137/1.9780898719192 (cit. on p. 25).
- [CWM21] C. D. G. Calaza, D. Willsch, and K. Michielsen. “Garden optimization problems for benchmarking quantum annealers”. *Quantum Information Processing* 20 (2021), 1–22. DOI: 10.1007/s11128-021-03226-6 (cit. on p. 1).
- [D-W] D-Wave. *Leap Docs*. Tech. rep. Tech. Rep.(D-Wave Systems Inc, Burnaby, BC, Canada, 2020) (cit. on p. 30).
- [DBM21] H. Daniel, O. Benjamin, and R. Matthias. “Anomaly detection with variational quantum generative adversarial networks”. *Quantum Sci. Technol.* 6 (2021), 045004. DOI: 10.1088/2058-9565/ac0d4d (cit. on p. 1).
- [DD03] V. V. Dobrovitski and H. De Raedt. “Efficient scheme for numerical simulations of the spin-bath decoherence”. *Phys. Rev. E* . 67 (2003), 056702. DOI: 10.1103/PhysRevE.67.056702 (cit. on p. 21).
- [DD83] H. De Raedt and B. De Raedt. “Applications of the generalized Trotter formula”. *Physical Review A* 28 (1983), 3575. DOI: 10.1103/PhysRevA.28.3575 (cit. on pp. 22, 23).
- [De +23] H. De Raedt, M. I. Katsnelson, M. S. Jattana, V. Mehta, M. Willsch, D. Willsch, K. Michielsen, and F. Jin. “Einstein–Podolsky–Rosen–Bohm experiments: A discrete data driven approach”. *Annals of Physics* 453 (2023), 169314. ISSN: 0003-4916. DOI: 10.1016/j.aop.2023.169314.

- [De +97] H. De Raedt, S. Miyashita, K. Saito, D. García-Pablos, and N. García. “Theory of quantum tunneling of the magnetization in magnetic particles”. *Phys. Rev. B* 56 (18 1997), 11761–11768. DOI: 10.1103/PhysRevB.56.11761 (cit. on p. 8).
- [De 87] H. De Raedt. “Product formula algorithms for solving the time dependent Schrödinger equation”. *Comput. Phys. Rep.* 7 (1987), 1–72. DOI: 10.1016/0167-7977(87)90002-5 (cit. on pp. 21, 22, 127, 128).
- [Deu85] D. Deutsch. “Quantum theory, the Church–Turing principle and the universal quantum computer”. *Proc. R. Soc. Lond. A* 400 (1985), 97–117. DOI: 10.1098/rspa.1985.0070 (cit. on p. 1).
- [Dev16] S. J Devitt. “Performing quantum computing experiments in the cloud”. *Phys. Rev. A* 94 (2016), 032329. DOI: 10.1103/PhysRevA.94.032329 (cit. on p. 1).
- [Dic+13] N. G. Dickson et al. “Thermally assisted quantum annealing of a 16-qubit problem”. *Nat. Commun.* 4 (2013), 1–6. DOI: 10.1038/ncomms2920 (cit. on p. 2).
- [DJ92] D. Deutsch and R. Jozsa. “Rapid solution of problems by quantum computation”. *Proc. R. Soc. Lond. A* 439 (1992), 553–558. DOI: 10.1098/rspa.1992.0167 (cit. on p. 1).
- [EGS11] S. Ermon, C. P. Gomes, and B. Selman. “A Flat Histogram Method for Computing the Density of States of Combinatorial Problems”. In: *IJCAI*. 2011 (cit. on p. 11).
- [Far+00] E. Farhi, J. Goldstone, S. Gutmann, and M. Sipser. “Quantum computation by adiabatic evolution”. *arXiv:quant-ph/0001106* (2000). DOI: 10.48550/arXiv.quant-ph/0001106 (cit. on p. 2).
- [Far+01] E. Farhi, J. Goldstone, S. Gutmann, J. Lapan, A. Lundgren, and D. Preda. “A quantum adiabatic evolution algorithm applied to random instances of an NP-complete problem”. *Science* 292 (2001), 472–475. DOI: 10.48550/arXiv.quant-ph/0104129 (cit. on p. 2).
- [Far+09] E. Farhi, J. Goldstone, D. Gosset, S. Gutmann, H. B. Meyer, and P. Shor. “Quantum adiabatic algorithms, small gaps, and different paths”. *arXiv preprint arXiv:0909.4766* (2009). DOI: 10.48550/arXiv.0909.4766 (cit. on p. 63).
- [Fel+19] S. Feld, C. Roch, T. Gabor, C. Seidel, F. Neukart, I. Galter, W. Mauerer, and C. Linnhoff-Popien. “A Hybrid Solution Method for the Capacitated Vehicle Routing Problem Using a Quantum Annealer”. *Frontiers in ICT* 6 (2019). DOI: 10.3389/fict.2019.00013 (cit. on p. 3).
- [Fey82] R. P. Feynman. “Simulating physics with computers”. *Int. J. Theor. Phys.* 6 (1982), 467–488. DOI: 10.1007/BF02650179 (cit. on pp. 1, 131).

- [FGG02] E. Farhi, J. Goldstone, and S. Gutmann. “Quantum adiabatic evolution algorithms with different paths”. *arXiv preprint quant-ph/0208135* (2002). DOI: 10.48550/arXiv.quant-ph/0208135 (cit. on p. 63).
- [Fin+94] A. B. Finnila, M. A. Gomez, C. Sebenik, C. Stenson, and Jimmie D. Doll. “Quantum annealing: A new method for minimizing multidimensional functions”. *Chem. Phys. Lett.* 219 (1994), 343–348. DOI: 10.1016/0009-2614(94)00117-0 (cit. on p. 2).
- [Fro12] G. Frobenius. *Über Matrizen aus nicht negativen Elementen*. Preuss. Akad. Wiss., Berlin. 1912, 456–477 (cit. on p. 121).
- [GH20] L. Gupta and I. Hen. “Elucidating the Interplay between Non-Stoquasticity and the Sign Problem”. *Adv. Quantum Technol.* 3 (2020), 1900108. DOI: 10.1002/qute.201900108 (cit. on p. 63).
- [Gro96] L. K. Grover. “A fast quantum mechanical algorithm for database search”. In: *Proceedings of the Twenty-Eighth Annual ACM Symposium on Theory of Computing*. 1996. DOI: 10.1145/237814.237866 (cit. on p. 1).
- [Gro97] L. K. Grover. “Quantum Mechanics Helps in Searching for a Needle in a Haystack”. *Phys. Rev. Lett.* 79 (2 1997), 325–328. DOI: 10.1103/PhysRevLett.79.325 (cit. on p. 1).
- [GV96] G. H. Golub and C. F. Van Loan. “Matrix computations”. *Johns Hopkins University Press, 3rd edition* (1996) (cit. on pp. 21, 25).
- [Har+10] R. Harris et al. “Experimental investigation of an eight-qubit unit cell in a superconducting optimization processor”. *Phys. Rev. B* 82 (2 2010), 024511. DOI: 10.1103/PhysRevB.82.024511 (cit. on p. 29).
- [Hau+20] P. Hauke, H. G. Katzgraber, W. Lechner, H. Nishimori, and W. D. Oliver. “Perspectives of quantum annealing: Methods and implementations”. *Reports on Progress in Physics* 83 (2020), 054401. DOI: 10.1088/1361-6633/ab85b8 (cit. on p. 81).
- [Hen+15] I. Hen, J. Job, T. Albash, T. F. Rønnow, M. Troyer, and D. A. Lidar. “Probing for quantum speedup in spin-glass problems with planted solutions”. *Phys. Rev. A* 92 (4 2015), 042325. DOI: 10.1103/PhysRevA.92.042325 (cit. on p. 81).
- [Hor+17] L. Hormozi, E. W. Brown, G. Carleo, and M. Troyer. “Nonstoquastic Hamiltonians and quantum annealing of an Ising spin glass”. *Phys. Rev. B* 95 (18 2017), 184416. DOI: 10.1103/PhysRevB.95.184416 (cit. on pp. 63, 64, 79, 85, 88).
- [Hou13] A. S. Householder. *The theory of matrices in numerical analysis*. Courier Corporation, 2013. DOI: 10.1137/1008032 (cit. on p. 26).

- [Hsu+19] T. Hsu, F. Jin, C. Seidel, F. Neukart, H. De Raedt, and K. Michielsen. “Quantum Annealing with Anneal Path Control: Application to 2-SAT Problems with Known Energy Landscapes”. *Commun. Comput. Phys.* 26 (2019), 928–946. DOI: <https://doi.org/10.4208/cicp.0A-2018-0257> (cit. on pp. 63, 81).
- [Ino+21] D. Inoue, A. Okada, T. Matsumori, K. Aihara, and H. Yoshida. “Traffic signal optimization on a square lattice with quantum annealing”. *Sci. Rep.* 11 (2021), 1–12. DOI: [10.1038/s41598-021-82740-0](https://doi.org/10.1038/s41598-021-82740-0) (cit. on p. 3).
- [Joh+10] M. W. Johnson et al. “A scalable control system for a superconducting adiabatic quantum optimization processor”. *Superconductor Science and Technology* 23 (2010), 065004. DOI: [10.1088/0953-2048/23/6/065004](https://doi.org/10.1088/0953-2048/23/6/065004) (cit. on p. 29).
- [JRS07] S. Jansen, M. B. Ruskai, and R. Seiler. “Bounds for the adiabatic approximation with applications to quantum computation”. *J. Math. Phys.* 48 (2007), 102111. DOI: [10.1063/1.2798382](https://doi.org/10.1063/1.2798382) (cit. on pp. 114, 115, 118).
- [JS94] N.N. Bogolyubov (Jr.) and D.P. Sankovich. “N. N. Bogolyubov and statistical mechanics”. *Russian Math. Surveys* 49 (1994), 19–49. DOI: [10.1070/RM1994v049n05ABEH002419](https://doi.org/10.1070/RM1994v049n05ABEH002419) (cit. on p. 10).
- [Jül19] Jülich Supercomputing Centre. “JUWELS: Modular Tier-0/1 Supercomputer at the Jülich Supercomputing Centre”. *Journal of large-scale research facilities* 5 (2019). DOI: [10.17815/jlsrf-5-171](https://doi.org/10.17815/jlsrf-5-171) (cit. on p. 11).
- [Kat50] T. Kato. “On the adiabatic theorem of quantum mechanics”. *J. Phys. Soc. Japan* 5 (1950), 435–439. DOI: [10.1143/JPSJ.5.435](https://doi.org/10.1143/JPSJ.5.435) (cit. on p. 7).
- [KGV83] S. Kirkpatrick, D. Gelatt, and M. P. Vecchi. “Optimization by Simulated Annealing”. *Science* 220 (1983), 671–680. DOI: [10.1126/science.220.4598.671](https://doi.org/10.1126/science.220.4598.671) (cit. on p. 2).
- [Kin+15] J. King, S. Yarkoni, M. M. Nevisi, J. P. Hilton, and C. C. McGeoch. “Benchmarking a quantum annealing processor with the time-to-target metric”. *arXiv:1508.05087* (2015). DOI: [10.48550/arXiv.1508.05087](https://doi.org/10.48550/arXiv.1508.05087) (cit. on p. 81).
- [Kin+18] A. D. King et al. “Observation of topological phenomena in a programmable lattice of 1,800 qubits”. *Nature* 560 (2018), 456–460. DOI: [10.1038/s41586-018-0410-x](https://doi.org/10.1038/s41586-018-0410-x) (cit. on p. 43).
- [KN98] T. Kadowaki and H. Nishimori. “Quantum annealing in the transverse Ising model”. *Phys. Rev. E* 58 (5 1998), 5355–5363. DOI: [10.1103/PhysRevE.58.5355](https://doi.org/10.1103/PhysRevE.58.5355) (cit. on p. 2).
- [Kog+22] J. Kogler, O. Kulkov, J. Sharma, V. Sharma, B. Shi, Aryaman, and T. Khullar. *2-SAT*. [urlhttps://cp-algorithms.com/graph/2SAT.html](https://cp-algorithms.com/graph/2SAT.html). 2022 (cit. on p. 123).

- [Kön+19] M. S. Könz, G. Mazzola, A. J. Ochoa, H. G. Katzgraber, and M. Troyer. “Uncertain fate of fair sampling in quantum annealing”. *Phys. Rev. A* 100 (2019), 030303. DOI: 10.1103/PhysRevA.100.030303 (cit. on pp. 48, 63, 97).
- [Kön+21] M. S. Könz, W. Lechner, H. G. Katzgraber, and M. Troyer. “Embedding Overhead Scaling of Optimization Problems in Quantum Annealing”. *PRX Quantum* 2 (4 2021), 040322. DOI: 10.1103/PRXQuantum.2.040322 (cit. on p. 81).
- [Lan32] L. D. Landau. “Zur theorie der Energieübertragung II”. *Phys. Z. Sowjetunion* 2 (1932), 88–95 (cit. on p. 8).
- [Loh+90] E. Y. Loh, J. E. Gubernatis, R. T. Scalettar, S. R. White, D. J. Scalapino, and R. L. Sugar. “Sign problem in the numerical simulation of many-electron systems”. *Phys. Rev. B* 41 (13 1990), 9301–9307. DOI: 10.1103/PhysRevB.41.9301 (cit. on p. 63).
- [Lyk+21] E. M. Lykiardopoulou, A. Zucca, S. A. Scivier, and M. H. Amin. “Improving nonstoquastic quantum annealing with spin-reversal transformations”. *Phys. Rev. A* 104 (1 2021), 012619. DOI: 10.1103/PhysRevA.104.012619 (cit. on p. 64).
- [Mar+19] J. Marshall, D. Venturelli, I. Hen, and E. G. Rieffel. “Power of Pausing: Advancing Understanding of Thermalization in Experimental Quantum Annealers”. *Phys. Rev. Applied* 11 (4 2019), 044083. DOI: 10.1103/PhysRevApplied.11.044083 (cit. on p. 43).
- [Mav+18] V. Mavroeidis, K. Vishi, M. D. Zych, and A. Jøsang. “The Impact of Quantum Computing on Present Cryptography”. *Int. J. Adv. Comput. Sci. Appl.* 9 (2018). DOI: 10.14569/ijacsa.2018.090354 (cit. on p. 1).
- [Meh+21] V. Mehta, F. Jin, H. De Raedt, and K. Michielsen. “Quantum annealing with trigger Hamiltonians: Application to 2-satisfiability and nonstoquastic problems”. *Phys. Rev. A* 104 (3 2021), 032421. DOI: 10.1103/PhysRevA.104.032421 (cit. on p. 63).
- [Meh+22a] V. Mehta, F. Jin, H. De Raedt, and K. Michielsen. “Quantum annealing for hard 2-satisfiability problems: Distribution and scaling of minimum energy gap and success probability”. *Phys. Rev. A* 105 (6 2022), 062406. DOI: 10.1103/PhysRevA.105.062406 (cit. on p. 81).
- [Meh+22b] V. Mehta, F. Jin, K. Michielsen, and H. De Raedt. “On the hardness of quadratic unconstrained binary optimization problems”. *Front. Phys.* (2022), 765. DOI: 10.3389/fphy.2022.956882 (cit. on pp. 14, 39).
- [MF20] C. McGeoch and P. Farré. *The D-Wave Advantage System: An Overview*. Tech. rep. Tech. Rep.(D-Wave Systems Inc, Burnaby, BC, Canada, 2020) D-Wave Technical Report Series 14-1049A-A, 2020 (cit. on pp. 2, 29, 30).

- [MHF21] C. Micheletti, P. Hauke, and P. Faccioli. “Polymer Physics by Quantum Computing”. *Phys. Rev. Lett.* 127 (8 2021), 080501. DOI: 10.1103/PhysRevLett.127.080501 (cit. on p. 1).
- [Mic+17] K. Michielsen, M. Nocon, D. Willsch, F. Jin, T. Lippert, and H. De Raedt. “Benchmarking gate-based quantum computers”. *Comput. Phys. Commun.* 220 (2017), 44–55. DOI: 10.1016/j.cpc.2017.06.011 (cit. on p. 1).
- [Miz19] A. Mizel. “Proof of efficient, parallelized, universal adiabatic quantum computation”. *Phys. Rev. A* 99 (2 2019), 022311. DOI: 10.1103/PhysRevA.99.022311 (cit. on p. 7).
- [MN08] S. Morita and H. Nishimori. “Mathematical foundation of quantum annealing”. *J. Math. Phys.* 49 (2008), 125210. DOI: 10.1063/1.2995837 (cit. on pp. 119, 120).
- [MNK09] Y. Matsuda, H. Nishimori, and H. G. Katzgraber. “Ground-state statistics from annealing algorithms: quantum versus classical approaches”. *New J. Phys.* 11 (2009), 073021. DOI: 10.1088/1367-2630/11/7/073021 (cit. on pp. 48, 63, 97).
- [Moh+21] H. Mohammadbagherpoor, P. Dreher, M. Ibrahim, Y. Oh, J. Hall, R. E. Stone, and M. Stojkovic. “Exploring Airline Gate-Scheduling Optimization Using Quantum Computers”. *arXiv preprint arXiv:2111.09472* (2021). DOI: 10.48550/arXiv.2111.09472 (cit. on p. 1).
- [MST04] R. Martoňák, G. E. Santoro, and E. Tosatti. “Quantum annealing of the traveling-salesman problem”. *Phys. Rev. E* 70 (5 2004), 057701. DOI: 10.1103/PhysRevE.70.057701 (cit. on p. 81).
- [Mul+19] V. K. Mulligan, H. Melo, H. I. Merritt, S. Slocum, B. D. Weitzner, A. M. Watkins, P. D. Renfrew, C. Pelissier, P. S. Arora, and R. Bonneau. “Designing peptides on a quantum computer”. *BioRxiv* (2019), 752485. DOI: 10.1101/752485 (cit. on p. 3).
- [NC10] M. A. Nielsen and I. L. Chuang. *Quantum Computation and Quantum Information: 10th Anniversary Edition*. Cambridge University Press, 2010. DOI: 10.1017/CB09780511976667 (cit. on pp. 2, 3, 6, 131).
- [Neu14a] T. Neuhaus. “Monte Carlo Search for Very Hard K-SAT Realizations for Use in Quantum Annealing”. *arXiv:1412.5361* (2014). DOI: 10.48550/arXiv.1412.5361 (cit. on pp. 10, 11, 13, 39).
- [Neu14b] T. Neuhaus. “Quantum searches in a hard 2-SAT ensemble”. *arXiv:1412.5460* (2014). DOI: 10.48550/arXiv.1412.5460 (cit. on pp. 10, 13, 39, 81, 83).
- [Nev+09] H. Neven, V. S. Denchev, M. Drew-Brook, J. Zhang, W. G. Macready, and G. Rose. “NIPS 2009 Demonstration: Binary Classification using Hardware Implementation of Quantum Annealing”. In: 2009 (cit. on p. 3).
- [NT17] Hidetoshi Nishimori and Kabuki Takada. “Exponential Enhancement of the Efficiency of Quantum Annealing by Non-Stoquastic Hamiltonians”. *Front. ICT* 4 (2017). DOI: 10.3389/fict.2017.00002 (cit. on pp. 63, 64).

- [OA18] D. Ottaviani and A. Amendola. “Low rank non-negative matrix factorization with d-wave 2000q”. *arXiv preprint arXiv:1808.08721* (2018). DOI: 10.48550/arXiv.1808.08721 (cit. on p. 43).
- [ÖJV18] A. B. Özgüler, R. Joynt, and M. G. Vavilov. “Steering random spin systems to speed up the quantum adiabatic algorithm”. *Phys. Rev. A* 98 (2018), 062311. DOI: 10.1103/PhysRevA.98.062311 (cit. on p. 63).
- [OML19] R. Orús, S. Mugel, and E. Lizaso. “Quantum computing for finance: Overview and prospects”. *Reviews in Physics* 4 (2019), 100028. DOI: <https://doi.org/10.1016/j.revip.2019.100028> (cit. on p. 1).
- [ONL18] M. Ohkuwa, H. Nishimori, and D. A. Lidar. “Reverse annealing for the fully connected  $p$ -spin model”. *Phys. Rev. A* 98 (2 2018), 022314. DOI: 10.1103/PhysRevA.98.022314 (cit. on p. 43).
- [P07] Oskar P. “Zur Theorie der Matrizes”. *Mathematische Annalen* 64 (1907), 248–263. DOI: 10.1007/BF01449896 (cit. on p. 121).
- [PAL14] K. L. Pudenz, T. Albash, and D. A. Lidar. “Error-corrected quantum annealing with hundreds of qubits”. *Nat. Commun.* 5 (2014), 3243. DOI: 10.1038/ncomms4243 (cit. on p. 1).
- [Par98] B. N. Parlett. *The symmetric eigenvalue problem*. SIAM, 1998. DOI: 10.1137/1.9781611971163 (cit. on p. 21).
- [Pav+11] E. Pavarini, D. Vollhardt, E. Koch, and A. Lichtenstein. *The LDA+ DMFT approach to strongly correlated materials*. Tech. rep. Theoretische Nanoelektronik, 2011 (cit. on pp. 21, 25).
- [PVA11] A. Perdomo-Ortiz, S. E. Venegas-Andraca, and A. Aspuru-Guzik. “A study of heuristic guesses for adiabatic quantum computation”. *Quantum Inf. Process.* 10 (2011), 33–52. DOI: [doi.org/10.1007/s11128-010-0168-z](https://doi.org/10.1007/s11128-010-0168-z) (cit. on p. 43).
- [Røn+14] T. F. Rønnow, Z. Wang, J. Job, S. Boixo, S. V. Isakov, D. Wecker, J. M. Martinis, D. A. Lidar, and M. Troyer. “Defining and detecting quantum speedup”. *Science* 345 (2014), 420–424. DOI: 10.1126/science.1252319 (cit. on pp. 1, 81).
- [Rus02] M. B. Ruskai. “Comments on Adiabatic Quantum Algorithms” (2002). DOI: 10.48550/ARXIV.QUANT-PH/0203127 (cit. on p. 121).
- [Sak20] T. Sakuma. “Application of deep quantum neural networks to finance”. *arXiv preprint arXiv:2011.07319* (2020). DOI: 10.48550/arXiv.2011.07319 (cit. on p. 1).
- [San+02] G. E. Santoro, R. Martoňák, E. Tosatti, and R. Car. “Theory of Quantum Annealing of an Ising Spin Glass”. *Science* 295 (2002), 2427–2430. DOI: 10.1126/science.1068774 (cit. on p. 81).
- [SBS18] D. Solenov, J. Brieler, and J. F. Scherrer. “The potential of quantum computing and machine learning to advance clinical research and change the practice of medicine”. *Mo. Med.* 115 (2018), 463 (cit. on p. 1).

- [Sha81] M. Sharir. “A strong-connectivity algorithm and its applications in data flow analysis”. *Computers & Mathematics with Applications* 7 (1981), 67–72. DOI: [https://doi.org/10.1016/0898-1221\(81\)90008-0](https://doi.org/10.1016/0898-1221(81)90008-0) (cit. on p. 11).
- [Sho99] P. W. Shor. “Polynomial-time algorithms for prime factorization and discrete logarithms on a quantum computer”. *SIAM Review* 41 (1999), 303–332. DOI: [10.1137/S0097539795293172](https://doi.org/10.1137/S0097539795293172) (cit. on p. 1).
- [Sim97] D. R. Simon. “On the power of quantum computation”. *SIAM J. Comput.* 26 (1997), 1474–1483. DOI: [10.1137/S0097539796298637](https://doi.org/10.1137/S0097539796298637) (cit. on p. 1).
- [SJM17] Y. Susa, J. F. Jadebeck, and H. Nishimori. “Relation between quantum fluctuations and the performance enhancement of quantum annealing in a nonstoquastic Hamiltonian”. *Phys. Rev. A* 95 (4 2017), 042321. DOI: [10.1103/PhysRevA.95.042321](https://doi.org/10.1103/PhysRevA.95.042321) (cit. on p. 64).
- [SMK77] M. Suzuki, S. Miyashita, and A. Kuroda. “Monte Carlo simulation of quantum spin systems. I”. *Prog. Theor. Phys.* 58 (1977), 1377–1387. DOI: [10.1143/PTP.58.1377](https://doi.org/10.1143/PTP.58.1377) (cit. on p. 22).
- [SN12a] Y. Seki and H. Nishimori. “Quantum annealing with antiferromagnetic fluctuations”. *Phys. Rev. E* 85 (5 2012), 051112. DOI: [10.1103/PhysRevE.85.051112](https://doi.org/10.1103/PhysRevE.85.051112) (cit. on pp. 63, 64, 81).
- [SN12b] Beatriz Seoane and Hidetoshi Nishimori. “Many-body transverse interactions in the quantum annealing of the  $p$ -spin ferromagnet”. *J. Phys. A Math. Theor.* 45 (2012), 435301. DOI: [10.1088/1751-8113/45/43/435301](https://doi.org/10.1088/1751-8113/45/43/435301) (cit. on p. 63).
- [SN15] Yuya Seki and Hidetoshi Nishimori. “Quantum annealing with antiferromagnetic transverse interactions for the Hopfield model”. *J. Phys. A Math. Theor.* 48 (2015), 335301. DOI: [10.1088/1751-8113/48/33/335301](https://doi.org/10.1088/1751-8113/48/33/335301) (cit. on p. 63).
- [SNK12] R. D. Somma, D. Nagaj, and M. Kieferová. “Quantum Speedup by Quantum Annealing”. *Phys. Rev. Lett.* 109 (5 2012), 050501. DOI: [10.1103/PhysRevLett.109.050501](https://doi.org/10.1103/PhysRevLett.109.050501) (cit. on pp. 73, 81).
- [SO05] S. Suzuki and M. Okada. “Residual Energies after Slow Quantum Annealing”. *J. Phys. Soc. Japan* 74 (2005), 1649–1652. DOI: [10.1143/JPSJ.74.1649](https://doi.org/10.1143/JPSJ.74.1649). eprint: <https://doi.org/10.1143/JPSJ.74.1649> (cit. on pp. 119, 120).
- [SRS20] J. Schnack, J. Richter, and R. Steinigeweg. “Accuracy of the finite-temperature Lanczos method compared to simple typicality-based estimates”. *Phys. Rev. Res.* 2 (2020), 013186. DOI: [10.1103/PhysRevResearch.2.013186](https://doi.org/10.1103/PhysRevResearch.2.013186) (cit. on p. 21).
- [ST08] G. E. Santoro and E. Tosatti. “Optimization using quantum mechanics: quantum annealing through adiabatic evolution”. *J. Phys. A: Math. Gen.* 41 (2008), 209801. DOI: [10.1088/1751-8121/41/20/209801](https://doi.org/10.1088/1751-8121/41/20/209801) (cit. on p. 81).

- [Sus+18] Y. Susa, Y. Yamashiro, M. Yamamoto, and H. Nishimori. “Exponential speedup of quantum annealing by inhomogeneous driving of the transverse field”. *J. Phys. Soc. Jpn.* 87 (2018), 023002. DOI: 10.7566/JPSJ.87.023002 (cit. on p. 81).
- [Suz76] M. Suzuki. “Generalized Trotter’s formula and systematic approximants of exponential operators and inner derivations with applications to many-body problems”. *Commun. Math. Phys.* 51 (1976), 183–190. DOI: 10.1007/BF01609348 (cit. on p. 22).
- [Suz85] M. Suzuki. “Decomposition formulas of exponential operators and Lie exponentials with some applications to quantum mechanics and statistical physics”. *J. Math. Phys.* 26 (1985), 601–612. DOI: 10.1063/1.526596 (cit. on p. 22).
- [Suz91] M. Suzuki. “General theory of fractal path integrals with applications to many-body theories and statistical physics”. *Journal of Mathematical Physics* 32 (1991), 400–407. DOI: 10.1063/1.529425 (cit. on p. 22).
- [Teu03] S. Teufel. *Adiabatic perturbation theory in quantum dynamics*. Springer, 2003. DOI: 10.1007/b13355 (cit. on p. 114).
- [TK84] H. Tal-Ezer and R. Kosloff. “An accurate and efficient scheme for propagating the time dependent Schrödinger equation”. *J. Chem. Phys.* 81 (1984), 3967–3971. DOI: 10.1063/1.448136 (cit. on p. 21).
- [Tra+16] T. Tran, M. Do, E. Rieffel, J. Frank, Z. Wang, B. O’Gorman, D. Venturelli, and J. Beck. “A hybrid quantum-classical approach to solving scheduling problems”. In: *Proceedings of the International Symposium on Combinatorial Search*. Vol. 7. 2016, 98–106. DOI: 10.1609/socs.v7i1.18390 (cit. on p. 1).
- [Tro59] H. F. Trotter. “On the product of semi-groups of operators”. *Proc. Am. Math. Soc.* 10 (1959), 545–551. DOI: 10.2307/2033649 (cit. on p. 22).
- [TW05] M. Troyer and U. Wiese. “Computational Complexity and Fundamental Limitations to Fermionic Quantum Monte Carlo Simulations”. *Phys. Rev. Lett.* 94 (17 2005), 170201. DOI: 10.1103/PhysRevLett.94.170201 (cit. on p. 63).
- [TYN20] K. Takada, Y. Yamashiro, and H. Nishimori. “Mean-Field Solution of the Weak-Strong Cluster Problem for Quantum Annealing with Stoquastic and Non-Stoquastic Catalysts”. *J. Phys. Soc. Japan* 89 (2020), 044001. DOI: 10.7566/JPSJ.89.044001 (cit. on p. 63).
- [VK19] D. Venturelli and A. Kondratyev. “Reverse quantum annealing approach to portfolio optimization problems”. *Quantum Mach. Intell.* 1 (2019), 17–30. DOI: 10.1007/s42484-019-00001-w (cit. on pp. 1, 43).
- [VL17] W. Vinci and D. Lidar. “Non-stoquastic Hamiltonians in quantum annealing via geometric phases”. *Npj Quantum Inf.* 3 (2017). DOI: 10.1038/s41534-017-0037-z (cit. on p. 2).

- [Wal+05] P. Walther, K. J. Resch, T. Rudolph, E. Schenck, H. Weinfurter, V. Vedral, M. Aspelmeyer, and A. Zeilinger. “Experimental one-way quantum computing”. *Nature* 434 (2005), 169–176. DOI: 10.1038/nature03347 (cit. on p. 1).
- [WE19] S. Woerner and D. J. Egger. “Quantum risk analysis”. *npj Quantum Inf.* 5 (2019), 15. DOI: 10.1038/s41534-019-0130-6 (cit. on p. 1).
- [Wei+06] A. Weiße, G. Wellein, A. Alvermann, and H. Fehske. “The kernel polynomial method”. *Rev. Mod. Phys.* 78 (2006), 275. DOI: 10.1103/RevModPhys.78.275 (cit. on p. 21).
- [Wil+20] M. Willsch, D. Willsch, F. Jin, H. De Raedt, and K. Michielsen. “Real-time simulation of flux qubits used for quantum annealing”. *Phys. Rev. A* 101 (1 2020), 012327. DOI: 10.1103/PhysRevA.101.012327 (cit. on p. 29).
- [Wil+21] D. Willsch, M. Willsch, F. Jin, K. Michielsen, and H. De Raedt. “GPU-accelerated simulations of quantum annealing and the quantum approximate optimization algorithm”. *arXiv:2104.03293* (2021). DOI: 10.1016/j.cpc.2022.108411 (cit. on p. 81).
- [Wil65] J. H. Wilkinson. *The algebraic eigenvalue problem*. Clarendon Press, Oxford, 1965 (cit. on pp. 21, 25).
- [WKI12] L. Wang, S. K. Kowk, and W. H. Ip. “Design of an improved quantum-inspired evolutionary algorithm for a transportation problem in logistics systems”. *J. Intell. Manuf.* 23 (2012), 2227–2236. DOI: 10.1007/s10845-011-0568-7 (cit. on p. 1).
- [Yam+19] Y. Yamashiro, M. Ohkuwa, H. Nishimori, and D. A. Lidar. “Dynamics of reverse annealing for the fully connected  $p$ -spin model”. *Phys. Rev. A* 100 (5 2019), 052321. DOI: 10.1103/PhysRevA.100.052321 (cit. on p. 43).
- [Yar+22] S. Yarkoni, E. Raponi, T. Bäck, and S. Schmitt. “Quantum annealing for industry applications: Introduction and review”. *Rep. Prog. Phys.* (2022). DOI: 10.1088/1361-6633/ac8c54 (cit. on p. 3).
- [Zen32] C. Zener. “Non-adiabatic crossing of energy levels”. *Proc. R. Soc. London, Ser. A* 137 (1932), 696–702. DOI: 10.1098/rspa.1932.0165 (cit. on p. 8).
- [ZZS16] L. Zeng, J. Zhang, and M. Sarovar. “Schedule path optimization for adiabatic quantum computing and optimization”. *J. Phys. A Math. Theor.* 49 (2016), 165305. DOI: 10.1088/1751-8113/49/16/165305 (cit. on p. 63).

# List of publications

1. V. Mehta, F. Jin, H. De Raedt, and K. Michielsen. “Quantum annealing with trigger Hamiltonians: Application to 2-satisfiability and nonstoquastic problems”. *Phys. Rev. A* 104 (3 2021), 032421.
2. V. Mehta, F. Jin, H. De Raedt, and K. Michielsen. “Quantum annealing for hard 2-satisfiability problems: Distribution and scaling of minimum energy gap and success probability”. *Phys. Rev. A* 105 (6 2022), 062406.
3. V. Mehta, F. Jin, K. Michielsen, and H. De Raedt. “On the hardness of quadratic unconstrained binary optimization problems”. *Front. Phys.* (2022), 765.
4. H. De Raedt, M. I. Katsnelson, M. S. Jattana, V. Mehta, M. Willsch, D. Willsch, K. Michielsen, and F. Jin. “Einstein-Podolsky–Rosen–Bohm experiments: A discrete data driven approach”. *Annals of Physics* 453 (2023), 169314.



# Eidesstattliche Erklärung

Ich, Vrinda Mehta, erkläre hiermit, dass diese Dissertation und die darin dargelegten Inhalte die eigenen sind und selbstständig, als Ergebnis der eigenen originären Forschung, generiert wurden.

Hiermit erkläre ich an Eides statt

1. Diese Arbeit wurde vollständig oder größtenteils in der Phase als Doktorand dieser Fakultät und Universität angefertigt;
2. Sofern irgendein Bestandteil dieser Dissertation zuvor für einen akademischen Abschluss oder eine andere Qualifikation an dieser oder einer anderen Institution verwendet wurde, wurde dies klar angezeigt;
3. Wenn immer andere eigene- oder Veröffentlichungen Dritter herangezogen wurden, wurden diese klar benannt;
4. Wenn aus anderen eigenen- oder Veröffentlichungen Dritter zitiert wurde, wurde stets die Quelle hierfür angegeben. Diese Dissertation ist vollständig meine eigene Arbeit, mit der Ausnahme solcher Zitate;
5. Alle wesentlichen Quellen von Unterstützung wurden benannt;
6. Wenn immer ein Teil dieser Dissertation auf der Zusammenarbeit mit anderen basiert, wurde von mir klar gekennzeichnet, was von anderen und was von mir selbst erarbeitet wurde;
7. Teile dieser Arbeit wurden zuvor veröffentlicht und zwar in:
  - V. Mehta, F. Jin, H. De Raedt, and K. Michielsen. “Quantum annealing with trigger Hamiltonians: Application to 2-satisfiability and nonstoquastic problems”. *Phys. Rev. A* 104 (3 2021), 032421.
  - V. Mehta, F. Jin, H. De Raedt, and K. Michielsen. “Quantum annealing for hard 2-satisfiability problems: Distribution and scaling of minimum energy gap and success probability”. *Phys. Rev. A* 105 (6 2022), 062406.
  - V. Mehta, F. Jin, K. Michielsen, and H. De Raedt. “On the hardness of quadratic unconstrained binary optimization problems”. *Front. Phys.* (2022), 765.

Datum:

Unterschrift:



# Acknowledgements

This work would not have been possible without the help and support of many people and organizations. I would like to take this opportunity to thank all of them.

This list cannot go any further before thanking my supervisor, Kristel Michielsen, for giving me the opportunity of working in the group, and for her constant support and understanding. In spite of being so busy, she has always organized things in ways that have never made me feel lost during this course. I feel grateful to her for always taking out the time to proof-read my papers and this thesis, and for finding out mistakes that would otherwise have gone unnoticed.

I would also like to express my deep gratitude towards Hans De Raedt, whose constant encouragement, not just limited to the scope of this project, but life in general, has made me a lot more comfortable with the challenges of this field, as well as some bigger challenges in life. I am very thankful to him for all his time for the deep and meaningful discussions. Not to forget the funny and interesting stories which have always served as refreshing breaks from the monotony of the writing tasks.

The next in the line has to be the go-to person for this (and also my master) thesis. I offer my sincere thanks to Fengping Jin whose constant support and guidance have helped me keep things on track. I am immensely grateful to him for his patience and for creating an environment where I feel comfortable asking questions, even the silly ones. Despite of things sometimes going wrong, his trust and words of encouragement have always kept me going. His approachable nature and genuine interest in almost everything have contributed very much in my learning process, and I will always be grateful to him for that.

I am also thankful to all the members of our QIP group for giving me such a friendly, comfortable, and fun working environment. My thanks to Dennis Willsch for being ever so kind and helpful, starting from setting up the required libraries for linear algebra to helping me with the submission related formalities. I would also like to thank Madita Willsch for helping me with the submission and the defense related queries and for co-tutoring the computational physics course with me. Her attention to details has always been inspiring for me. I have always considered myself fortunate for the fact that I was spared the intricacies of the bureaucratic and administrative things, thanks to Hannes Lagemann and Manpreet Singh Jattana for always being a few steps ahead of me on the timeline, and leaving behind a clear trail for me. I would like to thank Carlos Gonzalez, Andrea Basilio Rava, Dmitrii Nabok, Alejandro Montañez Barrera, Rijul Sachdeva, Kunal Vyas, Pim van den Heuvel, Sebastian Schulz, Edoardo Pasetto, Jaka Vodeb and Orkun Sensebat for all the nice conversations that made lunch and the bus rides to and from the Forschungszentrum enjoyable.

None of this would have been possible without the motivation, support, and love from



my family. I am really indebted to all my grandparents for their love and blessings and to my parents for being my pillars of strength and for always believing in me. The main credit for me undertaking this journey, should go to my Papuji, who has played an instrumental role in instilling in me a sense of appreciation for science, and curiosity for continuing to keep asking questions and learning. My heartfelt thanks to my sisters Pratima, Sumedha, and Saumya for their never-ending support and entertainment. The video calls with them, especially during COVID, have always made me feel at home despite of being away from home.

Next, I would like to use this opportunity to thank all my friends who have played a significant role in ensuring that I get to this point without giving up. I would like to thank Anoop Koushik for helping me in this journey in all possible ways. Starting from the basics of Linux to advanced programming techniques, I have learned a lot from him, and cannot thank him enough for always getting my back and for pushing me beyond my comfort zone. However, doing any of this while maintaining my sanity would not have been possible, if not for Shefali. Thanks to her for always being on my side in life, and for knowing the exactly right thing to say at each difficult point in my life. I would also like to extend my thanks to Sarojini Mahajan, Abhiroop Sen, Shivani Ramachandran, and Shrey Nagpal for being a part of this journey, and for the irreplaceable roles that they have played in my life.

Last but not the least, I gratefully acknowledge the Gauss Centre for Supercomputing e.V. for funding this project by providing computing time through the John von Neumann Institute for Computing (NIC) on the GCS Supercomputer JUWELS at Jülich Supercomputing Centre (JSC) and also the computing time granted through JARA on the supercomputer JURECA at Forschungszentrum Jülich. I am also thankful for the support from the project JUNIQ that has received funding from the German Federal Ministry of Education and Research (BMBF) and the Ministry of Culture and Science of the State of North Rhine-Westphalia.

Band / Volume 45

**Supercomputer simulations of transmon quantum computers**

D. Willsch (2020), IX, 237 pp

ISBN: 978-3-95806-505-5

Band / Volume 46

**The Influence of Individual Characteristics on Crowd Dynamics**

P. Georg (2021), xiv, 212 pp

ISBN: 978-3-95806-561-1

Band / Volume 47

**Structural plasticity as a connectivity generation  
and optimization algorithm in neural networks**

S. Diaz Pier (2021), 167 pp

ISBN: 978-3-95806-577-2

Band / Volume 48

**Porting applications to a Modular Supercomputer**

Experiences from the DEEP-EST project

A. Kreuzer, E. Suarez, N. Eicker, Th. Lippert (Eds.) (2021), 209 pp

ISBN: 978-3-95806-590-1

Band / Volume 49

**Operational Navigation of Agents and Self-organization Phenomena  
in Velocity-based Models for Pedestrian Dynamics**

Q. Xu (2022), xii, 112 pp

ISBN: 978-3-95806-620-5

Band / Volume 50

**Utilizing Inertial Sensors as an Extension of a Camera Tracking  
System for Gathering Movement Data in Dense Crowds**

J. Schumann (2022), xii, 155 pp

ISBN: 978-3-95806-624-3

Band / Volume 51

**Final report of the DeepRain project  
Abschlußbericht des DeepRain Projektes**

(2022), ca. 70 pp

ISBN: 978-3-95806-675-5

Band / Volume 52

**JSC Guest Student Programme Proceedings 2021**

I. Kabadshow (Ed.) (2023), ii, 82 pp

ISBN: 978-3-95806-684-7

Band / Volume 53

**Applications of variational methods for quantum computers**

M. S. Jattana (2023), vii, 160 pp

ISBN: 978-3-95806-700-4

Band / Volume 54

**Crowd Management at Train Stations in Case of Large-Scale Emergency Events**

A. L. Braun (2023), vii, 120 pp

ISBN: 978-3-95806-706-6

Band / Volume 55

**Gradient-Free Optimization of Artificial and Biological Networks using Learning to Learn**

A. Yeğenoğlu (2023), II, 136 pp

ISBN: 978-3-95806-719-6

Band / Volume 56

**Real-time simulations of transmon systems with time-dependent Hamiltonian models**

H. A. Lagemann (2023), iii, 166, XXX pp

ISBN: 978-3-95806-720-2

Band / Volume 57

**Plasma Breakdown and Runaway Modelling in ITER-scale Tokamaks**

J. Chew (2023), xv, 172 pp

ISBN: 978-3-95806-730-1

Band / Volume 58

**Space Usage and Waiting Pedestrians at Train Station Platforms**

M. Küpper (2023), ix, 95 pp

ISBN: 978-3-95806-733-2

Band / Volume 59

**Quantum annealing and its variants: Application to quadratic unconstrained binary optimization**

V. Mehta (2024), iii, 152 pp

ISBN: 978-3-95806-755-4



IAS Series  
Band / Volume 59  
ISBN 978-3-95806-755-4